Lawrence Berkeley National Laboratory
Recent Work

Title

CeLAND: search for a 4th light neutrino state with a 3 PBq 144Ce-144Pr electron antineutrino generator in KamLAND

Permalink

https://escholarship.org/uc/item/76w3g6v7

Authors

Gando, A
Gando, Y
Hayashida, S
et al.

Publication Date

2013-12-03

Peer reviewed

CeLAND: search for a 4th light neutrino state with a 3 PBq ^{144}Ce-^{144}Pr $\bar{\nu}_e$-generator in KamLAND

April 15, 2014

Abstract

The reactor neutrino and gallium anomalies can be tested with a 3-4 PBq (75-100 kilocurie scale) ^{144}Ce $-^{144}$ Pr antineutrino beta-source deployed at the center or next to a large low-background liquid scintillator detector. The antineutrino generator will be produced by the Russian reprocessing plant PA Mayak as early as 2014, transported to Japan, and deployed in the Kamioka Liquid Scintillator Anti-Neutrino Detector (KamLAND) as early as 2015. KamLAND's 13 m diameter target volume provides a suitable environment to measure the energy and position dependence of the detected neutrino flux. A characteristic oscillation pattern would be visible for a baseline of about 10 m or less, providing a very clean signal of neutrino disappearance into a yet-unknown, "sterile" state. This will provide a comprehensive test of the electron dissaperance neutrino anomalies and could lead to the discovery of a 4th neutrino state for $\Delta m_{new}^2 \gtrsim 0.1~eV^2$ and $\sin^2(2\theta_{new}) \gtrsim 0.05$.

A. Gando, Y. Gando, S. Hayashida, H. Ikeda, K. Inoue, K. Ishidoshiro, H. Ishikawa, M. Koga, R. Matsuda, S. Matsuda, T. Mitsui,D. Motoki, K. Nakamura, Y. Oki, M. Otani, I. Shimizu, J. Shirai, F. Suekane, A. Suzuki, Y. Takemoto, K. Tamae, K. Ueshima, H. Watanabe, B.D. Xu, S. Yamada,Y. Yamauchi, H. Yoshida

Research Center for Neutrino Science, Tohoku University, Sendai 980-8578, Japan

M. Cribier[1,2], M. Durero[2], V. Fischer[2], J. Gaffiot[1], N. Jonqueres[3], A. Kouchner[1], T. Lasserre[1,2,4,5], D. Leterme[3], A. Letourneau[2], D. Lhuillier[2], G. Mention[2], G. Rampal[3], L. Scola[2], Ch. Veyssière[2], M. Vivier[2], and P. Yala[3]

[1]*Astroparticules et Cosmologie APC, 10 rue Alice Domon et Léonie Duquet, 75205 Paris cedex 13, France*
[2]*Commissariat à l'énergie atomique et aux énergies alternatives, Centre de Saclay, IRFU, 91191 Gif-sur-Yvette, France*
[2]*Commissariat à l'énergie atomique et aux énergies alternatives, Centre de Saclay, DEN/DANS & DEN/DM2S, 91191 Gif-sur-Yvette, France*

[4] *European Research Council Starting Grant 4th-Nu-Avenue StG-307184*
[5]*Corresponding author (thierry.lasserre@cea.fr)*

B. E. Berger

Colorado State University, Fort Collins, CO 80523-1875, USA

A. Kozlov

Kavli Institute for the Physics and Mathematics of the Universe (WPI), University of Tokyo, Kashiwa 277-8583, Japan

T. Banks[2], D. Dwyer[1], B. K. Fujikawa[1], K. Han[2], Yu. G. Kolomensky[1,2], Y. Mei[2], T. O'Donnell[2]

[1]*Lawrence Berkeley National Laboratory, Berkeley, CA 94720, USA*
[2]*University of California, Berkeley, CA 94704, USA*

Patrick Decowski

Nikhef and the University of Amsterdam, Science Park 105 1098 XG, Amsterdam, the Netherlands

D. M. Markoff

North Carolina Central University, Durham, NC 27707, USA

S. Yoshida

Graduate School of Science, Osaka University, Toyonaka, Osaka 560-0043, Japan

V.N. Kornoukhov[1], T. V.M. Gelis[3], G.V. Tikhomirov[2], I.S. Saldikov[2]

[1] *Russian Federation State Scientific Center of Theoretical and Experimental Physics Institute, 117218 Moscow, Russia*
[2]*Scientific and Research Nuclear University, Moscow engineering and Physics Institute, Russia*
[3] *Russian Academy of Sciences A.N. Frumkin Institute of Physical chemistry and Electrochemistry, Russia*

J. G. Learned, J. Maricic, S. Matsuno, R. Milincic

University of Hawaii at Manoa, Honolulu, HI 96822, USA

H. J. Karwowski

University of North Carolina, Chapel Hill, NC 27599, USA

Y. Efremenko

University of Tennessee, Knoxville, TN 37996, USA

J. A. Detwiler, S. Enomoto

University of Washington, Seattle, WA 98195, USA

Contents

1 Executive summary

Over the last 20 years a standard neutrino oscillation framework associated with small splittings between the ν mass states has become well established. The three ν flavors (ν_e, ν_μ, ν_τ) are mixtures of three massive neutrinos (ν_1, ν_2, ν_3) separated by squared mass differences of $\Delta m_{21}^2 = \Delta m_{sol}^2 = 7.50_{-0.20}^{+0.19} \times 10^{-5}\,\text{eV}^2$ and $|\Delta m_{31}^2| \approx |\Delta m_{32}^2| = \Delta m_{atm}^2 = 2.32_{-0.08}^{+0.12} \times 10^{-3}\,\text{eV}^2$ [3]. This is a minimal extension of the Standard Model that requires a lepton mixing matrix, similarly to the quark sector.

Beyond this model, indications of oscillations between active and sterile ν_s have been observed in LSND [4], MiniBooNE [5, 6], Gallium [7, 8, 9] and more recently by reactor experiments [10]. This suggests the possible existence of a fourth massive ν with a mass of $\Delta m^2 \gtrsim 0.1\,\text{eV}^2$ [11, 12, 13]. Both the reactor and Gallium anomalies result from the observation of the disappearance of MeV energy ν_e and $\bar{\nu}_e$ in counting experiments. Therefore, to definitively test the anomalies one must not only test neutrino disappearance at short baselines, but also search for an oscillation pattern as a function of L/E_ν energy and baseline-dependent signatures. Probing Δm^2 values on the order of 0.1 to a few eV^2 implies that an oscillation search using neutrinos with energies of typical of radioactive decays, i.e. in the few MeV range, requires a baseline of only several meters. Assuming CP invariance, both gallium and reactor anomalies can be unambiguously tested using a neutrino emitter placed inside or next to a large 10-meter scale liquid scintillator detector, such as Borexino, KamLAND, SNO+, or Daya Bay. This constitutes an elegant method to probe the existence of oscillations into a 4th neutrino by using a well-known neutrino detector.

There are two options for deploying intense ν emitters in large liquid scintillator detectors: monochromatic ν_e emitters, like ^{51}Cr or ^{37}Ar, or $\bar{\nu}_e$ emitters with continuous β-spectra, like ^{144}Ce, ^{90}Sr, ^{42}Ar or ^{106}Ru. In the case of ν_e emitters the signature is provided by ν_e elastic scattering off electrons in the liquid scintillator molecules. This signature can be mimicked by Compton scattering induced by radioactivity or cosmogenic background, or by Solar-ν's. The constraints of an experiment with ν_e impose the use of a very high activity source $\gtrsim 10$ MCi outside of the detector target. In the case of $\bar{\nu}_e$, events are detected via the inverse beta decay reaction (IBD), which provides a e^+-n delayed coincidence that offers an efficient rejection of the mentioned background. For this reason, we focus our studies on $\bar{\nu}_e$ sources in the current proposal.

Based on the concept presented in 2011 in [1], the CeLAND collaboration intends to use an intense ^{144}Ce source decaying into the unstable daughter ^{144}Pr which, in turn, decays into stable ^{144}Nd with a Q-value of 2.996 MeV. The ^{144}Pr decay produces antineutrinos above the 1.8 MeV threshold for the inverse beta decay reaction. The half-life of ^{144}Ce is 285 days, and that of its daughter ^{144}Pr is only 17.3 minutes, so that the latter decay remains in equilibrium at all times. This thus leaves a significant amount of time for the source production, its transportation to the detector, and the data taking, without significant decrease in its initial activity.

The intense ^{144}Ce $-^{144}$Pr antineutrino generator (ANG hereafter) can be produced at the Federal State Unitary Enterprise Mayak Production Association (FSUE -Mayak- PA or simply Mayak) reprocessing plant in Russia as early as 2014. The source will then be transported within one month to the Kamioka mine, Japan, where the KamLAND detector is located. The CeLAND collaboration intends to deploy a 75-100 kCi (2.78-3.73 PBq) antineutrino generator within 13m of the KamLAND detector center, as early as 2015. The plan is to take data for at least 18 months and to search for a fourth neutrino. If a hint of oscillation is observed, the collaboration would consider deploying the source at the center of the detector, or procuring a second antineutrino generator to increase the statistical power of the experiment. Such deployment strategy allows a comprehensive test of the electron disappearance neutrino anomalies and could lead to the discovery of a 4th neutrino state for $\Delta m_{new}^2 \gtrsim 0.1\ eV^2$ and $\sin^2(2\theta_{new}) \gtrsim 0.05$.

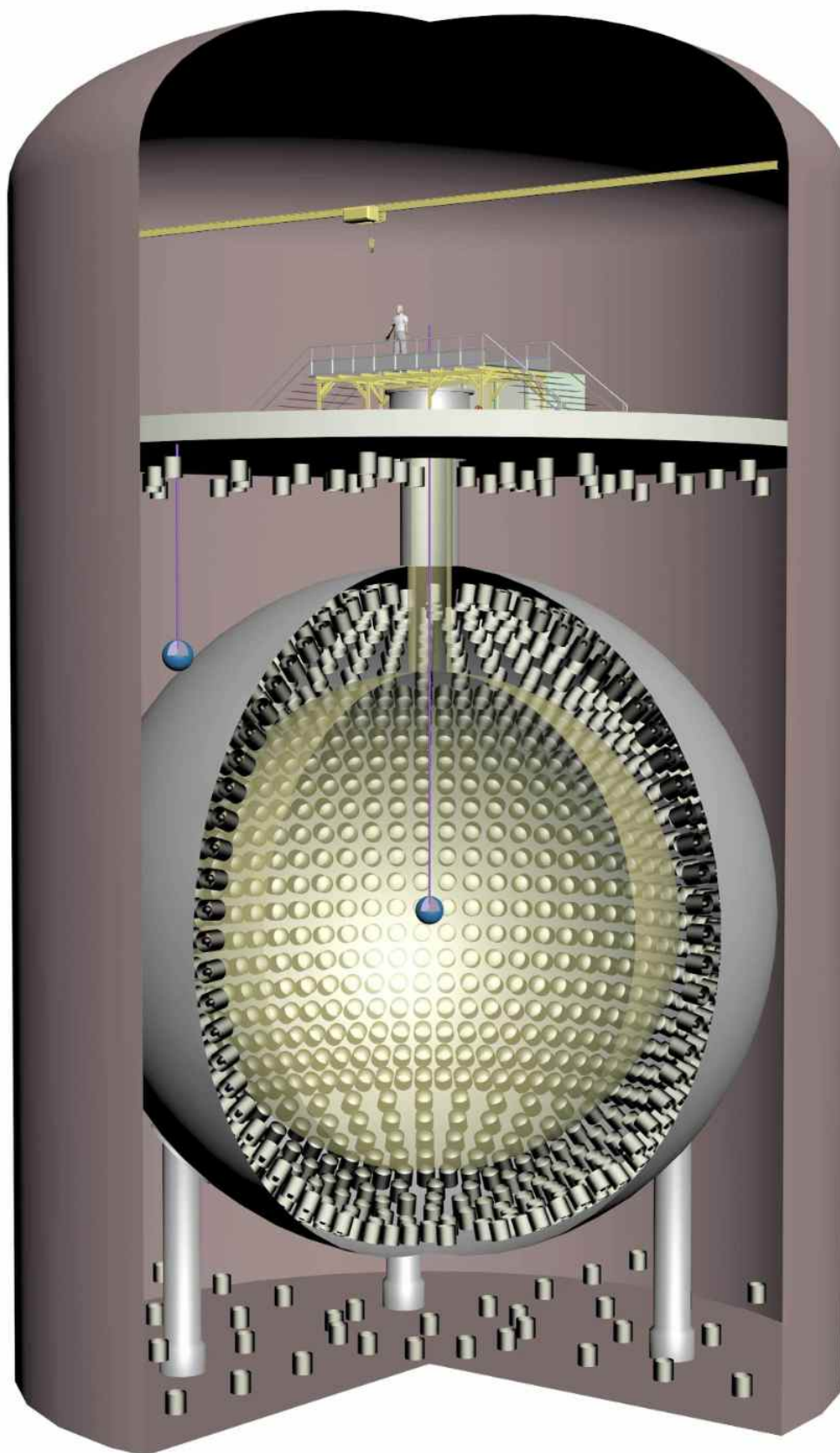Figure 1: Schematic view of the CeLAND experiment. In the first phase of the experiment the collaboration intends to deploy a 75-100 kCi source in the water Cherenkov outer detector of KamLAND. This run could be followed by the deployment of the same source (approx. 50 kCi after 6 months) at the center of the KamLAND detector for 1 year (in liquid scintillator target) in case of detection hint of a fourth neutrino state.

2 Physics motivations

2.1 Oscillation overview

Neutrino oscillations have been observed in solar, atmospheric, and long-baseline reactor and accelerator experiments. For a detailed review, see for example [2]. The data collected so far by these experiments are well fitted in the framework of a three-neutrino mixing approach, in which the three known flavor neutrinos ν_e, ν_μ and ν_τ are unitary linear combinations of three massive neutrinos ν_1, ν_2 and ν_3 with squared-mass differences and mixing angles [3]:

$$\Delta m_{21}^2 = \Delta m_{sol}^2 = 7.50^{+0.19}_{-0.20} \times 10^{-5} eV^2, \tag{1}$$

$$sin^2(2\theta_{12}) = 0.857^{+0.023}_{-0.025} \tag{2}$$

$$\mid \Delta m_{31}^2 \mid \approx \mid \Delta m_{32}^2 \mid = \Delta m_{atm}^2 = 2.32^{+0.12}_{-0.08} \times 10^{-3} eV^2, \tag{3}$$

$$sin^2(2\theta_{23}) > 0.95\,(90\%\,C.L.),\ sin^2(2\theta_{13}) = 0.098 \pm 0.013 \tag{4}$$

where $\Delta m_{jk}^2 = m_j^2 - m_k^2$ and m_j is the mass of the neutrino ν_j.

Besides this well-established picture, there are a few anomalies which could point toward short-baseline (SBL) neutrino oscillations generated by a larger squared-mass difference: the gallium radioactive source experiment anomalies [7, 8, 9], the recently observed reactor antineutrino anomaly [10], and the MiniBooNE [5, 6] and LSND [4] accelerator neutrino anomalies. Existence of a fourth yet unobserved neutrino species is not ruled out by cosmological data obtained by PLANCK [14] and WMAP [15]. In this section, we successively review these anomalies and give an up-to-date interpretation in terms of light sterile neutrinos.

2.2 The Gallium anomaly

Man-made neutrino sources were originally proposed and designed to test solar-ν detection in the GALLEX [16, 17, 18] and SAGE [19, 20, 21] experiments. Intense Mega Curie (MCi) ^{51}Cr and ^{37}Ar ν_e sources with precisely measured activities were placed at the center of the detectors to count for the number of ν_e events, as a tool to understand the detector responses. Taking into account the uncertainty of the cross-section of the detection process $\nu_e +^{71}$Ga $\to^{71}$Ge $+$ e$^-$, the ratios R of measured to predicted ^{71}Ge event rates reported by the experiments

$$R_{Cr1}^{GALLEX} = 0.95^{+0.11}_{-0.12},\ R_{Cr2}^{GALLEX} = 0.81^{+0.10}_{-0.11}, \tag{5}$$

$$R_{Cr}^{SAGE} = 0.95^{+0.12}_{-0.12},\ R_{Ar}^{SAGE} = 0.79^{+0.09}_{-0.10} \tag{6}$$

with an averaged ratio of

$$R^{Ga} = 0.86^{+0.05}_{-0.05}. \tag{7}$$

The number of measured events is smaller than the prediction at the 2.7σ level, leading to the so-called Gallium anomaly. Although the cross-section of the $\nu_e +^{71}$Ga $\to^{71}$Ge $+$ e$^-$ detection process might have been overestimated by adding the uncertain transitions from the ground state of ^{71}Ga to two excited states of ^{71}Ge, the anomaly still remains at the 1.8σ level in the absence of such transitions, with a ratio $R^{Ga} = 0.90^{+0.05}_{-0.05}$. Recently, a re-interpretation of the Gallium data with new measurements of the Gamow-Teller strengths of the transitions from the ground state of ^{71}Ga to the two excited states of ^{71}Ge confirmed the anomaly at the 3σ level [9].

2.3 The reactor antineutrino anomaly

Nuclear reactors emit $\bar{\nu}_e$ through β^- decay of fission products. Any reactor antineutrino spectrum is mostly the sum of the neutrino spectra of the four fissioning nuclei (^{235}U, ^{238}U, ^{239}Pu and ^{241}Pu) weighted by their relative fission rate. Since thousands of different β branches are available to the unstable fission products, and many of them are still unknown, neutrino spectra predictions cannot fully rely on simulations. Neutrino spectra are then estimated by converting the precise measurement of the total electron spectrum emitted by nuclear fuel under neutron irradiation, using energy conservation law. However, some modeling, such as of the end point distribution of the beta branches, still remain necessary.

In 2011, a revised calculation of the rate of $\bar{\nu}_e$ production by nuclear reactors yielded yet another indication of the hypothetical existence of a fourth neutrino species. The new calculation relies on

detailed knowledge of the decays of thousands of fission products listed by nuclear databases [22], while the previous calculation used a phenomenological model based on 30 effective β-branches. The revised rate of $\bar{\nu}_e$ production by nuclear reactors is 3.5% higher than previously thought and was confirmed independently by another calculation [23]. This new calculation motivated a re-analysis of 19 past reactor experiments at reactor distances < 100 m. Figure 2 shows the ratio of measured-to-expected $\bar{\nu}_e$ count rates in each of these experiments, following the revised calculation of the rate of $\bar{\nu}_e$ production by nuclear reactors combined with a new estimation of the inverse β decay cross-section (driven by the neutron life-time measurement) and off-equilibrium corrections to the reactor fuel composition. Along with these new ratios are also displayed the results of middle-baseline experiments (L > 100 m) such as Chooz [24] or Palo Verde [25]. The dotted line represents a "classic" three active neutrinos mixing scheme. The solid line shows a (3+1) sterile neutrino model. A constant fit to the 19 SBL experiments' measured-over-expected $\bar{\nu}_e$ count rates gives a mean ratio of $R^R = 0.927 \pm 0.023$, corresponding to a 3σ discrepancy called the reactor antineutrino anomaly (RAA)[10]. The SBL reactor data suggests a new $\Delta m^2_{new} \sim 1\,eV^2$ if interpreted in terms of a new SBL oscillation driven by a 4th neutrino state.
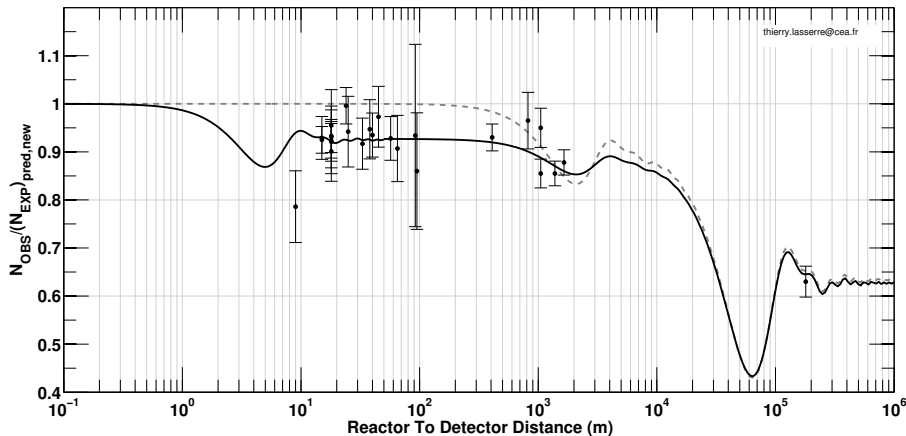
Figure 2: Re-analysis of the past reactor antineutrino experiments, which indicates an anomaly in the expected measured-to-predicted count rates of $\bar{\nu}_e$ at short distances. The dashed line corresponds to the classic three-neutrino picture with the squared mass differences quoted above. The solid line corresponds to a 3 active neutrinos plus one sterile neutrino (3+1) model.

2.4 Accelerator experiment anomalies

2.4.1 The LSND anomaly

The LSND experiment was designed to search for $\bar{\nu}_\mu \to \bar{\nu}_e$ oscillations at short distances and ran at the Los Alamos 800 MeV proton accelerator, producing $\bar{\nu}_\mu$ up to 300 MeV by μ^+ decay at rest [26]. The LSND detector was placed 30 m away from the $\bar{\nu}_\mu$ source and the detection process of $\bar{\nu}_e$ relied on the inverse β decay reaction $\bar{\nu}_e + p^+ \to e^+ + n$. Using the data collected between 1993 and 1998, the collaboration reported evidence for $\bar{\nu}_\mu$ oscillations at the 3.8σ level, with a total excess of $87.9 \pm 22.4 \pm 6.0$ events consistent with the $\bar{\nu}_e + p^+ \to e^+ + n$ reaction above the expected background [4]. In conjunction with other known neutrino limits, the LSND data suggest that the observed neutrino oscillations occur in the 0.2-10 eV^2 Δm^2 range, leading to the LSND anomaly.

2.4.2 The MiniBooNE anomaly

MiniBooNE is an appearance experiment which ran at Fermilab between 2002 and 2012. It has been searching for a $\nu_\mu \to \nu_e$ and $\bar{\nu}_\mu \to \bar{\nu}_e$ oscillation signal in the LSND L/E$_\nu$ range [27]. The experiment uses the Fermilab Booster neutrino beam, which produces ν_μ ($\bar{\nu}_\mu$) with energies up to 3 GeV with a 8 GeV proton beam hitting a Beryllium target. The center of the detector is 541 m away

from the neutrino source, and the ν_e ($\bar{\nu}_e$) detection process relies on quasi-elastic charged-current scattering on nucleons $\nu_e + C \to e^- + X$ and $\bar{\nu}_e + C \to e^+ + X$ (CCQE). In 2007, the MiniBooNE collaboration released its first results and showed no evidence of $\nu_\mu \to \nu_e$ oscillations for neutrino energies above 475 MeV [28].

However in their second publication [5], the collaboration reported a sizable excess of $83.7 \pm 15.1 \pm 19.3$ electron-like events for neutrino energies between 300 MeV and 475 MeV, corresponding to a significance of 3.4σ. In the antineutrino mode, MiniBooNE observes an excess of 24.7 ± 18.0 events in the $475 < E_\nu < 3000$ MeV energy range, which is consistent with the antineutrino oscillations suggested by the LSND data [6]. Finally, a combined analysis of the data collected in the neutrino and antineutrino mode recently showed an excess of $240.3 \pm 34.5 \pm 52.6$ events, updating the significance to 3.8σ [29]. The combined dataset favors Δm^2 in the 0.01-1 eV^2 range.

2.5 Inputs from cosmology

Cosmological data can also be used to test the sterile neutrino hypothesis because the Universe expansion rate is sensitive to the energy density in relativistic particles during the radiation domination era [15]:

$$H^2(t) \approx \frac{8\pi G}{3}(\rho_\gamma + \rho_\nu),$$ (8)

where ρ_γ and ρ_ν are the photon and neutrino energy density, respectively and

$$\rho_\nu = N_{eff}\frac{7\pi^2}{120}T_\nu^4.$$ (9)

N_{eff} could be interpreted as the effective number of neutrino species. It is equal to 3.046 in the standard model of cosmology with three generations of fermions. The extra energy density of neutrinos with respect to $N_{eff} = 3$ comes from QED and non-instantaneous decoupling effects in the calculation of the neutrino temperature T_ν. From a particle physics perspective, a sterile neutrino that mixes with active neutrinos can increase the relativistic energy density in the early Universe through oscillation-based thermal production, leading to a $N_{eff} > 3.046$. With ρ_γ being extremely well determined from measurements of the cosmic microwave background (CMB) temperature, constraints on $H(t)$ in the early Universe can be then interpreted as bounds on ρ_ν and hence on N_{eff}.

Various cosmological observables can be used to search for signatures of sterile neutrinos. Those include the light elemental abundances from big bang nucleosynthesis (BBN), the CMB anisotropies and the large-scale structure distribution. figure 3 summarizes the best constraints on N_{eff} obtained with the combination of these different cosmological observables. The recent Planck result leads to $N_{eff} = 3.36 \pm 0.66$ at 95% C.L. if no additional constraint are being used[14]. However including the astrophysical constraints on the Hubble constant measurement this results shifts to $N_{eff} = 3.52 \pm 0.46$ at 95% C.L. Therefore $N_{eff} > 3.046$ is mildly disfavored but this cosmological bound is still model dependent. Further laboratory experiments are thus mandatory to test the hypothetical existence of a fourth neutrino state.
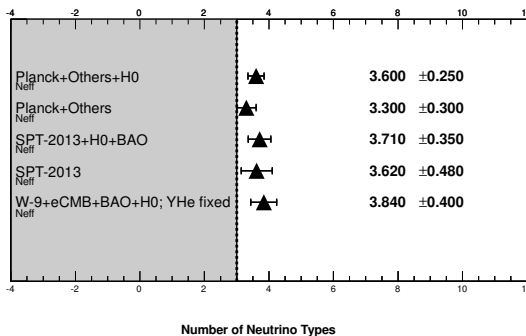
Figure 3: Constraints obtained on the number of effective neutrino species N_{eff} from different cosmological observables, based on WMAP 9-year data, PLANCK, SPT, BAO, and Hubble constant astrophysical inputs. BAO corresponds to the baryon acoustic oscillations data. ACT and SPT are the Atacama Cosmology Telescope and South Pole Telescope, respectively, which measure the CMB damping tail. Reference [15] gives further details about these experiments.

2.6 Global picture of SBL oscillations

Table1 summarizes the different anomalies observed so far in past neutrino oscillation experiments. Many studies have been performed to interpret the results of the different dataset in terms of oscillations into a fourth neutrino state. Figure 4 shows a comparison of the allowed 95% C.L. regions in the $\sin^2(2\theta_{\text{new}}) - \Delta m^2_{\text{new}}$ parameter space obtained from the separate fits of the different anomalies presented previously in the framework of a (3+1) neutrino mixing model. A global fit to the Gallium, reactor, solar, and ν_eC scattering data shows that two regions are preferred (in red contours), centered around $\Delta m^2_{\text{new}} = 7.6\,\text{eV}^2$, $\sin^2(2\theta_{\text{new}}) = 0.12$ and $\Delta m^2_{\text{new}} \simeq 2\,\text{eV}^2$, $\sin^2(2\theta_{\text{new}}) \simeq 0.1$ [9]. The second region is preferred by Gallium and reactor data.
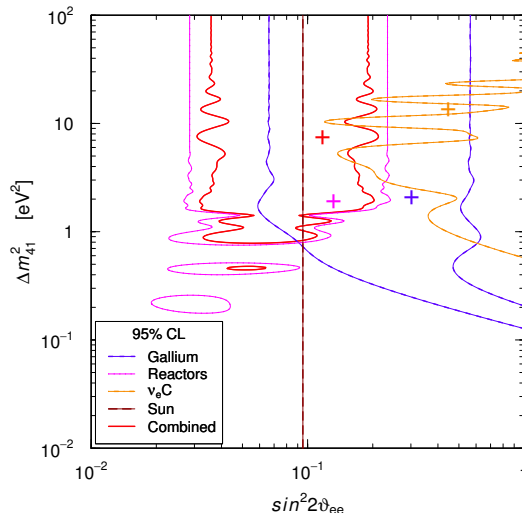
Figure 4: Allowed 95% C.L. regions in the $\sin^2(2\theta_{\text{new}}) - \Delta m^2_{\text{new}}$ plane obtained from separate fits of Gallium, reactor, solar and $\nu_e C$ scattering data and from the combined fits of all data. Crosses indicate the best-fit points. Figure taken from [9].

Experiment	ν source	Channel	Detection	Oscillation signature	Significance
LSND	μ decay at rest	$\bar{\nu}_\mu \to \bar{\nu}_e$	IBD	Rate, energy spectrum	3.8σ
MiniBooNE	π decay in flight	$\nu_\mu \to \nu_e,\ \bar{\nu}_\mu \to \bar{\nu}_e$	CCQE	Rate, energy spectrum	3.8σ
Gallium	$^{51}Cr, ^{37}Ar$	ν_e disappearance	CCQE	Rate	$\approx 3.0\sigma$
Reactor	$^{235,238}U,\ ^{239,241}Pu$	$\bar{\nu}_e$ disappearance	IBD	Rate, energy spectrum	3.0σ
Cosmology	CMB, BBN, LSS, ...	All	-	N_{eff}	$\approx 2.0\sigma$

Table 1: Summary of the different anomalies that possibly indicate the existence of a fourth neutrino state, along with their corresponding significances.

The results of the global fits, as well as the results of Gallium and reactor data give lower limits on Δm^2_{new} but do not give any upper limits. Upper limits on Δm^2_{new}, and even upper limits on the absolute mass scale of a new sterile neutrino m_s can be derived from the effects of heavy neutrino masses on electron spectrum measured in tritium β-decay experiments such as Mainz [30, 31, 32]or KATRIN [33], the results of neutrinoless double-β decay experiments such as KamLAND-Zen [34, 36] or EXO [37]and cosmology. The current upper limits at the 95% C.L. on Δm^2_{new} lie at $\mathcal{O}(10^4\,eV^2)$ assuming a normal hierarchy and come from the Mainz experiment[32]. For Majorana neutrinos, the recent combined results of EXO and KamLAND-Zen on the effective Majorana mass in neutrinoless double-β decay gives a more stringent constraint between 10^2 and 10^3 eV^2

[9]. Finally, cosmological data have also been used to set a 95% C.L. upper limit on the mass of a new sterile neutrino [38], which exhibits some tension with the mixing parameters preferred by the terrestrial experiment data:

$$m_s < 0.45 \, eV. \tag{10}$$

Nevertheless, the reported anomalies from the various terrestrial experiments still make a compelling case for a decisive search for a fourth neutrino state in the larger mass difference region.

3 Concept of neutrino generator experiments

There are two types of ν-source suitable to search for light sterile neutrinos: monochromatic ν_e emitters, such as ^{51}Cr or ^{37}Ar and $\bar{\nu}_e$ emitters with a continuous β-spectrum such as ^{144}Ce, ^{90}Sr, ^{42}Ar or ^{106}Ru. Both types provide pure neutrino flux with well-defined energy spectrum and absolute rate that can be precisely measured, creating an excellent opportunity to test the fourth neutrino hypothesis using oscillometry.

3.1 Oscillometry

The unambiguous way to address the existence of a fourth neutrino state is the determination of the oscillation pattern in the distance-dependent flux of a pure neutrino flavor source over the entire oscillation length. A detector-source distance similar to the expected oscillation length is thus necessary:

$$L \sim \frac{L_{osc}[m]}{2} = 1.24 \frac{E_{\bar{\nu}_e}[MeV]}{\Delta m^2_{new}[eV^2]}. \tag{11}$$

Electron antineutrinos produced in radioactive decays have energies up to a few MeV. Assuming a $\Delta m^2_{new} \sim 1 \, eV^2$, which is preferred by the different anomalies seen in the past terrestrial neutrino data, the optimum source-detector distance is $\mathcal{O}(1\,m)$. Therefore, large liquid-scintillator (LS) detectors such as Borexino [39], KamLAND [40], or SNO+ [41] are able to perform precise neutrino oscillometry since they are big enough to fully cover the spatial pattern of $\bar{\nu}_e$ oscillations into a fourth neutrino state.

3.2 Neutrino Emitters

In the nineties, intense ^{51}Cr (~ 750 keV, $\mathcal{A}_0 \sim$ MCi) and ^{37}Ar (814 keV, $\mathcal{A}_0 \sim 0.4$ MCi) sources were used to test the radiochemical experiments Gallex and Sage. Such radioactive neutrino sources involve either β^+-decay or electron capture. Electron captures produce mono-energetic ν_e's allowing for a determination of L/E_ν by only measuring the interaction vertex position. Production of an ^{37}Ar source requires a large fast neutron reactor (which is not easily available), leaving ^{51}Cr as the best current candidate for sterile neutrino searches with ν_e sources. ^{51}Cr has a half-life of 27.7 days. It decays 90.1% of the time to the ^{51}V ground state and emits a 751 keV ν_e while 9.9% of the time it decays to the first excited state of ^{51}V and emits a 413 keV ν_e followed by a 320 keV γ. The large scale production of ^{51}Cr has been possible thanks to the relatively high ^{50}Cr neutron capture cross-section (~ 17.9 barns). Natural chromium is primarily composed of ^{53}Cr (9.5%), ^{52}Cr (83.8%) and ^{50}Cr (4.35%). The ^{53}Cr and ^{50}Cr isotopes have similar neutron capture cross-section. Under the irradiation of natural chromium, ^{53}Cr absorbs 2.5 neutrons every time a neutron is captured on ^{50}Cr, thus reducing the ^{51}Cr yield. Enrichment of natural chromium with ^{50}Cr is therefore necessary in order to produce a ^{51}Cr source with an activity of several MCi. Such enrichment is favorable for manufacturing a compact target, which is necessary for sterile neutrino searches. The material used by the Gallex experiment was enriched to 38.6% in ^{50}Cr while the Sage target was enriched to 92%. Because many isotopes have high neutron capture cross-sections, great care must be taken during the production and handling of the chromium rods in order to avoid high-energy gamma ray contamination from chemical impurities.

In a radiochemical experiment, the interactions of ^{51}Cr and ^{37}Ar neutrinos produce ^{71}Ge atoms via the ^{71}Ga(ν_e,e$^-$)^{71}Ge reaction. The ^{71}Ge atoms are chemically extracted from the detector and converted to GeH$_4$. Ge atoms are then placed in proportional counters and their number is determined by counting the Auger electrons released in the transition back to ^{71}Ga, which occurs with a half-life of 11.4 days.

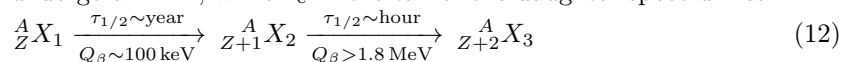In liquid scintillator experiments, the ν_e signature is provided by ν_e elastic scattering off electrons

(ES) of the molecules. The cross section is $\sigma(E_\nu) \sim 0.96 \times 10^{-44} \times E_\nu \, \mathrm{cm}^2$, where E_ν is the neutrino energy in MeV. This signature can be mimicked by Compton scatterings induced by radioactive and cosmogenic backgrounds, or by solar-ν interactions. An experiment running with a ν_e source then imposes the use of a very high activity source (5-10 MCi) to provide an interaction rate within the detector that will exceed the rate from solar ν, and to compensate the lack of solid angle due to the positioning of a source outside the detector (since the ES does not provide any specific signature of ν_e interaction).

3.3 Antineutrino Emitters

Antineutrino sources are non-monochromatic $\bar{\nu}_e$ emitters decaying through β^--decay. $\bar{\nu}_e$ are detected through the inverse beta decay (IBD) reaction $\bar{\nu}_e + \mathrm{p} \rightarrow e^+ + \mathrm{n}$. The IBD cross-section is $\sigma(E_e) \sim 0.96 \, 10^{-43} \times p_e E_e \, \mathrm{cm}^2$, where p_e and E_e are the momentum and energy (in MeV) of the detected e^+, neglecting neutron recoil, weak magnetism effects, and radiative second order corrections. The IBD cross-section is an order of magnitude higher than the neutrino scattering off electron cross-section at 1 MeV.

The $\bar{\nu}_e$ interaction signature is the time and space coincidence of two energy depositions in the liquid scintillator. The first energy deposition consists of e^+ kinetic energy deposition closely followed by the energy deposition of two 511 keV γ-rays from e^+ annihilation with an electron of the medium. It is called the prompt event, releasing a total visible energy of $\mathrm{E}_e = \mathrm{E}_\nu - (m_n - m_p)$ MeV. The second energy deposition originates from the neutron capture on a free proton, with an averaged capture time of the order of a few hundreds μs, which releases a 2.2 MeV deexcitation γ-ray. This is called the delayed event. The time coincidence between these two energy depositions suppresses any non-source backgrounds to a negligible level.

The background free IBD signature plus the relatively high IBD cross-section allow the source activity to be at the (tens of) kCi scale for sterile neutrino searches. A suitable $\bar{\nu}_e$ source must have a Q_β greater than 1.8 MeV to exceed the IBD energy threshold and a long enough lifetime ($\gtrsim$1 month) not to be limited by production and transportation time to the detector. Fulfillment of these two requirements is impossible for a single nuclei, since Q_β is anti-correlated with lifetime. We then looked for pairs of nuclei involving a long-lived low-Q nucleus decaying to a short-lived high-Q nucleus. Since the first isotope, the parent, has a much longer lifetime than its daughter, both nuclei are in equilibrium and the activity is driven by the parent. $\bar{\nu}_e$ emitted by the father has not enough energy to undergo an IBD, while $\bar{\nu}_e$ in the tail of the daughter spectrum can:

$$\,^A_Z X_1 \xrightarrow[Q_\beta \sim 100\,\mathrm{keV}]{\tau_{1/2} \sim \mathrm{year}} \,^A_{Z+1} X_2 \xrightarrow[Q_\beta > 1.8\,\mathrm{MeV}]{\tau_{1/2} \sim \mathrm{hour}} \,^A_{Z+2} X_3 \tag{12}$$

Four pairs fulfilling the above mentioned requirements have been identified in the nuclear databases and are presented in table 2, some of them also being reported in [64].

	^{144}Ce-^{144}Pr		^{106}Ru-^{106}Rh		^{90}Sr-^{90}Y		^{42}Ar-^{42}K	
$\tau_{1/2}$	285 d	7.2 min	372 d	30 s	28.9 y	64 h	32.9 y	12 h
Q_β (MeV)	0.319	2.996	0.039	3.54	0.546	2.28	0.599	3.52

Table 2: Possible nuclei pairs for a $\bar{\nu}_e$ source.

^{144}Ce, ^{106}Ru and ^{90}Sr are fission products found within nuclear reactor spent fuels, whereas ^{42}Ar is too light to be produced by fission processes. Furthermore, the production of ^{42}Ar needs two neutron captures, starting from stable ^{40}Ar. Because ^{41}Ar has a short lifetime of only 110 min and ^{40}Ar $(\mathrm{n},\gamma)^{41}$Ar reaction has a cross-section of only $\sim$0.4 barn, massive ^{42}Ar production is very difficult. Therefore, a solution consisting in the reprocessing and treatment of nuclear spent fuel rods is more convenient.

The probability of a nuclei to be created during fission processes in nuclear reactor fuel is called the fission yield and is given in percent [1]. However, the fission yield of a given nucleus does not take into account its possible decay to another nucleus, and is therefore not representative of the abundance of a given nuclei within spent nuclear fuel. The cumulative fission yield of an isotope is

---

[1] The sum of the isotopic fission yield gives 200 % because of the normalization with the number of fissions, not with the number of fissions products.

the number of nuclei of the considered isotope per fission when the reactor is at equilibrium. This quantity is then more interesting for our purpose of finding the best pair candidate because with a reasonable approximation (very long-lived isotopes never reach equilibrium), it represents a fission product abundance at reactor shutdown. Table 3 shows the ^{144}Ce, ^{106}Ru and ^{90}Sr cumulative fission yields for thermal fission of ^{235}U and ^{239}Pu, these two isotopes being the most fissioned isotopes in nuclear reactors. ^{144}Ce, ^{106}Ru and ^{90}Sr are clearly abundant fission products, but ^{106}Ru suffers from its rather low ^{235}U cumulative yield compared to ^{144}Ce and ^{90}Sr. Since ^{90}Sr-^{90}Y suffers from a relatively low Q_β leading to a small IBD reaction rate for a given activity, the ^{144}Ce $-^{144}$Pr pair is therefore the best candidate for a $\bar{\nu}_e$ source.

	Cumulative fission yield (%)		
	$^{144}_{58}$Ce	$^{106}_{44}$Ru	$^{90}_{38}$Sr
^{235}U	5.50 (4)	0.401 (6)	5.78 (6)
^{239}Pu	3.74 (3)	4.35 (9)	2.10 (4)

Table 3: Cumulative fission yield for thermal fission of ^{235}U / ^{239}Pu for ^{144}Ce, ^{106}Ru and ^{90}Sr [73].

4 ^{144}Ce $-^{144}$Pr antineutrino generator

The CeLAND experiment will use a ^{144}Ce $-^{144}$Pr source, which is the best compromise between production feasibility, intrinsic backgrounds and $\bar{\nu}_e$ interaction rate through the inverse beta decay reaction.

4.1 ^{144}Ce $-^{144}$Pr source features

With an atomic number Z=58, cerium belongs to the lanthanide elements. Natural cerium has an atomic mass of 140.116 g and is a soft, silvery, ductile metal which easily oxidizes in air. Cerium has two oxidation states (III and IV) and easily converts to CeO_2 in contact with oxygen.. Natural cerium contains four stable isotopes of mass 136 (0.195%), 138 (0.265%) and 140 (88.45%) and 142 (11.1%), respectively. Cerium is the most abundant rare earth element, making up about 0.0046% of the Earth's crust by weight.

4.1.1 Nuclear data

There is a considerable interest in the decay of ^{144}Ce since it is a prominent fission product. Nuclear data reported below are taken from the ENSDF database referring to [59, 60] for ^{144}Ce and [60] for ^{144}Pr.

F. Y.	$t_{1/2}$	1st β^- (keV)	2nd β^- (keV)	$I_{\gamma>1\,MeV}$	$I_{\gamma>2\,MeV}$	W/kCi
^{235}U: 5.2%	284.91d	318 (76%)				
		184 (20%)	2996 (99%)	1380 (0.007%)	2185	7.99
^{239}Pu: 3.7%		238 (4%)	810 (1%)	1489 (0.28 %)	(0.7%)	

Table 4: Summary of the features of ^{144}Ce $-^{144}$Pr pair. F.Y. are the fission yields of ^{144}Ce, $t_{1/2}$ the half-lives. β end-points are given for 1st and 2nd nucleus in the pair. The I_γ's are the intensities of the main γ-rays per β-decay above 1 and 2 MeV. The last column is the heat production in units of W/kCi.

The different cerium isotopes are listed in table 5. Up to now, 35 radioisotopes have been characterized, the most stable ones being ^{144}Ce with a half-life of 284.91 days, ^{139}Ce with a half-life of 137.640 days, and ^{141}Ce with a half-life of 32.501 days. The remaining radioactive isotopes have half-lives shorter than 4 days, most of them having half-lives shorter than 10 minutes. Note that the ^{136,138,142}Ce isotopes are predicted to undergo double beta decay but this process has never been observed.

Parent	Z	A	isotopic mass (u)	half-life	decay	daughter	spin/parity
^{119}Ce	58	61	118.95276(64)	200 ms	β^+	^{119}La	5/2+
^{120}Ce	58	62	119.94664(75)	250 ms	β^+	^{120}La	0+
^{121}Ce	58	63	120.94342(54)	1.1(1) s	β^+	^{121}La	(5/2)(+)
^{122}Ce	58	64	121.93791(43)	2 s	β^+	^{121,122}La	0+
^{123}Ce	58	65	122.93540(32)	3.8(2) s	β^+,p	^{123}La, ^{122}Ba	(5/2)(+)
^{124}Ce	58	66	123.93041(32)	9.1(12) s	β^+	^{124}La	0+
^{125}Ce	58	67	124.92844(21)	9.3(3) s	β^+,p	^{125}La,^{124}Ba	(7/2-)
^{126}Ce	58	68	125.92397(3)	51.0(3) s	β^+	^{126}La	0+
^{127}Ce	58	69	126.92273(6)	29(2) s	β^+	^{127}La	5/2+
^{128}Ce	58	70	127.91891(3)	3.93(2) min	β^+	^{128}La	0+
^{129}Ce	58	71	128.91810(3)	3.5(3) min	β^+	^{129}La	(5/2+)
^{130}Ce	58	72	129.91474(3)	22.9(5) min	β^+	^{130}La	0+
^{130m}Ce			2453.6(3) keV	100(8) ns			(7-)
^{131}Ce	58	73	130.91442(4)	10.2(3) min	β^+	^{131}La	(7/2+)
^{131m}Ce			61.8(1) keV	5.0(10) min	β^+	^{131}La	(1/2+)
^{132}Ce	58	74	131.911460(22)	3.51(11) h	β^+	^{132}La	0+
^{132m}Ce			2340.8(5) keV	9.4(3) ms	IT	^{132}Ce	(8-)
^{133}Ce	58	75	132.911515(18)	97(4) min	β^+	^{133}La	1/2+
^{133m}Ce			37.1(8) keV	4.9(4) h	β^+	^{133}La	9/2-
^{134}Ce	58	76	133.908925(22)	3.16(4) d	EC	^{134}La	0+
^{135}Ce	58	77	134.909151(12)	17.7(3) h	β^+	^{135}La	1/2(+)
^{135m}Ce			445.8(2) keV	20(1) s	IT	^{135}Ce	(11/2-)
^{136}Ce	58	78	135.907172(14)	Observationally Stable			0+
^{136m}Ce			3095.5(4) keV	2.2(2) μs			10+
^{137}Ce	58	79	136.907806(14)	9.0(3) h	β^+	^{137}La	3/2+
^{137m}Ce			254.29(5) keV	34.4(3) h	IT(99.22%)/β^+(.779%)	^{137}Ce/^{137}La	11/2-
^{138}Ce	58	80	137.905991(11)	Observationally Stable			0+
^{138m}Ce			2129.17(12) keV	8.65(20) ms	IT	^{138}Ce	7-
^{139}Ce	58	81	138.906653(8)	137.641(20) d	EC	^{139}9a	3/2+
^{139m}Ce			754.24(8) keV	56.54(13) s	IT	^{139}Ce	11/2-
^{140}Ce	58	82	139.9054387(26)	Stable			0+
^{140m}Ce			2107.85(3) keV	7.3(15) μs			6+
^{141}Ce	58	83	140.9082763(26)	32.508(13) d	β^-	^{141}Pr	7/2-
^{142}Ce	58	84	141.909244(3)	Observationally Stable			0+
^{143}Ce	58	85	142.912386(3)	33.039(6) h	β^-	^{143}Pr	3/2-
^{144}**Ce**	58	86	143.913647(4)	284.91(5) d	β^-	^{144m}**Pr**	0+
^{145}Ce	58	87	144.91723(4)	3.01(6) min	β^-	^{145}Pr	(3/2-)
^{146}Ce	58	88	145.91876(7)	13.52(13) min	β^-	^{146}Pr	0+
^{147}Ce	58	89	146.92267(3)	56.4(10)	β^-	^{147}Pr	(5/2-)
^{148}Ce	58	90	147.92443(3)	56(1) s	β^-	^{148}Pr	0+
^{149}Ce	58	91	148.9284(1)	5.3(2) s	β^-	^{149}Pr	(3/2-)
^{150}Ce	58	92	149.93041(5)	4.0(6) s	β^-	^{150}Pr	0+
^{151}Ce	58	93	150.93398(11)	1.02(6) s	β^-	^{151}Pr	3/2-
^{152}Ce	58	94	151.93654(21)	1.4(2) s	β^-	^{152}Pr	0+
^{153}Ce	58	95	152.94058(43)	500 ms	β^-	^{153}Pr	3/2-
^{154}Ce	58	96	153.94342(54)	300 ms	β^-	^{154}Pr	0+
^{155}Ce	58	97	154.94804(64)	200 ms	β^-	^{155}Pr	5/2-
^{156}Ce	58	98	155.95126(64)	150 ms	β^-	^{156}Pr	0+
^{157}Ce	58	99	156.95634(75)	50 ms	β^-	^{157}Pr	7/2+

Table 5: Cerium isotopes. EC refers to Electron capture and IT to Isomeric transition. There are 10 meta states.

The half-life of the ^{144}Ce, 284.91 days ($\tau = 411.04$ days), is long enough for uploading of irradiated fuel from the nuclear reactor, transportation to the reprocessing facility, extraction of cerium, cerium source packaging and transportation to the detector site. It is however not too long, mini-

mizing the mass of reprocessed fuel and source material within the detector. The ^{144}Ce is therefore a very good compromise, suitable for a year time scale experiment. The source compactness requirement imposes the time elapsed prior to the source manufacturing time. The time period must be shorter than a few years (typically three) starting from the end of the nuclear fuel irradiation within the reactor core.
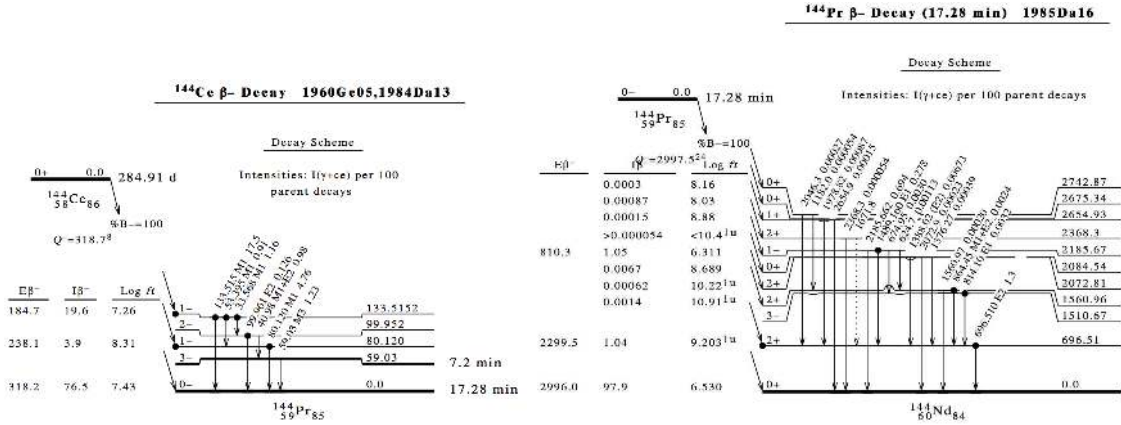
Figure 5: (left) Decay scheme of ^{144}Ce. The two intensities sum to give total transition intensity from each energy level in percent. Energies of γ rays and levels are given in keV. (right) Decay schemes of the 17.3-min ^{144}Pr. Energies of γ rays and levels are given in keV.

A major concern regarding an $\bar{\nu}_e$ source is the rate and energy of accompanying γ-rays because it is a source of backgrounds for the detection of $\bar{\nu}_e$, and requires substantial shielding to comply with safety rules for anybody working in the vicinity of the source during production, transportation, and deployment. For an artificial $\bar{\nu}_e$ source, the main channel of γ-ray background is the long-lived γ-emitting isotopes of the same chemical element simultaneously extracted from irradiated nuclear fuel. In case of cerium, all isotopes except ^{139}Ce and ^{144}Ce (see table 5) decay fast enough not to be sources of γ backgrounds for the CeLAND experiment. ^{139}Ce cumulative fission yield is only 2.10^{-9} for ^{239}Pu and 9.10^{-12} for ^{235}U, at least 7 orders of magnitude lower than ^{144}Ce. Therefore ^{139}Ce gamma background yield is negligible. The main concern then arises from the decay of ^{144}Ce and its daughter ^{144}Pr deexcitation. The decay scheme of ^{144}Ce and of ^{144}Pr ground and exited states are shown in figure 8 and 5, respectively. The most dangerous source of background originates from the energetic 2185 keV γ produced by the decay through excited states of ^{144}Pr (see also table 6). This γ line has a branching ratio of 0.7%. Starting from a β activity of 75 kCi, this leads to a huge γ activity of 525 Ci ($1.9\ 10^{13}$ Bq) that must be attenuated through a thick high-Z shielding material, such as tungsten alloy. In addition, it is necessary to guarantee a low level of radio-impurities containing long-lived γ radioisotopes during the cerium chemical extraction procedure. Specifically, rate of γ-rays above 1 MeV from impurities must be smaller than 10% of the 2185 keV γ rate, leading to an activity smaller than 50 Ci/75 kCi, ensuring that this gamma background is negligible.

4.1.2 Decay heat

The ^{144}Ce $-^{144}$Pr pair releases heat through the collisions of β and γ radiations with atoms. Details of the ^{144}Ce $-^{144}$Pr decay chain and heat production per decay branch are given in table 6. A ^{144}Ce $-^{144}$Pr source releases 7.991 ± 0.044 Watt/kCi (0.56 %) of thermal power per units of activity, mostly coming from β decay electrons (95.72 %) contained in the cerium oxide.

A 75 kCi activity therefore corresponds to an overall 599.3 W thermal power. For CeLAND phase 1, the heat will be dissipated within the 3 kilotons of water circulating in the outer detector. Heat release as a function of time (and decreasing activity) is given in table 7. Starting with a 75 kCi source at the KamLAND site, thermal power decreases down to 387 W after 6 months (roughly corresponding to a 50 kCi activity). Two years after the start of the data taking with an initial 75
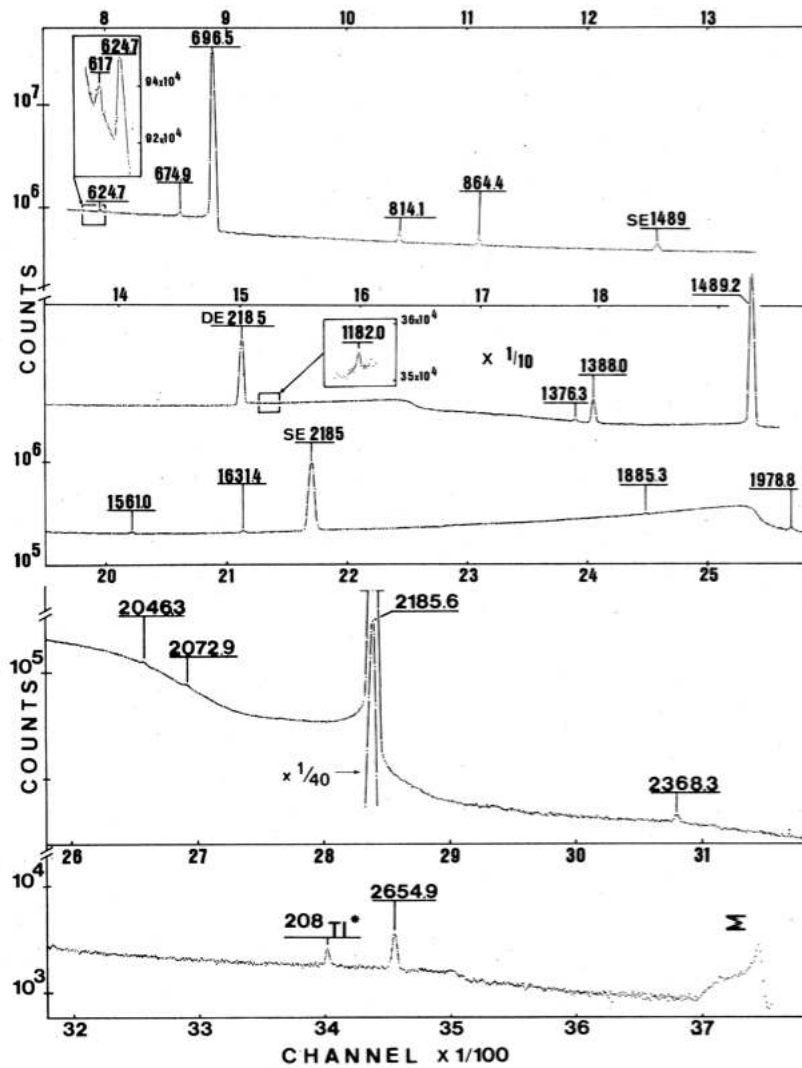
Figure 6: γ ray spectrum of ^{144m}Pr isomers in equilibrium with ^{144}Ce, measured with a 17% HPGe detector [61]. Energies are in keV; the energy dispersion is 0.76 keV/channel. SE and DE stand for single and double escape peaks, respectively. An asterisk denotes a γ ray from the background; the Σ symbol indicates summing a peak from 2185.6 and 696.5 keV γ rays.

kCi source, the heat release drops down to 101 W (corresponding to about 13 kCi). After 10 years of running with an initial 75 kCi source, the heat release should be roughly 0.1 W, corresponding to an activity of 10 Ci.

	End-point energy (keV)	Energy (keV)	Intensity (%)	Dose (keV / Bq)
^{144}Ce β branches				
	318.7 (8)	91.1 (7)	76.5 (5)	69.7 (7)
	238.6 (8)	66.1 (6)	3.90 (20)	2.58 (13)
	185.2 (8)	50.2 (6)	19.6 (4)	9.84 (23)
Total			100	82.1 (11)
^{144}Ce γ lines				
		133.515 (2)	11.09 (19)	14.8 (3)
		99.961 (15)	0.04 (4)	0.04 (4)
		80.12 (5)	1.36 (6)	1.09 (5)
		59.03 (3)	0.0004 (5)	0.00058 (3)
		53.395 (5)	0.1 (8)	0.053 (4)
		40.98 (10)	0.257 (16)	0.105 (7)
		33.568 (10)	0.2 (22)	0.067 (8)
Total				16.2 (4)
^{144}Pr β branches				
	2997.5 (24)	1222 (11)	97.9 (4)	1196 (5)
	2301 (24)	895 (11)	1.04 (20)	9.31 (18)
	1436.5 (24)	526.27 (99)	0.0014 (3)	0.0074 (16)
	924.7 (24)	322.85 (92)	0.00062 (5)	0.002 (16)
	913 (24)	306.77 (96)	0.0067 (10)	0.0206 (3)
	811.8 (24)	267.19 (93)	1.05 (4)	2.81 (11)
	342.6 (24)	98.9 (78)	0.00015 (3)	0.00015 (3)
	322.2 (24)	92.33 (77)	0.00087 (9)	0.0008 (8)
	254.6 (24)	71.11 (76)	0.0003 (10)	0.00021 (7)
Total			100	1208.2 (53)
^{144}Pr γ lines				
		2654.9 (2)	0.00015 (3)	0.0039 (7)
		2368.3 (3)	$5.4\,10^{-5}$ (13)	0.0013 (3)
		2185.66 (7)	0.694 (15)	15.2 (3)
		2072.9 (2)	0.00023 (3)	0.0047 (6)
		2046.3 (2)	0.00027 (5)	0.0055 (11)
		1978.82 (10)	0.00087 (8)	0.0173 (16)
		1560.97 (10)	0.00020 (3)	0.0031 (4)
		1489.17 (5)	0.278 (5)	4.14 (7)
		1388.02 (10)	0.00672 (9)	0.0933 (12)
		1376.27 (10)	0.00039 (4)	0.0054 (6)
		1182 (3)	$5.37\,10^{-5}$	$6.34\,10^{-4}$
		864.45 (10)	0.0024 (3)	0.0209 (23)
		814.1 (10)	0.0032 (3)	0.0262 (22)
		696.51 (3)	1.342	9.35
		674.95 (10)	0.003 (3)	0.0199 (18)
		624.7 (1)	0.00113 (3)	0.00704 (18)
Total				28.9 (4)
Total β branches				1290.3 (64)
Total γ lines				45.1 (8)
Total X lines				3.2 (1)
Total CE and Auger lines				9.5 (3)
Grand total				1348.0 (75)

Table 6: Energy released for branch of ^{144}Ce and ^{144}Pr decays [73]. The ^{144m}Pr is neglected, due to its very low branching ratio (<1%) and its very low β decay probability (0.7 %) compared to γ isomeric transition (99.3 %).

Time (months)	0	6	12	18	24	36	48	60	120
Activity (kCi)	75.0	48.1	30.8	19.8	12.7	5.2	2.1	0.9	0.01
Activity (PBq)	2.78	1.78	1.14	0.73	0.47	0.19	0.08	0.03	0.0004
Heat (W)	599	384	246	158	101	41.7	17.1	7.05	0.0829

Table 7: ^{144}Ce $-^{144}$Pr activity and heat release as a function of time after the production. After 20 years, the activity is only 50 Bq.

4.1.3 Electron and antineutrino spectra

Electron and antineutrino spectra of a given β decaying radioisotope are simply related by energy conservation at the β-branch level. However, ^{144}Pr undergoes several β-branch decays with forbidden transitions and makes the ^{144}Pr antineutrino spectrum calculation difficult. Here is presented a direct calculation of the neutrino spectrum using the Fermi theory [78]. With E and p the total energy and momentum of the beta particle, the differential energy spectrum at the β branch level writes:

$$N(E)dp = Kp^2(E - E_0)^2 F(Z, E)dp, \tag{13}$$

with E_0 the end point energy. Fermi theory is a simplified description of β decay and needs to be corrected for various atomic and nucleus effects, which especially affect low energy electrons and hence high energy neutrinos. The ^{144}Pr spectrum is carefully modeled by including major corrective effects to the Fermi spectrum:

$$N(E)dp = Kp^2(E - E_0)^2 F(Z, E)L_0(E, Z)C(E, Z)R(E, M)G(E, Z)S(Z, E)B(E, Z)dp, \tag{14}$$

where:

- $L_0(E, Z)$ and $C(E, Z)$ takes respectively into account the finite size and mass of the nucleus considering both electromagnetic and weak interactions [79] (Fermi theory considers the nucleus to be point-like with an infinite mass)

- $R(E, M)$ is the recoil effect on the phase space factor and the nucleus Coulomb field, with M the nuclear mass [79]

- $G(E, Z)$ corresponds to radiative corrections (i.e. emission of virtual or real photons in the decay process) [80]

- $S(Z, E)$ is the screening of the beta particle [81] by the atomic electrons

- $B(E, Z)$ is the weak magnetism correction [75] (similar to induced electromagnetic current in a moving Coulomb field, but for weak interactions).

All corrective terms have the structure $1 + \delta(E, Z, M)$. These terms represent up to a few percent correction to the Fermi spectrum (eq. 13). The recoil effects turn out to have a nearly negligible impact (0.013% correction) on the uncorrected Fermi spectrum. Figure 7 compares the relative weights of each of the above-mentioned corrections. Any theoretical uncertainty associated to a correction is propagated in the spectrum. The dominant source of uncertainty comes from the weak magnetism effect. Following the prescription of [75], a linear correction is used to estimate the weak magnetism effect. The linear coefficient is estimated following two approaches. The first one uses a theoretical calculation based on the so-called impulse approximation [75]. The second one assumes that vector currents in a β-decay behave the same as for an electromagnetic decay process (conserved vector current hypothesis), allowing to make an analogy between a Fermi type (vector current) β-decay and an electromagnetic M1 γ-decay. In such an approximation, the linear coefficient of the weak magnetism correction can be estimated using the measured M1 electromagnetic form factors of a reduced (and hardly representative) sample of 13 nuclei, which present the same nucleus quantum number change in their respective M1 γ-decay and β-decay[75, 77]. Both methods give strongly different outputs and the first one is retained as the default estimation. The second largest uncertainty is associated to the screening correction term, and comes from the modeling of the distribution of the atomic electrons. Various models along with their different results [81] are used to conservatively estimate the uncertainty on the screening correction.
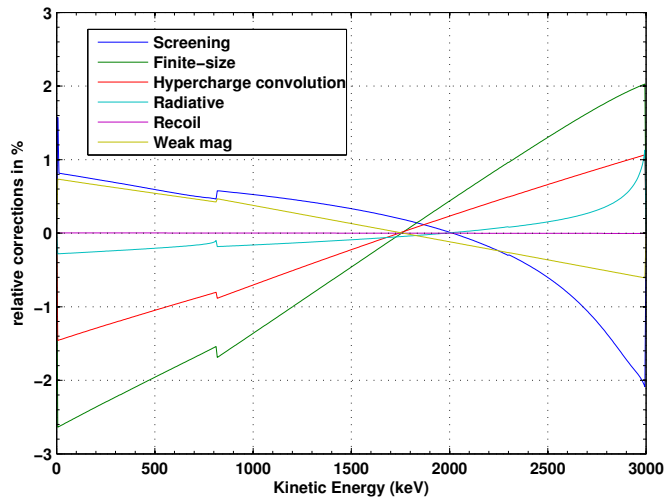
Figure 7: Comparison of the relative amplitudes for the corrective terms. The weak magnetism correction has been computed here using the impulse approximation. See text for further details.

The ^{144}Pr neutrino spectrum is modeled combining the eight most important β-branches (highest branching ratios) using data from National Nuclear Data Center. They are summarized in table 8. The resulting neutrino spectrum along with errors associated to the uncertainties in the considered corrections is displayed in figure 9. As a cross-check, the electron and antineutrino spectra have been calculated using the Bestiole code [76]. Bestiole has been originally developed to predict antineutrino spectra from nuclear reactors (which comprises thousands of β-branches) using available experimental informations in different nuclear databases. The agreement with our modeling, once integrated with the same binning configuration, is very good. The ^{144}Pr antineutrino spectrum exhibits the same two discontinuities at 811.8 keV and 2301 keV, which are the end-point energies of the β-branches of intensity of 1.05% and 1.04%, respectively. The next five branches do not have a strong influence on the total spectrum and have a negligible contribution.

In order to refine our knowledge of the source spectrum, β spectroscopic measurements using cerium nitrate samples prepared by PA Mayak are scheduled to begin by the end of 2013. Our ^{144}Pr β spectrum modeling will be adjusted to the data to reduce uncertainties on the shape of the neutrino spectrum, and especially to constrain the weak magnetism correction, which dominates the shape error budget.

The full ^{144}Ce $-^{144}$Pr antineutrino spectrum is displayed in figure 8. The ^{144}Ce lifetime is much shorter than that of ^{144}Pr, which enables us to assume secular equilibrium. The first peak corresponds to the ^{144}Ce parent β decay with an end-point energy of 318.7 keV. $\bar{\nu}_e$ originating from ^{144}Ce β decay are hence not detectable through the inverse beta decay process. The second broad peak corresponds to the ^{144}Pr β decay with an end-point energy of 2997.5 keV. The $\bar{\nu}_e$ spectrum which lies above the inverse beta decay threshold of 1.8 MeV represents about 50% of the ^{144}Pr emitted $\bar{\nu}_e$.

Branching ratio (%)	Quantum numbers	Q_β(keV)	type
97.9	0^+	2997.5	First non unique forbidden
1.05	1^-	811.8	Allowed
1.04	2^+	2301.0	First unique forbidden
$6.70 \cdot 10^{-3}$	0^+	913	First non unique forbidden
$1.4 \cdot 10^{-3}$	2^+	1436.5	First unique forbidden
$8.7 \cdot 10^{-4}$	0^+	322.2	First non unique forbidden
$6.2 \cdot 10^{-4}$	2^+	924.7	First unique forbidden
$3.0 \cdot 10^{-4}$	0^+	254.6	First non unique forbidden

Table 8: ^{144}Pr β-branches included in the analytical model, sorted by decreasing probability
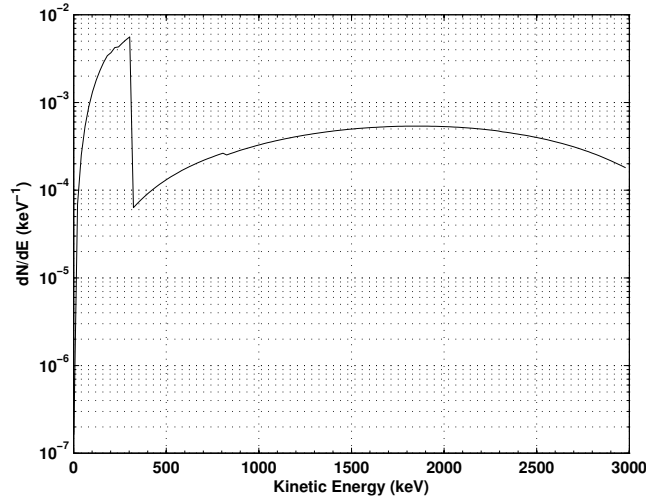
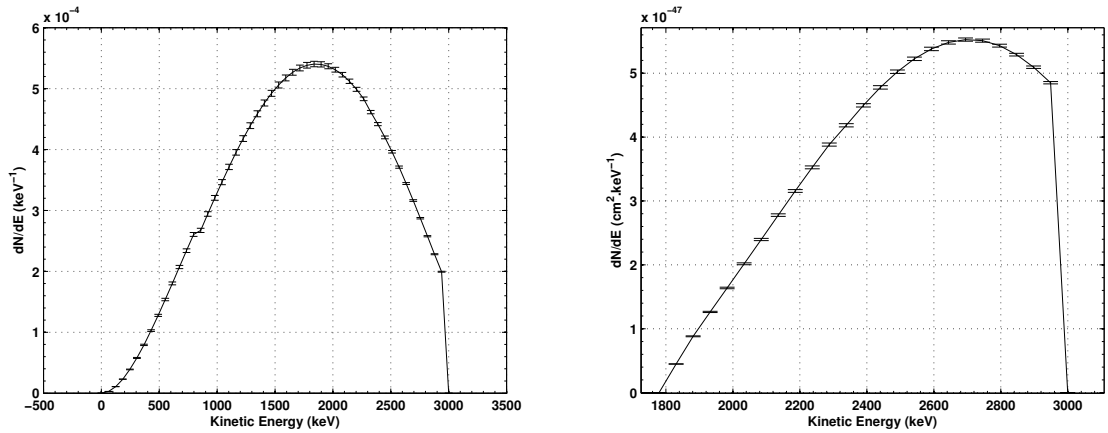Figure 8: ^{144}Ce $-^{144}$ Pr antineutrino emitted spectrum assuming secular equilibrium.

Figure 9: Left panel: Complete neutrino spectrum for eight first β-branches of ^{144}Pr with optimistic weak magnetism correction. Right Panel: Differential observable neutrino spectrum from ^{144}Pr including the IBD cross-section.

As a first application, our model was used to predict the rate of inverse beta decay events that will be detected in KamLAND. It is also used to estimate the uncertainty coming from the shape of the neutrino spectrum. The visible energy spectrum in the detector is obtained by multiplying the IBD cross-section to the $^{144}\text{Ce} -^{144}\text{Pr}$ antineutrino spectrum. It is shown on the right panel of figure 9. The threshold of IBD is high enough to neglect all influence of Cerium as its transition end-points are well below 1.8 MeV. The cross-section is computed using prescriptions from [81], with a pre-factor of $9.61 \ 10^{-48} \ \text{cm}^2/\text{Mev}^2$ (which has a negligible 0.1% uncertainty due to the neutron lifetime uncertainty). Then, the expected event rate in the KamLAND detector is

$$N_\nu = N_{Ce}\rho_p F_{geo} \int_0^\infty \sigma_{IBD}(E_\nu) S(E_\nu) dE_\nu, \tag{15}$$

where $\rho_p = 6.62 \times 10^{22} \ \text{cm}^{-3}$ is the density of protons in the KamLAND detector and F_{geo} is a geometric factor (with dimension of a length) including the detector and source geometry. For a cylindrical source of 13.5 cm diameter and 13.5 cm height, positioned 9.3 m away from the center of a spherical detector of 6.5 m radius, $F_{geo} = 1.10$ m. Considering a pessimistic scenario where some backgrounds escaping the source (gammas and neutrons) remain unshielded, a tighter 6 m radius fiducial cut was also considered, giving $F_{geo} = 0.85$ m. N_{Ce} is the number of Cerium decays corresponding to a data taking period T:

$$N_{Ce} = \int_0^T A_0 e^{\frac{-\ln(2)t}{T_{1/2}}} dt \tag{16}$$

$$= A_0 \frac{T_{1/2}}{\ln(2)} \left[1 - e^{\frac{-\ln(2)T}{T_{1/2}}} \right],$$

where A_0 is the initial source activity. With a 75 kCi source and a 18-month data taking period, 24165±189 (resp. 18673±146) antineutrinos are expected to be detected in KamLAND considering a 6.5m radius (resp. 6 m radius) fiducial volume cut. The quoted uncertainties come from the β-spectrum modeling only, assuming a weak magnetism correction factor calculated using the impulse approximation, as done in [22].

4.2 $^{144}\text{Ce} -^{144}\text{Pr}$ source production

From an extraction and production perspective, cerium is a rather abundant element present at the 5.5% and 3.7% levels in the fission products of uranium and plutonium, respectively (see table table 3).

4.2.1 Activity

As agreed with the PA Mayak, the activity of the cerium antineutrino generator will be of 85^{+15}_{-10} kCi in ^{144}Ce beta activity at delivery in Yekaterinburg. Taking into account the 6-8 % precision of the activity measurement at Mayak, one guarantee there is a 90 % probability to get the activity higher than 75 kCi. Remaining free space in source (inner) capsule, if any, will be filled with additional radioactive cerium oxide if available at the end of the production, up to 100 kCi. Thus, depending on the fuel age and extraction process there is a possibility that the source activity may be above 75 kCi at the beginning of the experiment at KamLAND.

4.2.2 Geometry

The spatial extent of the CeO_2 source material must be small compared to the neutrino oscillation length ($L_{osc} \sim 1$ m for $\Delta m^2 \sim 1 \, eV^2$ neutrino mass splittings considered above) for the successful oscillometry measurement. Moreover, the size of the source will directly increase the size and mass of the shielding, thus requiring a source to be small and compact, with an extension of a few tens of centimeter.
But several constraints have to be considered. The first consideration is that only a mixture of all cerium isotopes produced during irradiation can be practically separated from spent nuclear fuel, since isolating the ^{144}Ce would require a very difficult isotopic separation. So the ^{144}Ce content of the cerium oxide is limited by fission yields and cooling time. Secondly, the CeO_2 will be manipulated in hot cells, which requires cylindrically shaped capsule and limit the achievable density of cerium oxide to 4.0 ± 1 g/cm^3.

Finally, the largest capsule that can be handled routinely in Mayak hot cells is 15 cm in height and diameter, and safety requirements impose a double container in stainless steel. Mayak will provide the capsules, 4 mm thick for the outer capsule and 3 mm thick for the inner capsule. Adding the necessary mechanical gap of 0.5 mm, a maximum of 13.5 cm in diameter remains available for the CeO_2.

4.2.3 Spent fuel seeds

Preliminary computations have been done to study the amount of cerium produced within VVER reactors for various condition of irradiation. The SAS2H (SCALE-4.4) ORIGEN-S software from Oakridge was used by the MePhi group in Russia. The content of ^{144}Ce in spent nuclear fuel (SNF) elements depends on the irradiation history and on the reactor neutron spectrum. The ^{144}Ce isotope mostly results from the decay of ^{144}Cs and is abundantly produced in the fissions of ^{235}U and ^{239}Pu. The abundance of cerium among produced rare earth elements is about 22%. Taking these numbers at their face values, about 15 SNF elements would be needed to achieve 75 kCi of ^{144}Ce, but we will see that technical considerations force us to consider about five to ten times more SNF elements to reach the desired activity.

To optimize the selection of SNF elements in order to maximize the ^{144}Ce content per fuel element units of mass, a dedicated study was performed by Mayak and MePhi. The general guidelines to extract the fuel with the highest constant of ^{144}Ce are the following:

1. Select SNF with shortest time of irradiation, since the fission yield for ^{144}Ce of ^{239}Pu is lower than ^{235}U.

2. Select SNF with highest energy release during the last irradiation, since the ^{144}Ce content increases with the fission rate and therefore power.

3. Select SNF with the lowest burn-up, for the same reason than the first guideline.

Following these guidelines, a specific activity of ^{144}Ce in the range 31 to 35 Ci/g of SNF can be expected, corresponding to an absolute activity of 8 to 12 kCi per fuel SNF.

The usual cooling sequence of SNF consists is 3 years of cooling in the power plant storage pool followed by another 2-year period of SNF being stored at the reprocessing plant. Delivery of fresher SNF to the reprocessing plant is possible but not conventional. This step would maximize the amount of activity within a small volume and significantly reduce the amount of SNF needed to produce a ^{144}Ce source with 75 kCi activity. Each gained month in the source manufacturing process represents a gain of SNF material of the order of 10%. To guarantee that the source is compact enough to fit inside the Mayak capsule, the possibility of using SNF with a low cooling time has been considered and approved by Mayak.

The transport, by train, will probably use a TUK-6 container (or equivalent), which is categorized as a B(M) container according to the international classification and contains typically up to 3.8 tons of UO_2 (see figure 10). To keep the level of radiation within the limits for transportation from the reactor site to the reprocessing plant with a low cooling time fuel, the container may be not full or filled with a mix of long and low cooling time fuel.
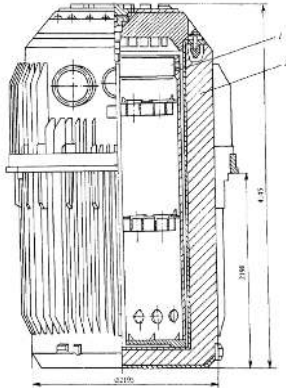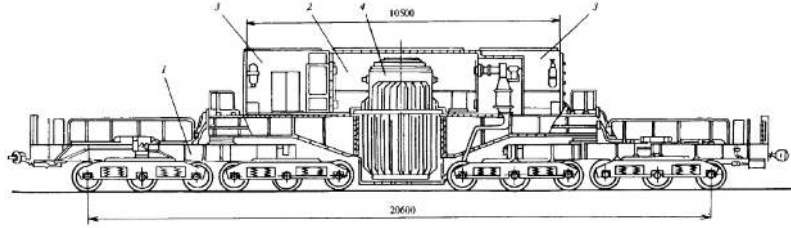
Figure 10: TUK-6 container (left) and carriage container (right) for spent fuel transportation from reactor to reprocessing plant. Each year about 58 tons of SNF are transported from Cola NPP to Radiochemistry plant RT-1 at PA Mayak (Ozersk, Chelyabinsk region).

An agreement between Rosatom and FSUE Mayak PA has been reached for delivery of 'fresh' SNF from the Kola Nuclear Power Plant (VVER-440, 3000 km north of Mayak) with a 1.7 to 2.0 year cooling period after the end of irradiation. The total mass of this special batch will be about 15 - 16 tons, including 7 - 8 tons with cooling time in the range of 580 till 640 days (1.6-1.75 years). The second part of SNF has cooling time 3.5 years and more. The burnup value of this "fresh" fuel will be in the range of 48 - 51 MW.d/t.

4.2.4 Spent fuel cooling time and mass of CeO_2 containing 75 kCi of ^{144}Ce

The ratio of ^{144}Ce in cerium extracted from SNF as a function of time t, assuming ^{144}Ce is the only cerium long-lived cerium isotope is,

$$\chi(t) = \frac{\text{mass}(^{144}\text{Ce}, \, t)}{\text{mass}(\text{Ce}, \, t)} = \frac{\text{mass}(^{144}\text{Ce}, \, t)}{\text{mass}(^{144}\text{Ce}, \, t) + \text{mass}(^{\text{stable}}\text{Ce})} = \frac{m_{144}(t)}{m_{144}(t) + m_{\text{stable}}} \tag{17}$$

According to MePhi (private communication during the CeLAND meeting in Paris, 22 July 2013), the content of ^{144}Ce in cerium with $t_c = 3$ years after the end of irradiation is:

$$\chi(3) = \chi_3 = 0.6^{+0.1}_{-0.15} \, \%$$

Here t_c is an arbitrary reference cooling time, used by MePhi for standard simulations. The mass of stable cerium can be written:

$$m_{\text{stable}} = \frac{m_{144}(3)}{\chi_3} - m_{144}(3) = \frac{(1 - \chi_3) \, m_{144}(3)}{\chi_3} \tag{18}$$

and the mass of ^{144}Ce is:

$$m_{144}(t) = m_{144}(0) \, e^{-\lambda t} = m_{144}(3) \, e^{-\lambda(t - t_c)}$$

with $\lambda = \ln(2)/\tau_{1/2} = 2.8158 \, 10^{-8} \, \text{s}^{-1}$. Then the ^{144}Ce mass ratio as a function of time t is:

$$\chi(t) = \frac{m_{144}(3) \, e^{-\lambda(t - t_c)}}{m_{144}(3) \, e^{-\lambda(t - t_c)} + \frac{(1 - \chi_3) \, m_{144}(3)}{\chi_3}} = \frac{\chi_3 \, e^{-\lambda(t - t_c)}}{1 - \chi_3 + \chi_3 \, e^{-\lambda(t - t_c)}} \tag{19}$$

The ^{144}Ce mass ratio is plotted on the left panel of figure 11. The source mass is related to the ^{144}Ce activity $\mathcal{A}(t)$ through:

$$\mathcal{A}(t) = \lambda \, N_{144}(t) = \frac{m_{144}(t) \, \mathcal{N}_a \, \lambda}{144} \Leftrightarrow m_{144}(t) = \frac{144 \times \mathcal{A}(t)}{\mathcal{N}_a \, \lambda}. \tag{20}$$

with $\mathcal{N}_a$ the Avogadro number. Finally, the source mass is given by:

$$m_{\text{source}}(t) = m_{144}(t) \times \frac{176}{144} + m_{\text{stable}}(t) \times \frac{174}{142} \simeq \frac{\mathcal{A}(t)}{\mathcal{N}_a \, \lambda \, \chi(t)} \, (176.5 - 0.5\chi(t)) \tag{21}$$

24
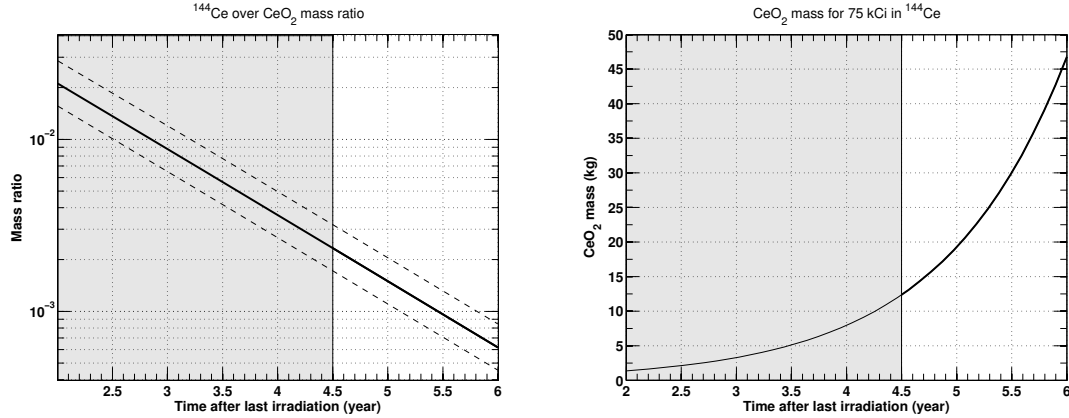
Figure 11: Left: ^{144}Ce/CeO$_2$ mass ratio as a function of time after last irradiation at the reactor (and its uncertainty band computed from reactor core simulations). Right: Mass of CeO$_2$ for a 75 kCi activity in ^{144}Ce as a function of the cooling + production time. The antineutrino generator should be realized with maximum cooling + production time of about 4.5 years in order to fit enough radioactive material inside the inner capsule (assuming a cerium oxide density of 4 g/cm^3).

The mass of CeO$_2$ required to achieve an activity of 75 kCi in ^{144}Ce, is given as a function of time in the right panel of figure 11. Assuming a 2-year cooling time and 1 year of production, the source mass included is between 4.8 kg and 6.4 kg. The last case corresponds to a cylinder of 15.4 cm in height and diameter with a minimal density of 3 g/cm^3. With all the parameters taken at their baseline values, the source mass is 5.45 kg, its volume is 1.36 liter corresponding to a cylinder of 12.0 cm in height and diameter. Considering the uncertainty on density and χ_3, the largest capsule has been validated (15 cm in the external diameter of the outer capsule, 13.5 cm in the internal diameter of the inner capsule).

4.2.5 Cerium production line

The Federal State Unitary Enterprise Mayak Production Association is a Russian spent fuel reprocessing facility located in the city of Ozersk, which performs the reprocessing of Russian SNF. It can reprocess spent fuel from various nuclear power plants (VVER, BN-600, and BN-350) as well as from research reactors, atomic-powered ships and submarines.
Russia reprocesses its SNF with the PUREX process which extracts uranium and plutonium. A secondary and optional phase can extract a highly concentrated waste of rare-earth elements (REEs), and a final step allows to separate through liquid chromatography a specific element, such as samarium used for powerless lights.

Standard reprocessing at the radiochemical plant

Procedures of spent fuel processing, starting from cutting and digestion through standard PUREX process to preparation of the required feed for further individual radionuclides separation are depicted in figure 12.
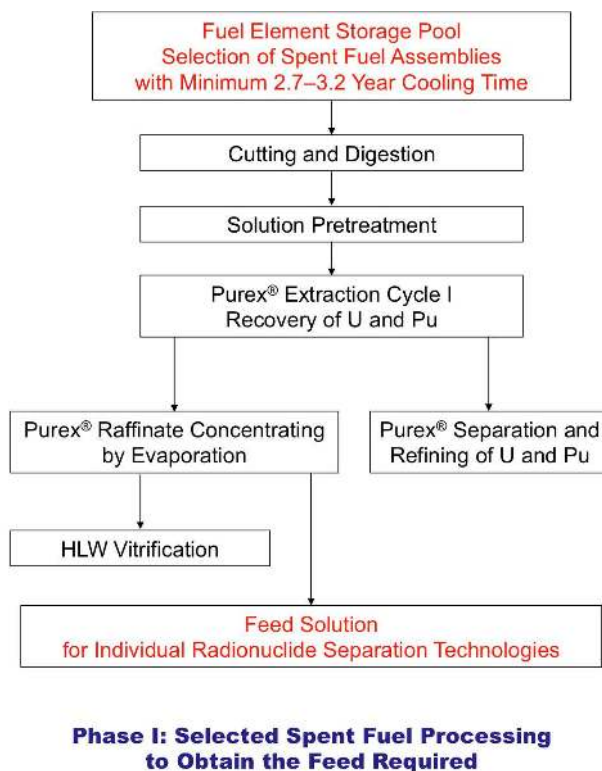
Figure 12: First procedures of PUREX process and Selected Spent Fuel Processing to obtain the required feed for further individual radionuclides separation.

First step is cutting of the ends of fuel assemblies (FA) by electroarc process. Then fuel part of FA is cut into small pieces and dissolved by nitric acid. The resulting solution is in form of pulp with superfine components of graphite, silicone and other elements. These components can affect the following chemical procedures. This is why one of important stages of reprocessing is clearing of the pulp by high-molecular organic flocculating agent and filtration on bulk filter made of stainless steel metallic spheres and natural minerals.

Procedure of U, Th and Np recovery (PUREX process) is the extraction process using multistage mixer settlers with the mixture of tributyl phosphate and hydrocarbon solvent. A similar process is implemented by COGEMA (France) and BNFL (UK). After recovery of U, Pu and Np, PUREX raffinate is transported to another distant workshop of Radiochemical Plant for its concentrating by evaporation. During the evaporation procedure a large quantity of nitric acid is recovered from the raffinate for its reiterative use. Due to big volume of communication pipeline (the distance of about 1.5 km) the minimum batch of PUREX raffinate which is transported is about several tens of cubic meters of the solution. Such a volume of the PUREX raffinate is equivalent to about 10 tons of SNF. It means that minimum quantity of SNF of certain quality we should select is about 10 tons.

Most of raffinate after evaporation procedure is directed to vitrification unit for disposal of high radioactive waste in form of phosphate glasses. This is one of main task for the Radiochemical Plant RT1 of PA Mayak in the framework of Russian program of closed fuel cycle.

Sometimes, accordingly to special request from Customers, a part of PUREX raffinate is pumped to another distant workshop, Radioisotope plant, for recovery of radioisotopes for medicine, scientific and industrial applications. Before pumping the solution is diluted by water to improve the mobility of this pulp.

Additional reprocessing at radioisotope plant

First operation at Radioisotope plant is recovery of 137Cs isotope by sorption procedure (see figure 13). At the radiochemical plant the raffinate passed two stages of concentration and purification of REE and TPE concentrate by double oxalate precipitation. First and second oxalate

procedure consists of oxalate precipitation of REE and TPE followed by dissolving the precipitate by nitric acid (digestion of oxalate). Precipitation of oxalates allows to separate the bulk of impurities present in the raffinate and to obtain relatively pure REE and TPE group. Main impurities which should be removed are Cesium (^{137}Cs) and Strontium (^{90}Sr), and chemical elements after corrosion (Fe, Ni, Cr).
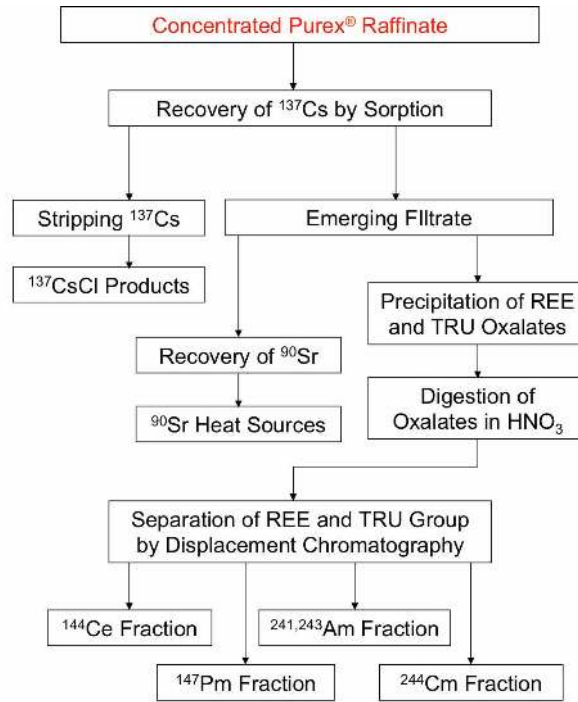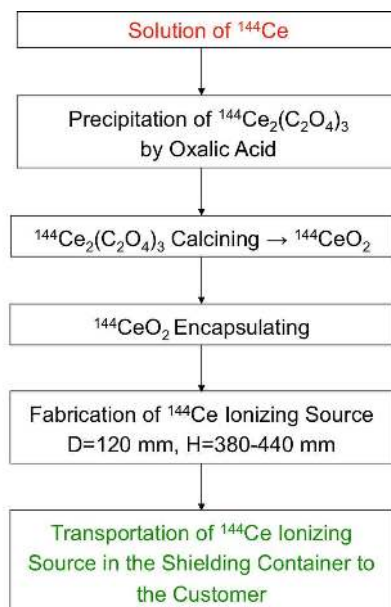

Figure 13: Individual radionuclides separation and refining.

Cerium Recovery

REE and TPE concentrate after correction by means of nitric acid are transferred by a pipeline to the chromatographic facility for separation of REE and TPE at the distance of about 500 m. The pipeline and additional vessels should be purified before this procedure.

Separation of cerium is performed by complexion displacement chromatography (CDC) using a series of columns, the first one being a sorption column and the others being separating columns. REEs are sorbed as a uniform band in the sorption column and are later separated using a series of columns packed with a resin containing retaining ion (Ni_2^+, Cu_2^+, H^+, etc.).

Figure 14: Schematic view of the cerium extraction process.

The main role of the retaining ions is to decompose the REE complex during the entire separation process and to favor repeated sorption-desorption cycles. The complexes of the eluent with the retaining ion should be stronger than those with the ions being separated. The sorption of the retaining ion on the resin should be weaker than that of the ions being separated. To separate REEs, a complexing agent containing displacing ions, NH_4^+, or Na^+, is used. The sorption of this agent is stronger than that of REEs. When a column is washed with this agent, NH_4^+ cations substitute REE_3^+ cations. As a results, the resin is transformed into the NH_4^+ form and REE ions form complexes with the eluent (EDTA). These complexes are decomposed by reaction with the resin in the form of the retaining ion Ni_2^+. The released REE ions are sorbed again and displace Ni_2^+. Thus, separate REE bands are formed in the columns. The order of these bands corresponds to the strength of the REE complexes (see figure 15). A diagram of the cerium extraction process is given in figure 14. An generic output of the chromatography is given in figure 15.
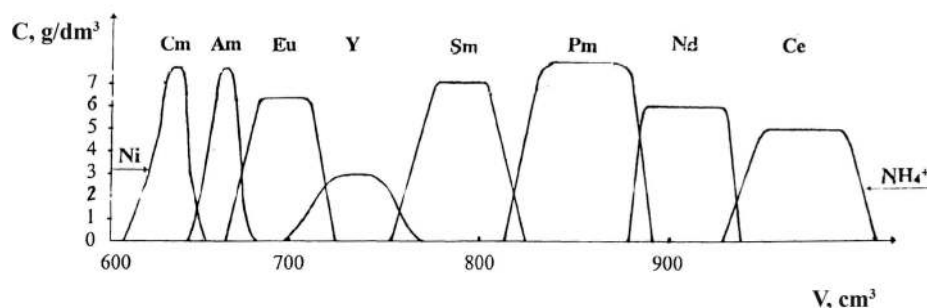

Figure 15: Selection of cerium through displacement chromatography. We note here that cerium if far away from curium and americium which guarantee a low concentation of neutron emitter impuritites in the final product.

4.2.6 ^{144}Ce source pressing and encapsulation

The source will be encapsulated in a cylindrical sealed double stainless steel container, the outer capsule having a 15 cm external diameter. The outer capsule will be 4 mm thick, the inner capsule 3 mm thick, and the mechanical gap will be 0.5 mm (to be confirmed by Mayak), leading to an inner capsule with a 13.5 cm in internal diameter (see figure 16 for a preliminary design proposed by CEA before Mayak constraints were known). The final design is ongoing. The capsules will be welded inside a hot cell (argon-arc welding). The tightness of the capsules will be tested using the Mayak's standard helium leakage test. The capsule will be certified by Mayak according to the ISO 9978-92 (Radiation protection - Sealed radioactive sources - Leakage test methods) regulation.
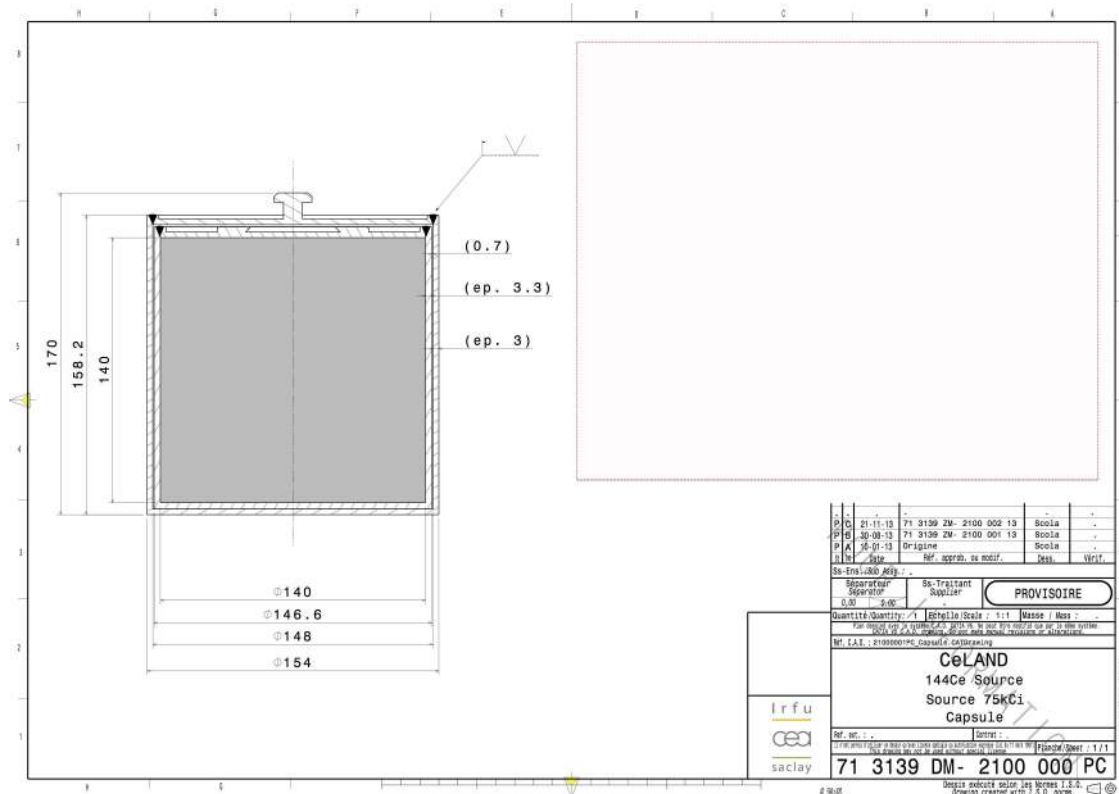

Figure 16: *Preliminary* 75 kCi ^{144}Ce $-^{144}$ Pr source capsule (cylinder with a diameter of 15 cm height and radius). Dimensions have to be updated, and a new design of the lid holder (mushroom-like) is necessary for proper manipulation inside the hot cells.

The cold pressing of the cerium oxide will be done in a hot cell at PA Mayak. In principle, a density of 5 g/cm^3 can be achieved since the CeO$_2$ has a theoretical density of 7.2 g/cm^3, but it could be as low as 3 g/cm^3. This is being checked with large samples in laboratory. The current density is expected to be 4 ± 1 g/cm^3. Prior to insertion, the cerium oxide will be pressed under the form of large solid pellets, with a diameter slightly smaller than the capsule.

Finally, the CeO$_2$ material and source container will be qualified as SFRM (Special Form of Radioactive Material). This is a mandatory step prior to the source container insertion within the tungsten shielding.

The CeLAND CeO$_2$ source production scenario assumes a 1-year production time between SNF arrival at the PA Mayak reprocessing facility and source delivery in Japan. Mayak's schedule is slightly shorter, about 10 months.

4.2.7 Target contamination

^{144}Ce will be extracted from spent nuclear fuel elements. Though expected to be very small, contamination of the final ^{144}Ce source with other radio-elements is unavoidable. The extraction

process leads to a small contamination from other REEs and minor actinides, that may be however relevant for realizing a neutrino experiment.

The REE contaminants are γ and β emitters, which could bias the activity measurement or participate to γ-induced accidental background. The contamination in REEs must therefore be small enough to provide a negligible contribution to activity, a requirement easily achieved through the CDC method used at PA Mayak. Because the source has to be shielded against 2.185 MeV ^{144}Pr γ-rays, any γ-rays from contaminants will be shielded as well. As explained in section 5, the γ attenuation length is close to its minimum at 2.2 MeV and will therefore drives the shielding dimensions.

Actinides are produced in a reactor core through successive neutron captures and beta decays from ^{238}U, as shown by figure 17. On one hand, they are α, β and γ emitters feeding long decay chains that require similar high-Z shielding than for REE contaminants. On the other hand, the heavy neutron rich actinides could be more hazardous since they also undergo Spontaneous Fission (SF). This emission of several γ-rays and neutrons is therefore a potential source of correlated background for the CeLAND experiment.
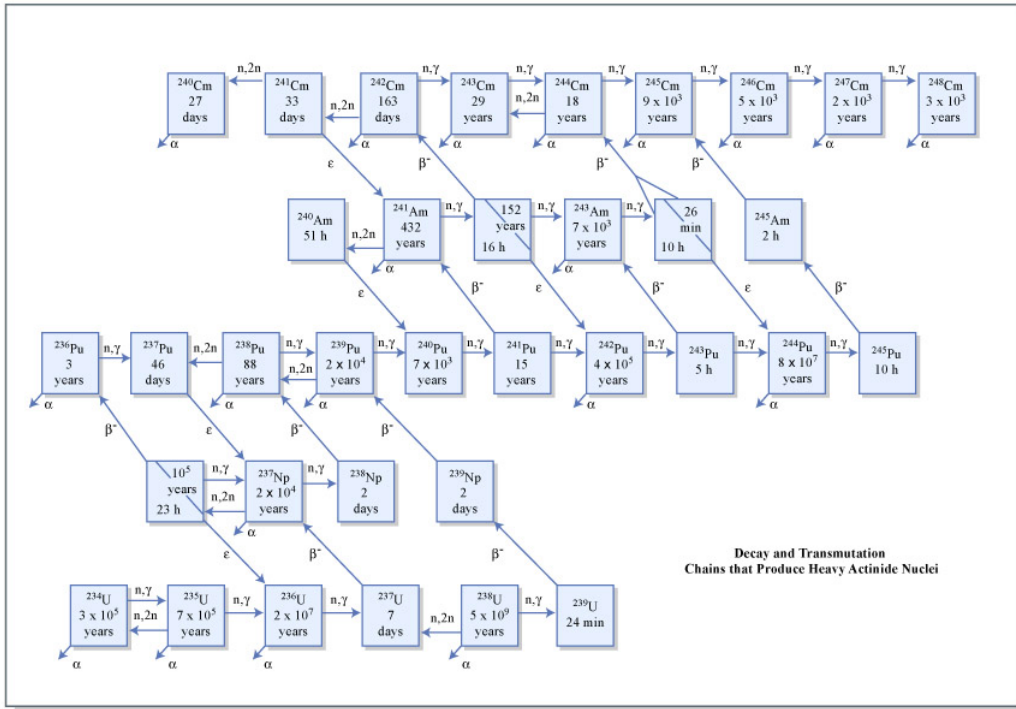

Figure 17: Production of minor actinides during irradiation of a reactor core.

Our contamination specifications are consequently the following:

- Thermal power of nuclides other than ^{144}Ce and ^{144}Pr should be less than 0.1 % of the thermal power delivered by ^{144}Ce and ^{144}Pr (7.991 ± 0.044 W/kCi), in order to guarantee the precision of the calorimetry measurement;

- Gamma activity above 1 MeV should be less than 0.1 % of the beta activity of ^{144}Ce;

- Activity of spontaneous fission radio impurities to be defined by Saclay in collaboration with the MePhi institute, ICP institute and Isoflex USA.

Since the attenuation corresponding to 2.185 MeV γ-rays is very close to the minimal attenuation length of tungsten, any high energy γ-rays (above 1 MeV) will at least be as attenuated as the 2.185 MeV γ-rays from ^{144}Pr. The 0.1% ^{144}Ce beta activity specification on γ-rays therefore ensures that the most active γ-rays will come from the ^{144}Pr 2.185 MeV γ emission (0.7% branching ratio). Thus, the gamma radiation shielding dimensions should only be driven by the activity of the ^{144}Pr 2.185 MeV γ-ray.

4.2.8 Source induced background

The CeLAND source could potentially add backgrounds to the signal measurement through decays of ^{144}Ce and ^{144}Pr (β^- electron, gamma, bremsstrahlung) or through decays of impurities (see previous section), if deployed too close or inside the KamLAND target volume. Since the ^{144}Ce is extracted from spent nuclear fuel, a particular concern is the presence of heavy minor actinides that undergo SF with non negligible branching ratios (reaching 74 % for ^{250}Cm), emitting γ-ray cascades and several fast neutrons.

4.2.8.1 Accidental backgrounds First, β^- decays of ^{144}Pr emit 2.185 MeV γ-rays (0.7% branching ratio), which lie both within the prompt and delayed energy windows. The biological shielding should be able to provide enough attenuation for deployment outside the tank (an additional plate could be placed between the shielding and the buffer tank). However, a deployment at the center of the detector would require much more shielding.

Second, neutrons from SF can scatter out of the source despite the high-Z shielding. Escaping neutrons can be captured on the detector materials, such as hydrogen in water, oil or in the liquid scintillator, consequently emitting 2.2 MeV γ-rays both affecting the prompt and delayed energy windows. As opposed to the 2.185 MeV γ-rays, which can be easily attenuated through the high-Z shielding, neutron induced background might dominate any other source of backgrounds despite a much lower activity in actinide's SF, which depends on the ^{144}Ce contamination with heavy minor actinides.

4.2.8.2 Correlated backgrounds The only correlated backgrounds induced by the source come from SF. Fast neutrons can reach the liquid scintillator target and make a proton recoil faking the prompt signal and slow down until being captured in the liquid scintillator, with the same coincidence time than a neutrino signal. Fortunately, the hydrogen-rich buffer oil separates the source from the target liquid scintillator, and fast neutrons have great chance to loose energy through scattering before the target. Moreover, detector response to fast neutron is affected by quenching and fast neutrons rarely give more than 1.022 MeV of visible energy (IBD energy threshold). This background should therefore not affect the experiment.

The multiple neutron background is potentially more hazardous. Spontaneous fission releases several neutrons in two opposite beams (neutrons are actually released by the two energetic fission fragments and are therefore strongly boosted), of which two can be scattered in the detector direction and then be captured on hydrogen inside or close to the target. The γ-rays resulting from the two captures could fake an IBD signal. Table 9 shows the half-life, branching ratios to spontaneous fission and specific neutron activities for all americium, curium, berkelium and californium isotopes with half-life higher than 180 days. The nuclei of interest are the curium and californium isotopes with an even mass number (^{244,246,248,250}Cm and ^{248,250,252}Cf). All americium isotopes and other curium and californium isotopes with odd mass number have negligible branching ratios. Berkelium isotopes have very short half-life period, and nuclei heavier than californium (Es, Fm) can be safely ignored since they are produced in negligible quantities in a reactor core and have a very short half-life period. It is worth noting that the mean number of neutron released per SF N increases with the nucleus mass number, following roughly $N = 0.1094A - 23.94$ in our mass range. For instance, ^{252}Cf releases 50 % more neutrons per SF than ^{241}Am (3.6 and 2.4 respectively).

The specific activities of the relevant heavy minor actinides have to be weighted by their abundance in spent nuclear fuel to correctly estimate the level of multiple neutron correlated background in the KamLAND detector. First, nuclei with odd mass number generally have large fission cross-sections, leaving radiative capture as a minor deexcitation process. Second, fresh nuclear fuel does not contain any isotope heavier than ^{238}U. All heavy minor actinide isotopes are then produced through a long chain of successive neutron captures and β^- decays, with the fission trap on odd nucleon number isotopes. The burn-up of spent nuclear fuel has then to be large enough to start producing heavy elements. Such threshold in burn-up of course increases with the isotope mass. Moreover, in power plant, reactors are generally operated at constant power with low enriched fuel. The neutron flux is then roughly constant, and the mass of ^{238}U is so large that it can be considered constant. The production of heavy actinide isotope with mass number A+1 depends of neutron flux, cross-section, decays and mass of isotope A. The mass ratio between an heavy actinide isotope A and the following isotope A+1 is therefore expected to be constant once the threshold in burn-up of isotope A+1 is reached. Available data show that the total mass of a given

curium isotope with even mass number A is roughly a factor 10^2 more than the following even isotope A+2. This effect should then counterbalance the increase of SF branching ratios with mass number. Detailed simulations are ongoing to precisely estimate heavy isotope abundance is spent nuclear fuel.

Isotope	Half-life	Branching ratio to SF	Specific neutron activity (neutron/g)
^{241}Am	432 y	$4 \cdot 10^{-12}$	1.2
^{242m}Am	141 y	$4.7 \cdot 10^{-11}$	46
^{243}Am	7370 y	$3.7 \cdot 10^{-11}$	0.72
^{243}Cm	29 y	$5.3 \cdot 10^{-11}$	$2.6 \cdot 10^2$
^{244}Cm	18 y	$1.4 \cdot 10^{-6}$	$1.2 \cdot 10^7$
^{245}Cm	8500 y	$6.1 \cdot 10^{-9}$	$1.1 \cdot 10^2$
^{246}Cm	4730 y	$3 \cdot 10^{-4}$	$1.0 \cdot 10^7$
^{248}Cm	$3.5 \cdot 10^4$	0.083	$4.2 \cdot 10^7$
^{250}Cm	9000 y	0.74	$1.5 \cdot 10^{10}$
^{249}Bk	320 d	$4.7 \cdot 10^{-10}$	$9.4 \cdot 10^4$
^{248}Cf	333 d	$2.9 \cdot 10^{-5}$	$5.4 \cdot 10^9$
^{249}Cf	351 y	$5 \cdot 10^{-9}$	$2.5 \cdot 10^3$
^{250}Cf	13 y	$8 \cdot 10^{-4}$	$1.1 \cdot 10^{10}$
^{251}Cf	898 y	$1 \cdot 10^{-7}$	$2.0 \cdot 10^4$
^{252}Cf	2.65 y	0.030	$2.2 \cdot 10^{12}$

Table 9: Spontaneous fission properties of minor actinide isotopes with half-life > 0.5 y

The most abundant curium isotope is ^{244}Cm, with a specific neutron activity comparable to ^{246}Cm and ^{248}Cm. According to our preliminary GEANT4 simulations, the correlated background induced by ^{244}Cm is 5000 events per year in the KamLAND detector, with a 6 m radius fiducial volume cut and assuming a contamination of 10^{-9}Bq/Bq. This assumption is taken from a limit on the level of contamination by minor actinides observed in Promethium production. However, the amount of multiple neutron correlated background in KamLAND is expected to be lower, because Cerium is more efficiently separated from actinides than Promethium using the complexion displacement chromatography method (see figure 15).

A neutron shielding solution, using saturated boric water surrounding the tungsten alloy shielding, is envisaged if the contamination in heavy minor actinides turns out to be non negligible. Commercial tungsten alloys are known to resist to boric water at room temperature. Corrosion test are currently being performed to clearly demonstrate that point.

4.2.9 Summary

Below are summarized the specifications of the source in the standard scenario that we will rely on in estimating the physics and sensitivity reach of the CeLAND project:

1. Spent fuel cooling time less than 2 years prior to transportation to PA Mayak;

2. Source beta activity of 85^{+15}_{-10} kCi of ^{144}Ce at delivery ;

3. Chemical form of cerium is CeO_2 with density 4 ± 1 g/cm^3;

4. External diameter of the capsules is 15 cm, internal diameter is 13.5 cm ;

5. Samples of cerium from the same production batch will be provided with the source.

5   High-Z gamma ray shielding

The most serious source of backgrounds is the decay of the ^{144}Nd 1^- excited state, which emits a 2.185 MeV γ-ray with a 0.7% intensity (see table 4). The bremsstrahlung of the ^{144}Pr β particles

might also be another source of backgrounds. The source must be shielded by a thick high-Z absorber to attenuate these backgrounds to the required level. With a theoretical density of 19.3 g/cm^3, tungsten is widely used in radiation shielding applications and is among the best suited candidate for this purpose.

5.1 Attenuation of γ rays in CeLAND

The total interaction cross-section of $\sim$MeV γ rays with matter is equal to the sum of three partial cross-sections: $\sigma = \sigma_f + \sigma_c + \sigma_p$, where σ_f is the photoelectric effect cross-section, σ_c is the Compton interaction cross-section and σ_p is the pair creation cross-section. A beam of gamma radiation passing through a layer of absorber material of thickness x will be exponentially attenuated: $I(x) = I_0 e^{-\left(\frac{\mu}{\rho}\right)\rho x}$, where I_0 is the intensity of the incident beam and μ/ρ is the mass attenuation coefficient. This coefficient is taken from [68] for each CeLAND material that will be later considered in our γ ray attenuation calculations. The μ coefficient definition is $\mu = \sigma \times n$, where n is the atomic concentration in the material. In the MeV energy regime, Compton scattering is the dominant interaction process so that the mass-attenuation coefficient is approximately the same for absorbers with different Z. This is because the probability of Compton scattering on atomic electrons is proportional to Z, making $\mu \sim \sigma_c Zn$ and $\mu/\rho \sim \sigma_c Z/M_A$ since $\rho = n \times M_A$, where M_A is the atomic mass. The inverse of the attenuation coefficient is $\lambda = 1/\mu$ and has units of length, so that it can be associated to a mean free path or an attenuation length. In other words, λ corresponds to the average distance the γ rays can travel in the absorber without interacting. The attenuation length dependence on the radiation energy is shown in figure 18 for typical materials making the CeLAND source and shielding, as well as the KAMLAND detector liquid scintillator. A summary of the relevant attenuation lengths used for the design of the CeLAND phase 1 and 2 shieldings is given in table 10. The design of the shielding of CeLAND phase 2 is still under consideration.

γ Absorber	Form	density	λ(1 MeV)	λ(2.185 MeV)	λ(2.655 MeV)
Tungsten alloy	solid	18.5 g/cm^3	0.817 cm	1.238 cm	1.288 cm
Mercury	liquid	13.5 g/cm^3	1.059 cm	1.644 cm	1.709 cm
CeO$_2$	solid	4.5$\pm$0.5 g/cm^3	3.358 cm	5.089 cm	5.293 cm
Sodium paratungstate	liquid	2.8 g/cm^3	5.358 cm	8.121 cm	8.446 cm
KamLAND scintillator	liquid	0.778 g/cm^3	18.000 cm	26.922 cm	30.132 cm
KamLAND buffer oil	liquid	0.762 g/cm^3	18.367 cm	27.472 cm	30.747 cm

Table 10: Summary of the attenuation lengths of γ absorber being considered for CeLAND. The biological shielding will consist of the source itself (CeO$_2$) surrounded by a thick tungsten alloy cylinder. It will be used as a γ-ray shielding for the CeLAND source deployment outside the detector target. In such a deployment scenario, further attenuation is naturally provided by the detector buffer oil and liquid scintillator. For deployment inside the KamLAND sphere, a shielding solution using heavy liquids such as sodium paratungstate or mercury is being considered.

5.2 Biological protection

Any exposure to ionizing radiation presents risks of biological damage. As such, the tungsten alloy shielding must also act as a biological protection during source transportation and manipulation. After the source is produced, it will be inserted in the shielding in a hot cell by the Mayak reprocessing plant.
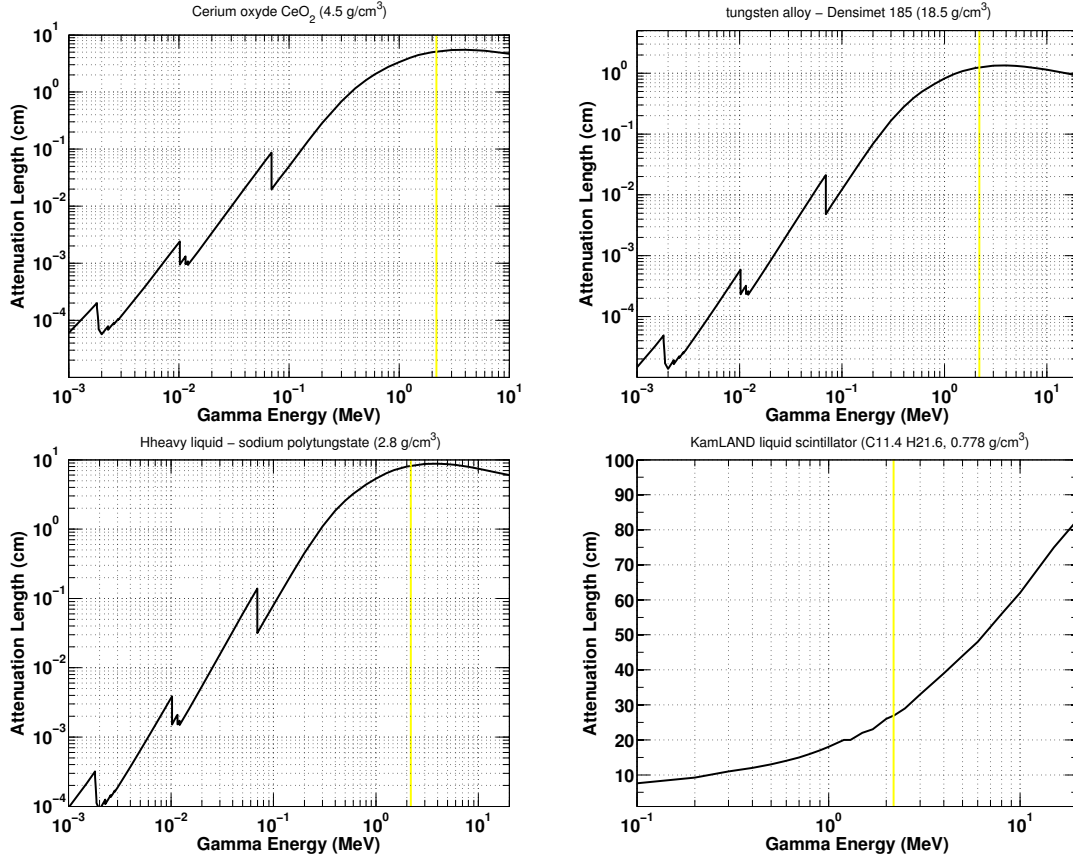
Figure 18: γ-ray attenuation lengths of some CeLAND materials. From left to right and top to bottom: cerium oxide, tungsten alloy, sodium paratungstate, and KamLAND liquid scintillator. The yellow line indicates the 2.185 MeV γ line produced by the decay through excited states of ^{144}Pr, which set the stronger constraint in the CeLAND source shielding design.

Chemical composition:	W (97%), Ni (1.5%), Fe (1.5%)
Density [g/cm^3]	18.5
Tensile strength at 20 °C [MPa]	800
Oxidation resistance	up to 600 °C
Thermal conductivity at 500 °C [W/mï¿œK]	70-90
Modulus of elasticity [GPa]	385
Hardness [HRC]	43
Yield strength at 20 °C [MPa]	600
Breaking elongation at 20 °C [%]	10
Coefficient of thermal expansion [10^{-6} K^{-1}]	5.0

Table 11: Mechanical and thermal properties of a typical tungsten alloy used for radiation shielding applications.

5.3 Equivalent dose

In order to assess the tungsten shielding dimensions, and especially the thickness, a number of factors must be taken into consideration:

- the nature of the ionizing radiation

- the strength of the source, which drives the intensity of the 2.185 MeV escaping γ-rays and thus the required attenuation to suppress this background

. the level of exposure of the area surrounding the source to ionizing radiations, with parameters such as time and distance from the source to evaluate the impact of escaping radiations on human bodies

The only ionizing radiation which eventually escapes from the source are γ-rays. As a first estimate, the equivalent dose (in Sievert) induced by a radioactive point source at the center of the shielding is computed. The absorbed dose (Gy/s) is given by:

$$D(J/g/s) = \mathcal{A}[Bq] \times \frac{1}{4\pi d^2 [cm^2]} \times \frac{\mu}{\rho}[g/cm^2]_{en} \times E[J] \tag{22}$$

where d is the source-person distance in cm, $\mathcal{A}$ is the source γ activity (in Bq) at the surface of the biological protection (i.e. after shielding), μ/ρ is the mass absorption coefficient (the fraction of energy of the gamma rays transferred to the medium, in cm^2/g), and E the energy of the escaping γ-ray (in Joule). Usually, $\mu/\rho \sim 25\,g/cm^2$ for γ-ray energies between 1 and 3 MeV. Furthermore it is almost medium independent, as explained in the previous section. The equivalent dose (in Sv) is calculated by multiplying the absorbed dose by the γ radiation weighting factor, w=1. After plugging in the correct numerical factors in equation 22, the equivalent dose becomes:

$$D(mSv/h) = 4.24 \times \mathcal{A}[Ci] \times E[MeV]/d[m]^2 \tag{23}$$

For a 75 kCi $^{144}Ce - ^{144}Pr$ source the activity corresponding to the 2.185 MeV γ rays (BR=0.7%) is 525 Ci. Considering a 16-cm thick spherical tungsten alloy shielding (d=18.5 g/cm^3, attenuation length of 1.26 cm at 2.185 MeV) the 2.185 MeV γ activity is reduced to 1.3×10^{-3} Ci at the surface of the biological protection. According to equation 23, the absorbed dose received at 1 m from the shielding is 14 μSv/h. As a comparison, the maximum tolerable annual dose for people working in environments with ionizing radiations is given by international regulations to be 20 mSv/y (see table 12), corresponding to about 1730 hours/y of exposure for somebody standing 1 m away from the source.

Criteria	IAEA dose Limit for exposed workers
Effective dose limit for workers in category A	20 mSv/y
Effective dose limit for workers in category B	6 mSv/y
Maximum effective dose allowed in any single year	50 mSv/y
Total work life (50 y)	400 mSv

Table 12: IAEA radiation dose limits for various working conditions.

A more accurate computation of the radiation dose using the GEANT4 simulation package has been performed. We consider here a 75 kCi $^{144}Ce - ^{144}Pr$ source in the form of CeO$_2$, encapsulated in a 5-cm radius sphere with a density of 4 g/cm^3. A sphere-shaped tungsten alloy shielding is simulated taking a typical composition for tungsten alloy with a density of 18.5 g/cm^3 [69]. The mechanical and thermal properties of this material are summarized in table 11. The simulated sphere is 21 cm diameter, leading to a uniform absorption thickness of 16 cm along any direction. The computed equivalent dose corresponding to the 2.185 MeV emission of ^{144}Pr is 0.930 mSv/h at the shielding contact. For the 1.489 MeV, the equivalent dose is 0.026 mSv/h at contact. At a distance of 1 m from the shielding surface, the 2.185 MeV radiation leads to a dose of 0.028 mSv/h. It is two times higher than the dose obtained with the simple computation of equation 23. This can be explained by the fact that the simulation also accounts for the degraded γ-rays that escape the shielding material. The radiation dose associated to the 1.489 MeV line 1 m away from the biological protection is 0.75 μSv/h. These results confirm that a tungsten alloy thickness of 16 cm is sufficient to meet the radiobiological protection requirements.

Finally a computation of the equivalent dose was performed by the CEA radio protection division. The two 2.185 MeV and 1.49 MeV γ-rays have been simulated through the same shielding geometry and material, using MCNPX v 2.7.a. Other γ rays are neglected, either because of their low energy or because of their weak intensity. The source was assumed to be CeO$_2$ with a density of 4 g/cm^3 and contained in a 1-mm thick capsule made of stainless steel with the same shape and dimensions as previously described. The equivalent dose rates are summarized in table 13. Though slightly higher, they are similar to our GEANT 4 computation.

γ rays energy (MeV)	Dose rate at 1 cm (mSv/h)	Dose rate at 1 m (mSv/h)
2.185	1.5	$4.2 \, 10^{-2}$
1.49	$3.9 \, 10^{-2}$	$<1.5 \, 10^{-3}$

Table 13: CEA - SPR computations of the radiation dose 1 cm and 1 m away from the shielding.

For completeness, the influence of electromagnetic radiation produced by the deceleration of the β-decay electrons when deflected by the atomic nuclei (Bremsstrahlung) has been studied. The mean free path of electrons in matter, δ, is taken from the Katz and Penfold formula [70]: $\delta(\mathrm{cm}) = 0.412/\rho E^n$, where ρ is the material density in g/cm^3, E is the energy of the electron in MeV, and the scaling index $n = 1.265 - 0.0954 \ln(E)$. The maximum mean free path of electrons of ^{144}Ce and ^{144}Pr is given in table 14 for stainless steel, cerium oxide, and a tungsten alloy. Bremsstrahlung spectra of ^{144}Ce and ^{144}Pr is computed using MCNPX. The obtained X-ray spectra are converted into dose rates using the software MERCURIAD v1.04. Details of the computation can be found in [74]. The dose rate induced by Bremsstrahlung of β electrons is less than 1 μSv/h at 1 cm and can thus be neglected in comparison with the dose rate directly induced by the 2.185 MeV γ-ray of the ^{144}Pr decay.

β energy (MeV)	Stainless Steel	CeO_2	Tungsten alloy
0.32	$1.1 \, 10^{-2}$ cm	$4.27 \, 10^{-3}$ cm	$2.2 \, 10^{-2}$ cm
3.0	$1.9 \, 10^{-1}$ cm	$8.0 \, 10^{-2}$ cm	$3.7 \, 10^{-1}$ cm

Table 14: CEA - SPR computations of the mean free path of electrons in stainless steel, cerium oxide, and a tungsten alloy.
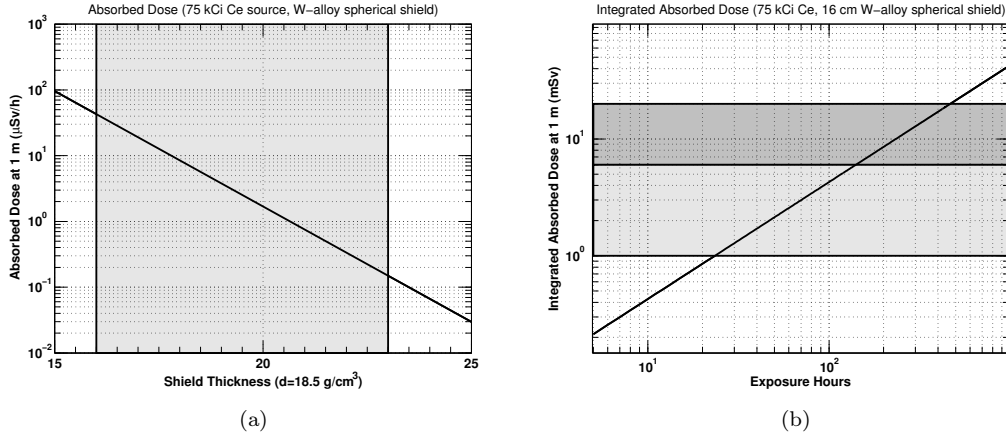

(a)

(b)

Figure 19: Left panel: absorbed dose received at 1 m from a spherical tungsten alloy shielding as a function of thickness. The gray area represent the range of thicknesses being considered for the CeLAND experiment, with a cylinder having a 16 cm minimum thickness. The maximum dose is 42 μSv/h. Right panel: Integrated absorbed dose for a 16-cm tungsten alloy shielding as a function of time, when standing next to the source (initial activity of 75 kCi). Category A and B equivalent dose limits are represented by the light and dark gray bands, respectively. A worker could stand more than 20 hours at 1 meter from the shielding before receiving an integrated dose of 1 mSv, assuming an activity of 75 kCi.

5.4 Insertion of the ^{144}Ce source inside the biological shielding

The ^{144}Ce source will be manipulated and inserted into the central shielding in a hot cell at the Mayak reprocessing plant. The hot cell has a 1.1 m high and 1.0 m wide single door and can contain up to 4 tons of material. The crane available in the area is certified to lift a maximum weight of 5 tons. The tungsten alloy shielding will be cleaned at Mayak to avoid surface contamination of the shielding after being manipulated in the hot cell. The ^{144}Ce source must be inserted in the shielding downwards from the top.

5.5 High-Z shielding (for the deployment next to KamLAND)

The characteristic signature of an inverse beta decay antineutrino interaction is the time and space coincidence of a prompt energy deposition (e^+ energy deposition) followed by a delayed energy deposition (neutron capture on hydrogen). The main background to the antineutrino signal are accidental coincidences between prompt-like (E>0.9 MeV) and delayed-like energy depositions (E>2.0 MeV) occurring within a time window taken as three neutron capture lifetimes on hydrogen (equivalent to about ΔT =772 µs), and within a volume of 10 m^3. If the prompt and delayed energy deposition positions can be reconstructed, an additional background rejection of a factor ΔV =1/100 can be achieved.

A dangerous source of accidental coincidences comes from the emission of energetic 2.185 MeV γ-rays from the decay of the 1^- excited state of ^{144}Nd (Table 4). 2.185 MeV γ-rays can easily mimic the signal neutron capture on hydrogen at 2.2 MeV and the signal of a positron above 0.9 MeV, generating an accidental coincidence signal. The rate of accidental coincidences must then stay small enough compared to the expected antineutrino interaction rate within the KamLAND detector (16000/y for phase 1). Hence, the reduction of the rate R$_\gamma$ of escaping γ-rays is a key parameter in computing the shielding dimensions. To first order, this requirement translates into: R$^2_{\gamma,\text{phase1}} \times \Delta t \times \Delta V \ll$ 16000/y leading to R$_{\gamma,\text{phase1}} \leq$ 5 Bq . Starting from an initial rate of 19.4 TBq for the 2.185 MeV γ-ray line (0.7% of 2.77 PBq), this requirement on the reduction of R$_\gamma$ imposes an attenuation of $\sim 10^{-12}$.

5.5.1 γ-ray absorption specification

In the first phase of the experiment, the ^{144}Ce $-^{144}$Pr emitter will be placed as close as possible from the steel tank within the circulating water shielding. The minimum foreseen distance from the center of the KamLAND detector is 9.6 m. The shielding thickness is computed taking into account additional attenuation provided by different media between the source and the liquid scintillator volume: water plus a 1-cm thick stainless steel vessel ($\lambda = 4.15$ cm) plus 2.5 m of mineral oil ($\lambda = 26.9$ cm). As a conservative assumption, the self-absorption of γ-rays within the CeO$_2$ capsule and the solid angle effect are not taken into account. Achieving a 10^{-12} attenuation in this geometric configuration finally leads to a 16-cm thick tungsten alloy (18.5 g/cm^3).

5.5.2 Radiopurity specification

An important remaining source of background could be the tungsten shielding itself, especially in the second phase of the experiment where the shielding will be in contact with the liquid scintillator. The activity induced by impurities inside the tungsten shielding are here required to be less than $\sim$1/10 of the activity of the 2.185 MeV γs able to escape the shielding without interaction. This requirement ensures the absence of a significant background contribution from the tungsten shielding. For the deployment in the outer veto or in a room close to the detector, conservative estimates can be computed as described in the previous section, by imposing a maximum tolerable background rate of R$_{\gamma,\text{phase1}} \leq$ 0.5 Bq. GEANT4 simulations have been run in the CeLAND phase 1 deployment scenario, with a 16 cm thick spherical shape tungsten alloy shielding placed 9.6 m away form the KamLAND detector center. Taking into account the most dangerous γ-ray lines emitted in the different primordial decay chains or nuclei, the maximum tolerable activities in ^{232}Th, ^{238}U, ^{40}K, ^{60}Co are the following:

- ^{232}Th (primordial, ^{232}Th-chain) : $\sim$0.3 Bq/kg

- ^{238}U (primordial, ^{238}U-chain) : $\sim$3 Bq/kg

- ^{40}K (primordial) : $\sim$120 Bq/kg

- ^{60}Co (anthropogenic) : $\sim$20 Bq/kg

Several tungsten alloy samples from different suppliers have been analyzed, with activities at the level of ten to hundreds of mBq/kg for the above-mentioned radioisotopes. They are hence all suitable for the CeLAND phase 1 deployment scenario of the cerium antineutrino generator in the KamLAND Outer detector.

5.5.3 Preliminary mechanical design

The shielding is made up of a hollow tungsten alloy cylinder with two cavities, each with different inner diameter and located at different depths: the source fits in the lower cavity at the center of the shielding and the upper cavity supports the plug to avoid direct radioactive leaks. The tungsten alloy shielding is 16 cm thick at minimum and weighs about 1.5 tons. It is represented in figure 20.
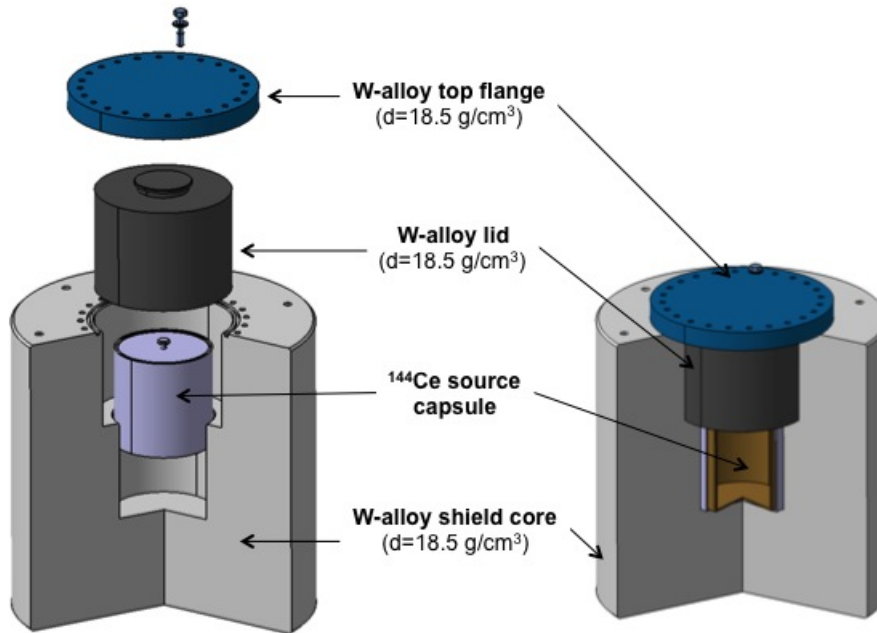
Figure 20: Sketch of the tungsten alloy shielding to be used for radiological protection for the deployment in the outer detector water (OD) or farther from the target liquid scintillator.

The final choice on the tungsten alloy material will mostly be driven by radiopurity requirements (see previous section). The upper cavity in the shielding is closed by a tungsten alloy lid. The tightness of the seal is achieved by a Helicoflex O-ring metallic gasket with good resistance to radiations and high temperatures. Captive screws hold the cap in order to ease its mounting in the hot cell. The final tightening of the screws will require a high torque and can be done outside the hot cell (the biological protection is ensured as soon as the cap is plugged on the top of the shielding). A 1 mm play between the outer capsule and the inner wall of the shielding lower cavity, as well as a 2 mm chamfer, should ease the insertion of the source in the shielding. Likewise, there is a 5/10 mm play between the plug and the inner wall of the shielding upper cavity. The loading of the capsule in the shielding should be done downwards from the top. 2 x 6 threaded M16 holes on the top and bottom shielding sides allow several handling operations: translation and rotation

in the hot cell (with a dedicated tool), insertion of the shielding in the transportation container, in the calorimeter, handling above the manhole at KamLAND or inside the detector. They also allow holding the shielding during measurements in the KamLAND detector or can be used to fix supports to protect the bottom surface of the shielding. These threaded holes will be protected by screws fitted with metallic gaskets to avoid trapping of any dust or any kind of radioactive particles. A preliminary technical drawing of the CeLAND source shielding is given in figure 21.
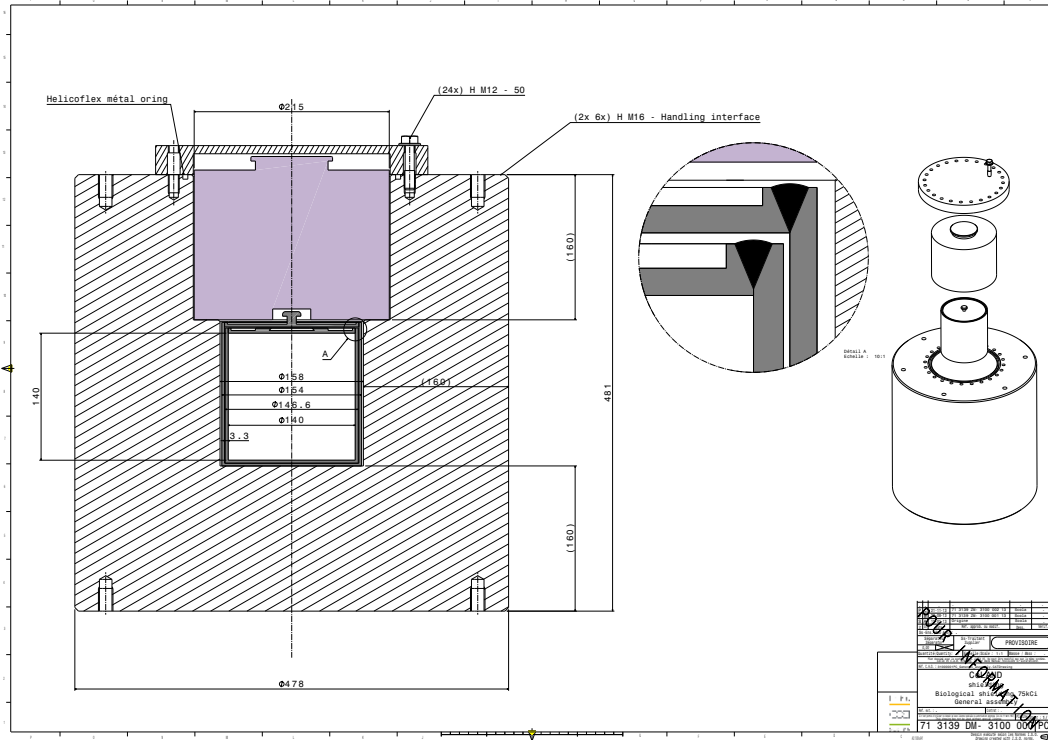
Figure 21: Preliminary drawing of the tungsten alloy shielding to be used for radiological protection as well as for the first phase of CeLAND, e.g. the deployment in the outer detector water (OD).

6 Source and shielding logistics

Various heavy elements needed for the experiment will be shipped between the different manufacturing places to Japan. Here is a summary of the major heavy shipments.

6.1 High-Z shielding transportation

Transport involving non radioactive material:
• shipment from Saclay to Mayak of the tungsten radiological protection ;
• shipment from Saclay to Kamioka of the equipment to measure its activity prior to deployment and of the tools used to manipulate the source ;
• if the shielding is not manufactured in France, calibration of the calorimeter will impose a transit through France.

6.2 ^{144}Ce $-^{144}$Pr antineutrino generator transportation

The most sensitive part is the transportation of the radioactive antineutrino generator between Mayak and Japan. Transport of radioactive materials must follow requirements stated in the reference document : Regulations for the Safe Transport of Radioactive Material (2009 Edition) issued by IAEA [IAEA09]. This document describe the type, characteristics and performance of containers used for these transports, the different forms of the radioactive material and the radiation level

and temperature outside the transport container.

In our case the parcel (or consignment) which will be transported is composed of the radioactive Cerium oxide pressed to reach a density around 4 g/cm^3 and placed inside a double sealed stainless steel container ; this object will be inserted in the tungsten shielding at Mayak and will be tightly closed by a top part in tungsten. Each capsule will be tested for leaks (Helium leak test) and according to ISO 9978-92 certification procedure (Radiation protection - Sealed radioactive sources - Leakage test methods).

6.2.1 Transport of radioactive materials

The physical characteristics of the ^{144}Ce $-^{144}$Pr and its encapsulation leads to the classification of the source as a Special form of radioactive material according to the IAEA terminology.

6.2.2 Transport with a B(U) type container

During the transport the ^{144}Ce $-^{144}$Pr source contained in its biological shielding will be inserted and secured in an IAEA approved transport container of type B(U) whose characteristics are being defined. The plan is to use an existing transport container. As mentioned above the limit on radiation level will be satisfied thanks to the important tungsten shielding:
• 2 mSv/h in contact with the packaging (or the vehicle);
• 0.1 mSv/h at two meters from the vehicle.

These limits will be checked at each transit points. Vehicles carrying radioactive materials by definition are in motion; the public exposure times are very short (of the order of a few seconds to minutes) during transport. The workers involved in the handling of the container will receive appropriate training on radiological protection. If a member of the CeLAND collaboration attends to the transportation he/she will be classified in the category B (6 mSv/y) and therefore has no impact on his/her health. The limit related to temperature concerns the external temperature of the transport container and not the temperature of the shielding itself.

The transport container of type B(U) must fulfill several requirements as explained above, but must received an agreement from the safety authorities of the countries involved in the transport. To simplify the explanations, a US built and certified container in United Stated needs to be rectified if the transport goes (or transits) through Japan. For this procedure Russia and Europe have mutual agreements to accept containers certified in one of the countries. Agreements of an existing foreign container in Japan can be a long procedure (several months). The ideal case would be to reuse a container which has been already used to transport radioactive material from Russia to Japan.

Two potential transport containers have been identified :

TN TM − MTR

- Engineered by AREVA; used to transport package for irradiated MTR (Material Test Reactor) and TRIGA (Training, Research, and Isotope production, General Atomics) fuel elements Type B(U)F IAEA 1996

- Criticality Safety Index : CSI : 0

- Certified in Europe, Australia and USA; need a certification in Japan

- External dimensions : H = 2008 mm, D = 2080 mm , weight = 23 400 kg (max. loaded)

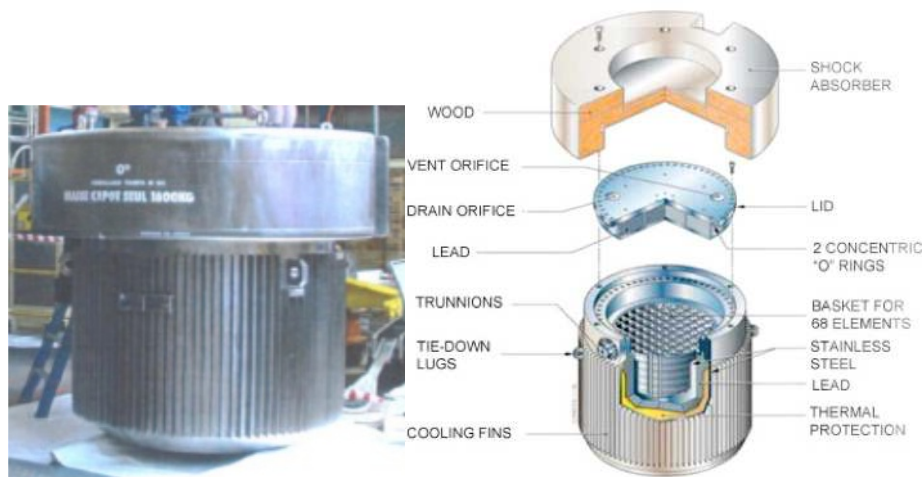- Useful dimensions: Cavity height = 1080 mm; useful cavity diameter = 960 mm

Figure 22: TN TM – MTR transport container.

JMS-87Y-18.5T

- Engineered by Kimura Chemical Plant; used to transport package for irradiated MTR (Material Test Reactor) and TRIGA (Training, Research, and Isotope production, General Atomics) fuel elements

- Certified in Japan and in USA; needs a certification in Russia and possibly a new certification in Japan by the new safety authority (NRA).

- External dimensions : H 1900 mm – D 2000 mm – Weight : 18 500 kg (max. loaded)

- Useful dimensions: Cavity height: 820 mm - cavity diameter: 660 mm
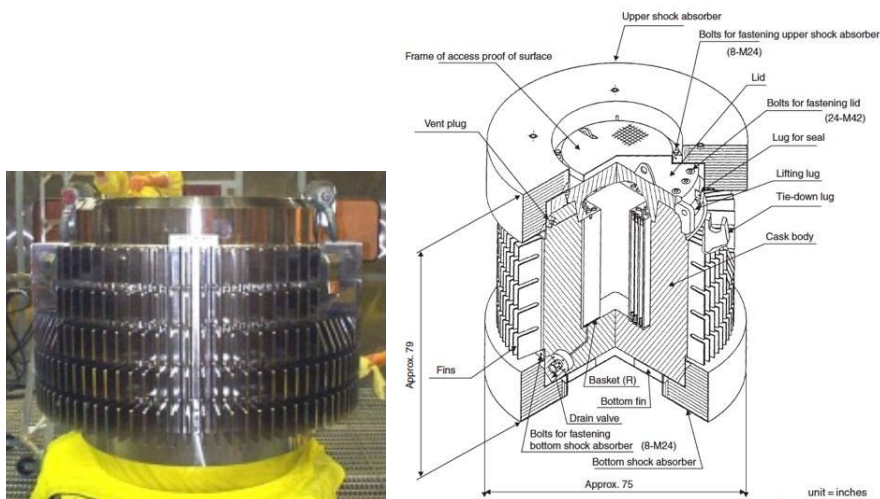
Figure 23: JMS-87Y-18.5T transport container.

The antineutrino generator transportation is being studied with Areva TN International, Hitachi, and PA Mayak that offer a complete range of transport and storage solutions for radioactive materials throughout the entire nuclear fuel cycle. From several meetings with experts we gathered a wealth of useful informations concerning the transport of our radioactive source. There is a very limited number of harbors in the world authorized to receive radioactive materials (so called class

7). Until recently, only the Saint Petersburg and Mourmansk harbors were certified to receive the class 7 radioactive materials in Russia. In particular on the east coast, on the sea of Japan, up to very recently no harbor were approved as class 7. Only Yokohama and Tokyo harbors have the necessary certifications in Japan. Areva TNI transported several shipments of radioactive material towards (and from) Japan, such as fuel elements to be treated at la Hague plant and Plutonium and MoX fuel elements. Similarly they have organized the transport from Mayak to western destinations.
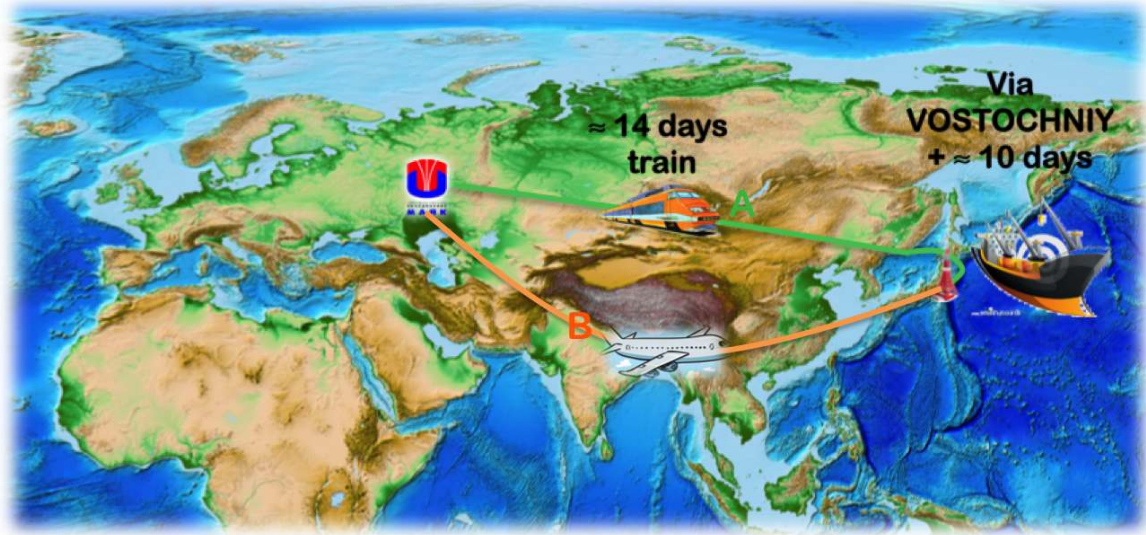
Figure 24: CeLAND transportation routes, via train + boat (A), and airplane (B).

Last fall a transport of enriched uranium took place between Russia and Japan. It transited through the harbor of Nakhodka on the east coast of Siberia. This possibility will reduce the time (and the cost) of the transport by a dedicated ship. IT is shown on 24. Indeed, the boat used for this transport is a fully dedicated boat which means that the cost will include the renting of the boat, the salary of the crew, the renting of the container and, last but not least, the cost of the insurance.

Air transport IAEA regulations allow transport of radioactive material by air, but, in this case there is a limit in the activity of the material inside a single container. For the case of ^{144}Ce the limit is 600 TBq (16.2 kCi), but for ^{51}Cr it is 90 PBq and for ^{60}Co 1200 TBq. Nevertheless the same regulation does not limit the number of container in a single plane, but each radioactive source has to be enclosed in a specific container. Thus we studied the possibility to divide our 75kCi ^{144}Ce source into 5 sources of 15 kCi. Even if the individual activity is reduced, we still need an important shielding to be able to manipulate these sources ; the estimated mass cannot be less than 500 kg. Existing transport containers dedicated for air shipments are used to transport alpha or beta sources with no penetrating radiations. In our case, an extra biological shielding in tungsten is mandatory to be below the radiation limit, but the maximum load for the certification is largely exceeded; therefore they are not suitable for our purpose.

Special arrangements

Having in mind the constraints on transportation following the usual standard IAEA regulations, it is wise to look if the regime of ï¿œ Special arrangements ï¿œ as described in paragraph 310 is more appropriate for our case. It seems useful to quote the text describing this regime:
ï¿œ 310. Consignments for which conformity with the other provisions of these Regulations is impracticable shall not be transported except under special arrangement. Provided the competent authority is satisfied that conformity with the other provisions of these Regulations is impracticable and that the requisite standards of safety established by these Regulations have been demonstrated

through means alternative to the other provisions, the competent authority may approve special arrangement transport operations for single or a planned series of multiple consignments. The overall level of safety in transport shall be at least equivalent to that which would be provided if all the applicable requirements had been met. For consignments of this type, multilateral approval shall be required. ï¿œ

6.2.3 Transport with a C type container

The IAEA and the United States Department of Energy (DOE) fabricated a series of Czech-design SKODa VPVr/M transport overpacks, developed specifically for spent fuel storage and transport inside the standard twenty-foot ISO-containers. Sixteen such SKODa VPVr/M overpacks were produced and subsequently certified first in the Czech republic and then in Russia, where they are now labelled as TUK145/C. This container has now performed spent fuel deliveries by automobile, rail, river and sea transport. Moreover it is the first world's first Type C package certified for the air transport of SNF in compliance with the classification given in IAEA TS-R-1 Regulations, without any restriction on the ANG activity.

TUK-145/C

- Engineered by Skoda in Czech Republic; used to transport package for LEU SNF.

- Certified in Russia for SNF; needs an extension of certification in Russia for containing cerium, only (not considered to be an obstacle) and an extension of the certification in Japan by the new safety authority (NRA).

- External dimensions : H 2155 mm – D 1500 mm – Weight : up to 35 000 kg (max. loaded)

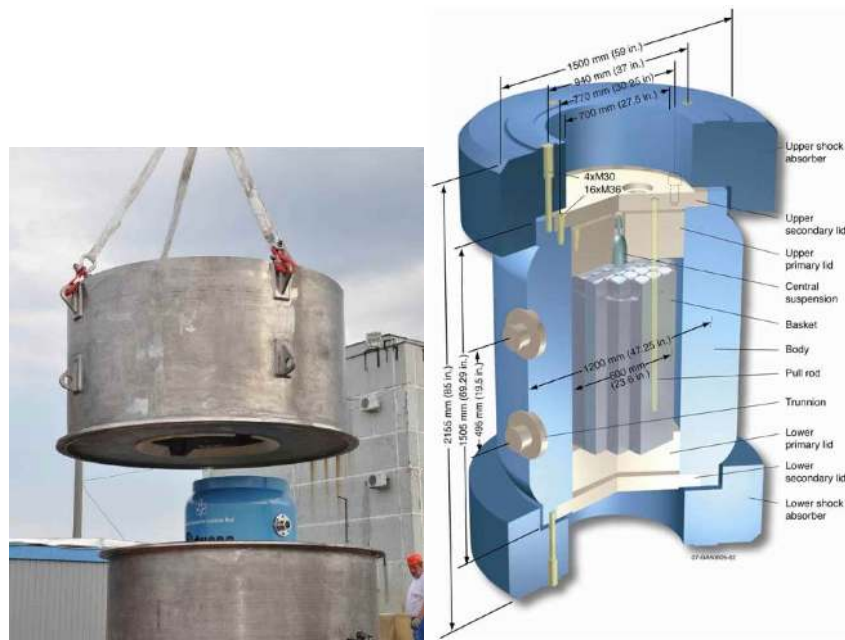- Useful dimensions: Cavity height: 820 mm - cavity diameter: 660 mm

Figure 25: TUK145/C transport container.

The TUK145/C cask is of a unique construction that allows it to be loaded and unloaded from below and from the top. The cask body is made of cast iron. The cask inner walls are plated with aluminum. Leak-tight containment is provided by the metallic Helicoflex seals. The inner cavity of the cask is backfilled with helium. The standard basket would have to be replaced by a

custom basket to fit the cerium antineutrino generator with a reduced shielding not exceeding 450 kg. This corresponds to a thickness of approx. 8.5 cm, leading to a dose rate at 1 m of 10 mSv/h. The basket could be designed by the Sosny Science and Production Firm and fabricated by the OZNO plant in Ozersk, russia.

The TUK145/C container could be used for the transportation of a 75 kCi ^{144}Ce ANG with a reduced, 8.5 cm thick W-alloy shielding. It would be loaded on a truck at PA Mayak, and be transferred to Yekaterinburg airport and loaded into an aircraft (AN-124-100), including the truck that would finally drive from the Japanese airport to the Kamioka mine for unloading. This would necessitate a special operation at the Kamioka site to unload the ^{144}Ce ANG with its reduced shielding from the TUK-145/C and to immediately load it into the additional shielding cylinder, 8 cm thick as well in order to reach the overall 16 cm thickness.

7 Activity measurements

7.1 Requirements

The source activity is a key normalization parameter, directly linked to the prediction of the number of expected events and to the sensitivity of the experiment, particularly at high Δm^2. So the minimal uncertainty on activity is desirable. To ensure the competitiveness of the experiment, a maximum of 2 % uncertainty on activity is considered, 1 % being the goal.

The main technique considered to measure the activity is the calorimetry, which is a global technique relatively easy to interpret and calibrate (compared to radiation measurement). According to nuclear database, the specific activity of the ^{144}Ce $-^{144}$ Pr couple is 7.991 ± 0.044 W/kCi, so a 0.56 % systematic uncertainty will in any case limit the calorimetry sensitivity. In any case, the source would be inside its tungsten biological protection to contain gammas, so the calorimeter must be able to support about 1.5 ton and a cylinder of roughly 60 cm in height and diameter.

Other techniques rely on radiation measurement (β or γ) on a sample of the source, with extrapolation to the source by weighing.

7.2 Calorimetry

7.2.1 Principle

The proposed calorimetric measurement of the source is based on the fact that emitted β, γ , X and Auger radiation will heat up the source and the tungsten shield leading to a well-defined power rate. The temperature increase of the object is described by:

$$\frac{\mathrm{dT}}{\mathrm{dt}} = \frac{\mathrm{P}}{\mathrm{C}} - \frac{\mathrm{T} - \mathrm{T}_{\mathrm{ext}}}{\tau} \tag{24}$$

where T is the temperature at a given time t (in K), P the power released by the source (in W), C the heat capacity (in J.K^{-1}) of the system measured and τ (in s) describes the thermal losses of the calorimeter toward the exterior.

Several different techniques can be used:

- the temperature increase ($\frac{dT}{dt}$) in a calorimeter maximally insulated from the environment can be measured (such as in Gallex [66]), which implies negligible heat losses during the whole measurement and to calibrate the heat capacity;

- the equilibrium temperature (when $\frac{dT}{dt} = 0$) can be measured and compared to a calibration phase;

- the heat can be transferred to another system and then measured, typically to a fluid such as water.

τ can be minimized down to be negligible, and C and τ (if any remaining) can be evaluated precisely in a preliminary calibration phase of the system with known heat sources.

7.2.2 Data

- ^{144}Ce half life: 284.91 days

- ^{144}Pr half life: 17.28 min

- Unitary power: 7.991 ± 0.044 W/kCi

- Density of tungsten alloy: 18.5 g/cm^3

- Heat capacity of tungsten: 130 J/kg

- Thermal conductivity of tungsten: approx. 70 W.m^{-1}.K^{-1}

The thermal power delivered by the source is therefore between 600 and 800 W, for respectively 75 and 100 kCi.

7.2.3 Requirements

1. Uncertainty on thermal power below 1 % (as long as reasonably achievable).

2. Measurement time below 3 days, and preferentially at the hour scale.

3. Capsule temperature below 400°C.

4. Reproducibility of the measurement, which implies a careful and limited instrumentation of the shielding to ensure reproducibility before and after hot cell manipulations and transportation.

7.2.4 Current Design

The current design (see figure 26) relies on the measurement of heat flow transferred to water, by measuring the water massive flow rate and the temperature of the water before and after its circulation at the contact with the shielding. The flow rate can be very precisely measured with Coriolis flow meter, which directly gives the massive flow rate with uncertainty at the 0.1 % level or even better with dedicated calibration. The temperature measurement with thermocouple has an uncertainty of 0.1 to 0.2 K, leading to the requirement for the inflow/outflow water temperature difference of 40 K. This leads to a flow rate of 4 g/s for 85 kCi.
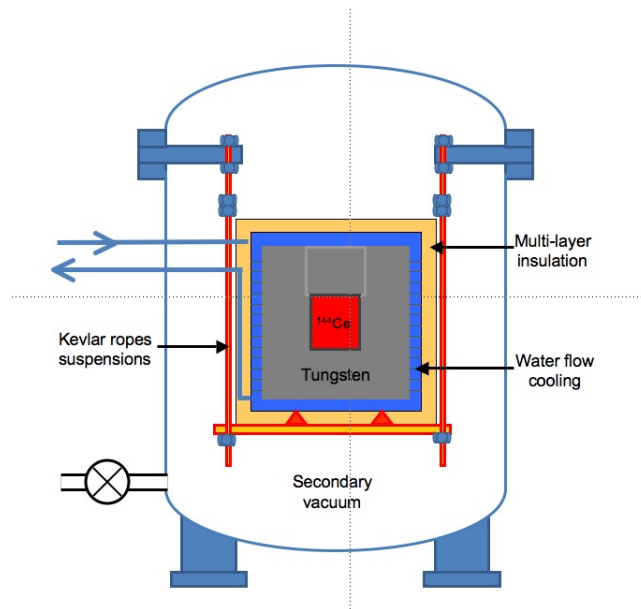

Figure 26: Preliminary design of the calorimeter. The multi-layer radiation shield, which will take place in the vacuum between the two tanks, is missing. The shielded source is supported by 3 pillars, while final design will use 3 strings to hold a board supporting the shielded source. Thermocouples and the Coriolis flow meter are not shown either.

The source power is measured by the power evacuated by water. The source has to be insulated at the watt level to reach 1 % of uncertainty. This can be achieved by a combination of vacuum (probably secondary), suspension of the source (probably with Kevlar strings), multi-layer radiation shield and temperature control of the external tank.

This design ensures reproducibility and allows a preliminary study and calibration phase with electric source power, while being also an absolute measurement since water heat capacity is well known. The time needed for the measurement will probably be dominated by the time needed to reach the target vacuum, since the shielding heating will be low and consequently thermal equilibrium reached in about 1 hour. As soon as both target vacuum and thermal equilibrium are reached, the measurement is over. Finally, the capsule temperature will be far from 400°C since the mean shielding surface temperature will be several tens of degrees Celsius.

7.3 Spectroscopy of samples and weighing of the source

Under the assumption of CeO_2 uniformity (which should be ensured by the mixing of all the cerium solution in a single tank, after chromatography at Mayak), one can sample the CeO_2 and dilute it, determine the activity of the sample by radiation spectroscopy and deduce the source activity by weighing both the source and the sample. Mass measurement can easily achieve excellent accuracy, thus the main source of uncertainty of this technique is the spectroscopy.

β spectroscopy relies on the measurement of the electron spectrum emitted by the sample. This measurement is typically realized with a silicon detector, but the interpretation which relies on simulation (diffusion in sample, back scattering, efficiency...), calibration and background control can be difficult to control at the target level

γ spectroscopy relies on the measurement of a characteristic gamma ray of the ^{144}Ce-^{144}Pr couple, such as the 2.185 MeV ray of the ^{144}Pr which is intense and far from common natural background (above ^{40}K 1.4 MeV ray but still below the ^{208}Tl 2.6 MeV ray). This measurement is typically realized with a High Purity Germanium (HPGe) detector, but the normalization which also relies on simulation (solid angle, auto absorption, efficiency...), calibration and background control can also be difficult to control at the target level.

8 ^{144}Ce $-^{144}$Pr source deployment and data taking

8.1 The KamLAND detector

The KamLAND detector is located under the peak of Ikenoyama (Ike Mountain, 36.42°N, 137.31°E) in the Kamioka mine, see figure 27, with a vertical rock overburden of approximately 2700 meters water equivalent (m.w.e.).

A schematic diagram of KamLAND is shown in figure 28. KamLAND consists of an active detector region of ~1 kton of ultra-pure LS contained in a 13-m-diameter spherical balloon made of 135 μm thick transparent nylon/EVOH (ethylene vinyl alcohol copolymer) composite film and supported by a network of Kevlar ropes. In addition to providing containment for the LS, the balloon protects the LS against the diffusion of ambient radon from the surrounding components. The LS comprises of 80% dodecane, 20% pseudocumene (1,2,4-Trimethylbenzene) by volume, and 1.36 ± 0.03 g/liter of the fluor PPO (2,5-Diphenyloxazole). The density of the LS is 0.780 g/cm^3 at 11.5°C.

A buffer comprising of 57% isoparaffin and 43% dodecane oils by volume fills the region between the balloon and the surrounding 18-m-diameter spherical stainless-steel outer vessel to shield the LS from external radiation.

An array of photomultiplier tubes (PMTs), 1325 specially developed fast PMTs masked to 17-inch diameter and 554 older 20-inch diameter PMTs reused from the Kamiokande experiment are mounted on the inner surface of the outer containment vessel, providing 34% photo-cathode coverage. A 3 mm thick acrylic barrier at 16.6-m-diameter helps prevent radon emanating from the PMT glass from entering the BO. The inner detector (ID), consisting of the LS and BO regions, is surrounded by a 3.2 kton water-Cherenkov detector instrumented with 225 20-inch PMTs. This outer detector (OD) absorbs γ-rays and neutrons from the surrounding rock and enables tagging of cosmic-ray muons.
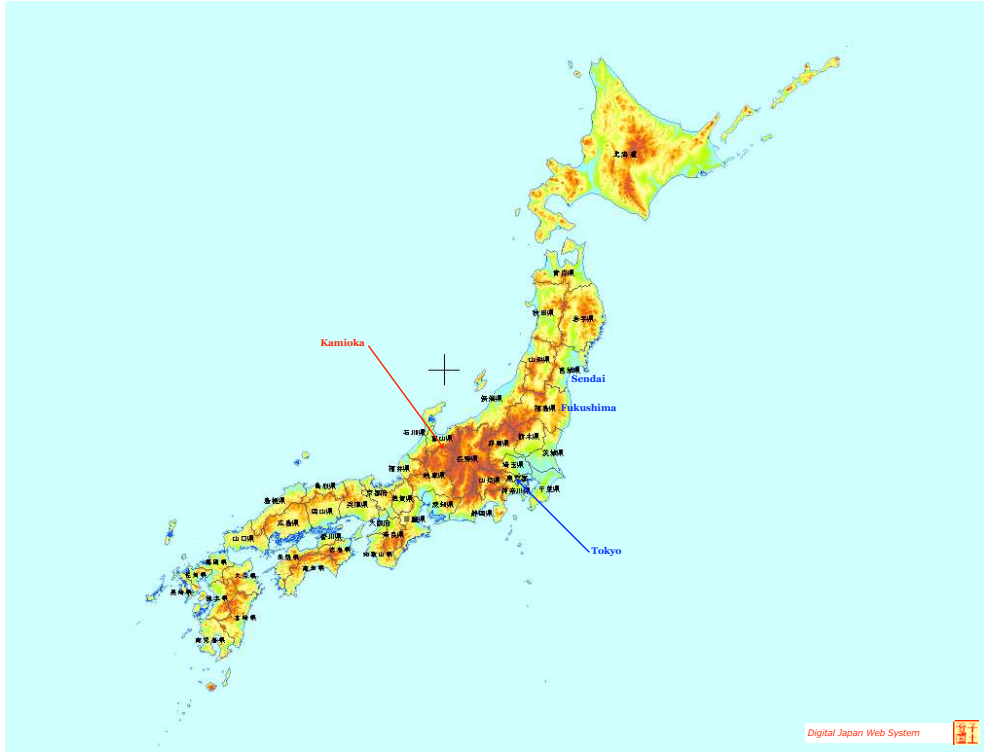
Figure 27: Kamioka mine location.

The KamLAND front-end electronics (FEE) system is based on the Analog Transient Waveform Digitizer (ATWD) which captures PMT signals in 128 10-bit digital samples at intervals of 1.5 ns. Each ATWD captures three gain levels of a PMT signal to obtain a dynamic range from one photoelectron (p.e.) to 1000 p.e. Each ATWD takes $27\,\mu$s to read out, so two are attached to each PMT channel to reduce dead time. The FEE system contains discriminators set at 0.15 p.e. ($\sim$0.3 mV) threshold which send a 125 ns long logic signal to the trigger electronics. The trigger electronics counts the number of ID and OD PMTs above the discriminator threshold with a sampling rate of 40 MHz and initiates readout when the number of 17-inch ID PMTs above the discriminator threshold exceeds the number corresponding to $\sim$0.8 MeV deposited energy. The trigger system also issues independent readout commands when the number of OD PMTs above threshold exceeds a preset number.

The offline analysis takes full advantage of the information stored in the digitized PMT signals by identifying individual PMT pulses in the waveform information that is read out. The time and charge are computed from the individual pulses. For each PMT, the average charge corresponding to a single p.e. is determined from single-pulse waveforms observed in low occupancy events. The ID PMT timing is calibrated with light pulses from a dye laser, injected at the center of the detector through an optical fiber. The vertices of spatially localized low-energy ($<$30 MeV) events are estimated by comparing calculated time-of-flights of optical photons from the hypothetical vertex to the measured arrival times at the PMTs in KamLAND.

The reconstructed energies of events were calibrated with γ sources in past deployments: ^{203}Hg, ^{68}Ge, ^{65}Zn, and ^{60}Co; and with $n + \gamma$ sources: ^{241}Am+^{9}Be and ^{210}Po+^{13}C. These were deployed at various positions along the vertical axis of the detector and occasionally off the vertical axis within 5.5 m from the detector center. The energy calibration is aided with studies of background contaminants ^{40}K and ^{208}Tl, ^{212}Bi-^{212}Po and ^{214}Bi-^{214}Po sequential decays, ^{12}B and ^{12}N spallation products, and γ's from thermal neutron captures on ^{1}H and ^{12}C.

The visible energy (E_{vis}) of an event is computed from the measured light yield. Specifically, E_{vis} is the number of detected p.e. after corrections for PMT variation, dark noise, solid angle, shadowing by suspension ropes, optical transparencies, and scattering properties in the LS. The
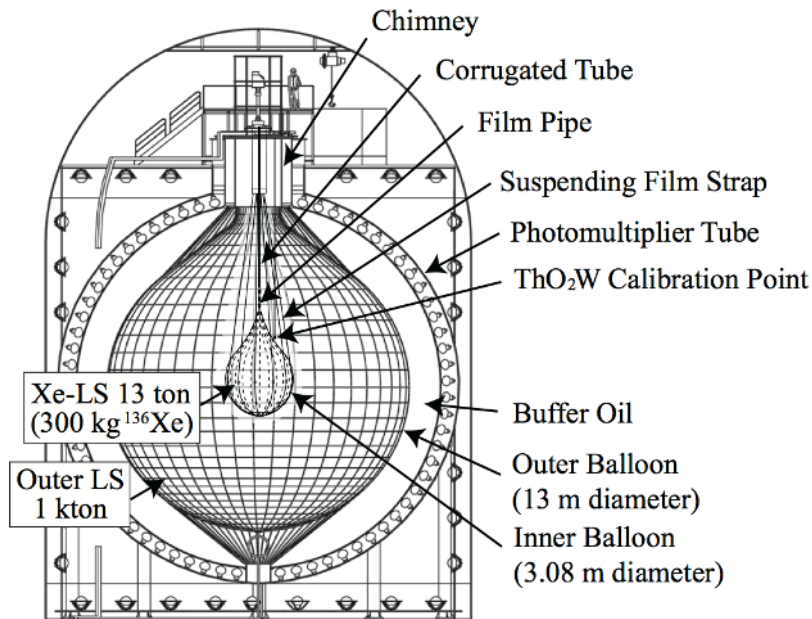
Figure 28: Schematic diagram of the KamLAND detector at the Kamioka underground laboratory, including the KamLAND-Zen balloon.

relationship between E_{vis} and the deposited energy (E_{dep}) of γ's, $e^{\pm}$'s, protons, and α's is non-linear and modeled as a combination of Birks-quenched scintillation and Cherenkov radiation. The scale is adjusted so that E_{vis} is equal to E_{dep} for the 2.225 MeV γ-ray from neutron capture on ^{1}H. The combined 17-inch and 20-inch PMT energy resolution is $\sim 6.5\%/\sqrt{E_{vis}(\mathrm{MeV})}$.

The calibration sources are also used to determine systematic deviations in position reconstruction by comparison with the source's known position. This comparison gives an average position reconstruction uncertainty of less than 3 cm for events with energies in the range 0.28 to 6.1 MeV. The KamLAND experiment started operation in March 2002 and has run continuously since then. The experiment has gone through various phases, the latest phase is a modification to the detector where an additional balloon at the center of the detector is filled with a mixture of liquid scintillator and ^{136}Xe to study neutrinoless double beta decay.

8.1.1 Intrinsic detector backgrounds

A number of backgrounds could mask the oscillation signal from the proposed source measurement. However we demonstrate in what follows that detector background are absolutely not an issue for CeLAND. We perform a simulation including all backgrounds measured or the last 10 years in KamLAND as shown in figure 29. Our background generator takes into account:

- accidental events, usually from natural radioactivity.

- cosmogenics, ^{9}Li and ^{8}He.

- (α,n), an α from Polonium (prompt signal) gets captured by a carbon atom deexciting into oxygen and a neutron (delayed signal from capture).

- geoneutrinos, from U and Th inside Earth's crust and mantle.

- reactor neutrinos, from the surrounding Japanese and Korean nuclear reactors. This background will depend on the nuclear activity in Japan at the time of the experiment, but cannot create significant background contribution even if all reactors in Japan are running at the full power level.
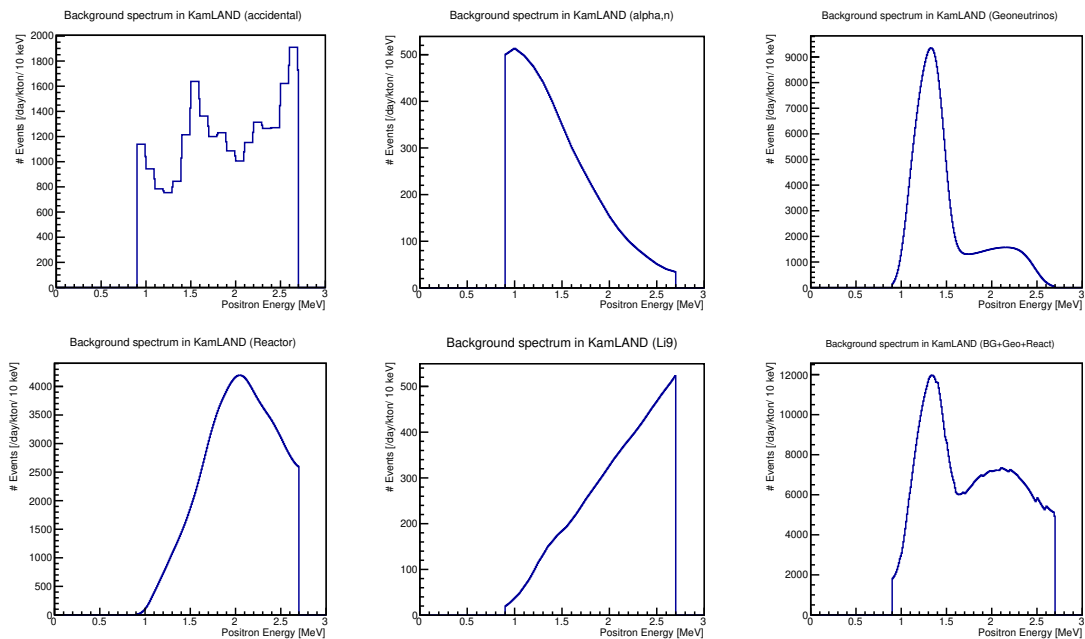
Figure 29: Energy distributions of the KamLAND intrinsic backgrounds measured in-situ. From left to right and top to bottom: accidentals,(α,n), geoneutrinos, reactor neutrinos, ^{9}Li, Sum of all the previous backgrounds.

8.2 KamLAND infrastructure for CeLAND

This section discusses the transportation of the Ce-ANG antineutrino generator in Japan. There are three logical steps to transport the Ce-ANG generator from the port of entry to the KamLAND deployment area:

1. Transportation from a port to the mine entrance;

2. Transportation from the mine entrance to KamLAND entrance;

3. Transportation from the KamLAND entrance to the deployment area.

8.2.1 Transportation of the antineutrino generator to the mine entrance

The Ce-ANG antineutrino generator will arrive at a port on the Pacific Coast (i.e., East-side) of Japan. The generator will be contained in a BU type container with a weight of 10-25 tons. The generator in the BU container will have to be transported from the port to the Kamioka mine entrance.

The national highways are well maintained in Japan and can be used for transportation. A licensed shipping company can transport Ce-ANG in the BU container across the mountains to Kamioka. There are several shipping companies that have transported BU containers in Japan. The CeLAND Japanese group is currently discussing the transportation plan with one such company, HITACHI Transport Systems (HTS). From these discussions it is clear that the technically most challenging segment of the transportation is the last 500 m, just before the Atotsu entrance to the Kamioka mine. The road here follows a narrow path along the Atotsu river and includes a small bridge that may not be able to support the weight of the truck and BU container.

8.2.2 Transportation of the anti neutrino generator to KamLAND entrance

The KamLAND detector is located 2.5 km from the Atotsu entrance of the Kamioka mine, see figure 30. Most of the tunnel from the mine entrance to the detector is horizontal and should not be a problem. However, there is a short, 20 m long section of the tunnel with a slope that will be challenging for transportation.

Figure 30: Access to Kamioka mine entrance from National highway 41.

Once the antineutrino generator arrives at the mine entrance, there are two scenarios:

- The most favorable is the case that the antineutrino generator, contained inside the 1.5-ton γ-ray shield, can be removed from the BU container for further transportation. The mine company has equipment that can lift the 1.5 ton container and transport the container to the KamLAND entrance. This scenario will need detailed discussion with the mine company regarding regulation, in particular whether we will be allowed to lift Ce-ANG at the entrance of the mine without the BU container.

- In case the generator cannot be removed from the BU container, the BU container will have to be transported to the KamLAND entrance on the same truck as was used for transportation from the port. The truck will have to have the capability to clear the slope on the way towards the KamLAND entrance.

8.2.3 Transportation from the KamLAND entrance to the KamLAND dome area

It will not be feasible to transport the generator inside the heavy BU container towards the Kam-LAND dome area. The generator, still inside the 1.5-ton γ-ray shield, will have to be removed from the BU container at this point at the latest. The $25\,\mathrm{m}^3$ tank region, at the entrance of KamLAND-controlled area (see figure 31), can be used to remove the generator and γ-shield from the BU container. We will have to install lifting fixtures in this area to accomplish this. Once Ce-ANG is removed, it can be lifted by existing equipment operated by the Kamioka mine company to the entrance of the KamLAND dome area. The maximum lifting capacity of this equipment is 4 tons and is therefore sufficient for this task.

No heavy machinery can enter the KamLAND dome area. This means that personnel will have to transport the 3-ton shield with the generator over the last ∼15 m. For this we intend to use cranes, chains or other tools.
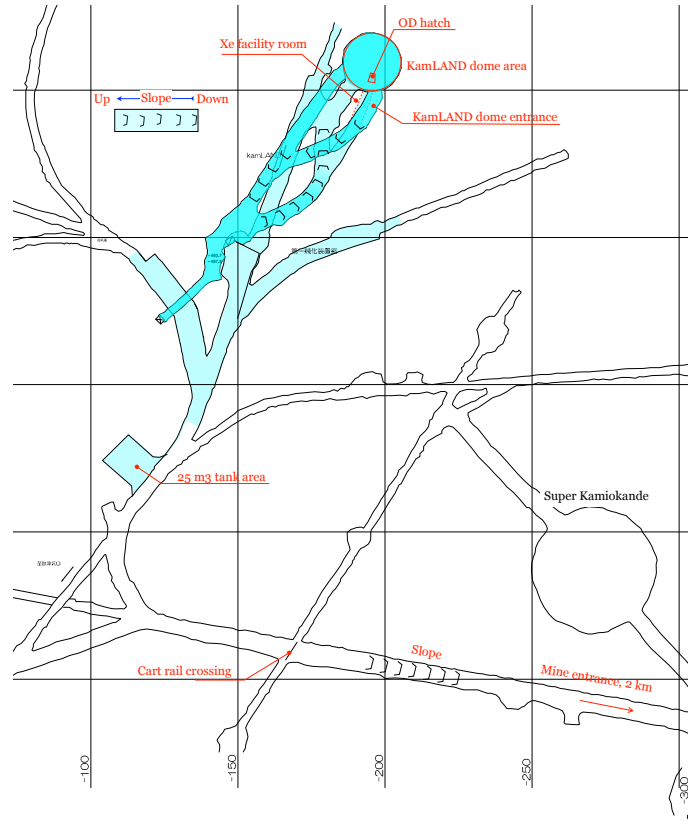
Figure 31: KamLAND area

8.3   Deployment into the outer detector (water veto) and data taking

The existing water Cherenkov detector, the so-called KamLAND OD, provides a straightforward location for the first phase of source deployment.

Source/detector properties	
Source initial activity	75-100 kCi
Source location	Water veto
Source-center distance	9.3 m
Fiducial volume radius	between 6.0 and 6.5 m
Interactions after 6 months	8930
Shielding composition	Tungsten alloy, d=18.5 g/cm^3
Shielding dimensions	51 cm height, 54 cm diameter cylinder - TBC
Shielding mass	1.5 tons

Table 15: CeLAND Phase I deployment data

8.3.1   Detector issues and source deployment

The recirculating water provides a thermal bath for the hot source. Buffer oil provides a free shielding of more than 2.5 m with a density of 0.75. Finally spatial constraints for source location are easier to handle with respect to the detector center. In addition, the placement of the source in the OD avoids complicated issues of cleanliness and W-shielding radiopurity. Nevertheless, a
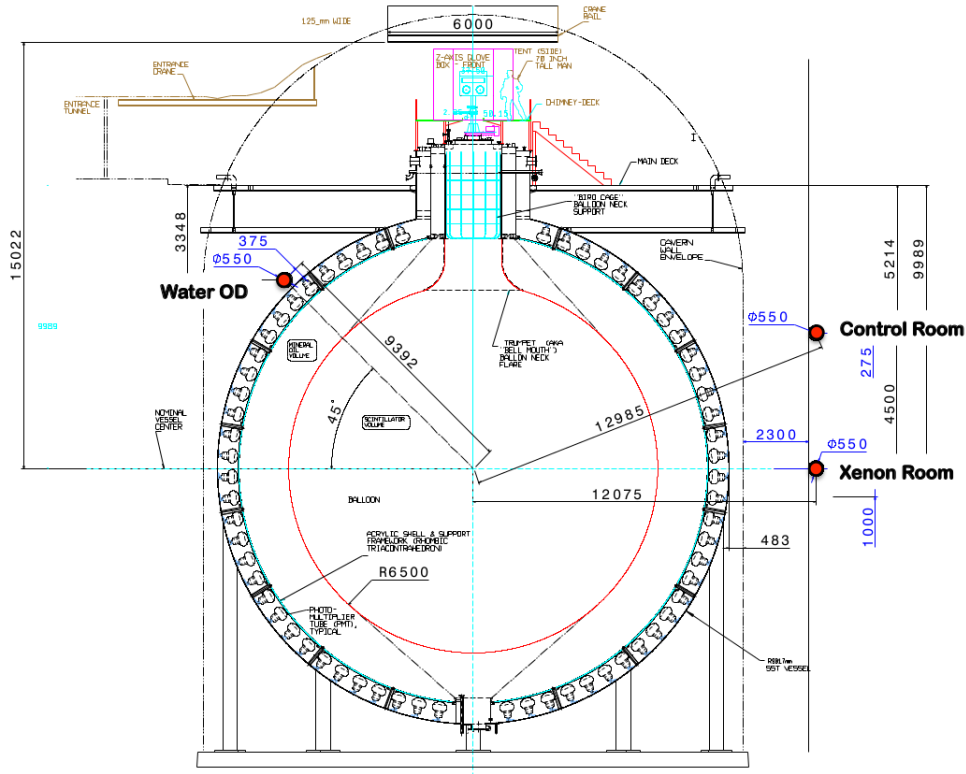
Figure 32: Sketch of the 3 different locations under consideration.

dedicated infrastructure for the transport and lifting of source on the KamLAND detector upper platform has to be designed and realized. In order to prevent the unlikely scenario of a radioactive material contamination in the detector, the source and its biological shielding have to be isolated from the OD. It is thus planned to put it inside a "sock" as sketched in figure 33. This sock, most likely made of stainless steel, will act as an additional shielding for the source intrinsic γ's and will be filled with water or any other liquid that will act as a temperature and neutron flux moderator.

8.3.2 Signal and backgrounds

Assuming a moderator thickness of 10 cm, the source will be located at about 9.3 m from the detector center, separated from the active liquid scintillator volume by at least 2.8 m. CeLAND data are given in Table 15. In the case of no-oscillation we estimate that 14650 neutrino events in one year are expected within the detector fiducial volume (taken as R<6.5 m inside the balloon containing the liquid scintillator). The expected number of interactions is given in Table 15.

The energy and distance traveled determine the oscillation probability of the $\overline{\nu}_e$ flux. Using the GEANT4 KamLAND Monte-Carlo simulation we simulated 10 million events. However results that follows are renormalized to 20000 to match the expectation for a one year run with a 75 kCi source located 9.3 m away from the detector center.

Figure 35 and shows the effect of $\overline{\nu}_e \rightarrow \nu_s$ oscillation as a function of energy and distance from the source. It is displayed as a function of R/E in figure 39. It also illustrates the fractional oscillation effect normalized to the expected, unoscillated event rate. In what follows, to be conservative, signal is being considered within a radius of 6 m with respect to the detector center to limit the
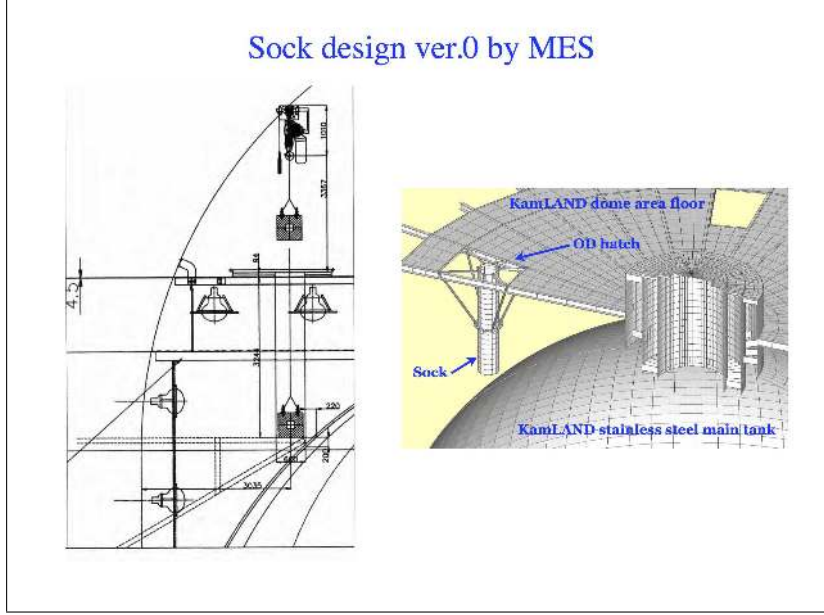
Figure 33: Ce-ANG is contained inside a stainless steel enclosure ("sock") and suspended into the Outer Detector.

contribution of the accidental background. This fiducial cut could probably be relaxed to use the whole liquid scintillator contained in the balloon. As an illustration we considered, as a baseline, the following neutrino oscillation parameters: $\Delta m_{14}^2 = 2\,\mathrm{eV}^2$, $\sin^2(2\,\theta_{14}) = 0.1$.

Months	3	6	9	12	18	24	30	36	48
R<6 m	4950	8930	12110	14650	18330	20710	22170	23160	24180
R<6.5 m	6425	11560	15680	18970	23740	26800	28710	29970	31330

Table 16: Expected $\overline{\nu}_e$ interactions inside KamLAND with a 75 kCi ^{144}Ce antineutrino generator at 9.3 m from the detector center as a function of the exposure for 2 definitions of the fiducial volume, R<6 m (current KamLAND analysis) and R<6.5 m (extension of the fiducial volume to the KamLAND balloon surface).

8.3.3   Expected sensitivity

This section illustrate the expected sensitivity of the CeLAND experiment for an antineutrino generator deployed at 9.3 m from the target detector center.

8.4   Alternative deployment into the Xenon Room and data taking

Given the technical issues raised by a deployment in the OD, another option has been studied: the possibility of placing the source outside the detector volume. Two locations are being considered: the Xenon room and the Control room as shown infigure 32. We will focus on the Xenon room which is currently being used to store and purify the Xenon used for the KamLAND-Zen experiment.
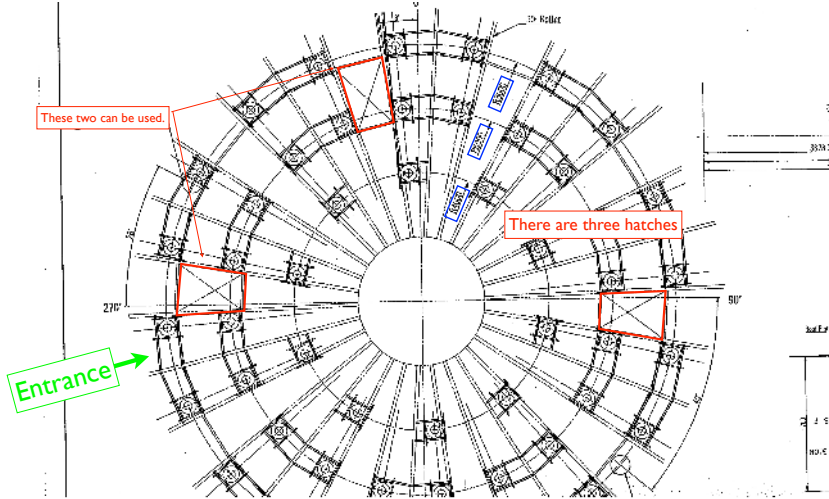
Figure 34: KamLAND top platform and OD hatch to be used for the source insertion inside the OD.
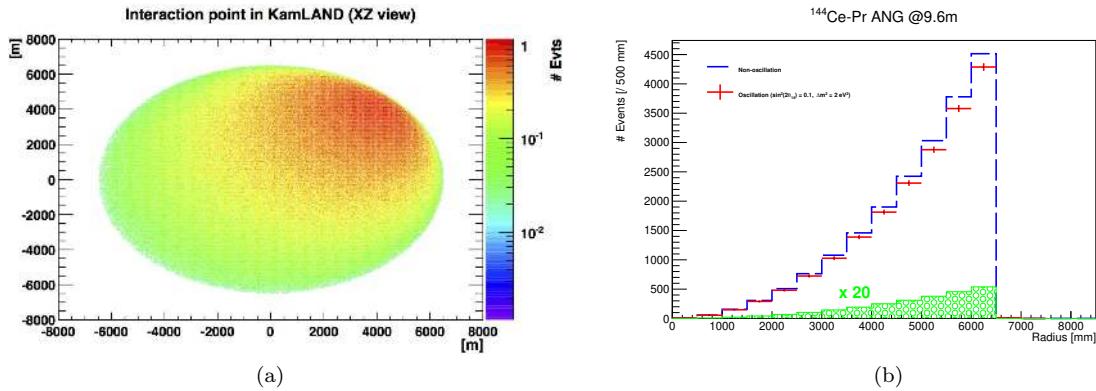

(a)   (b)

Figure 35: Left panel: Simulation of signal events in the non-oscillation case, for a source located at $Y \sim 6.8\,\mathrm{m}$ and $Z \sim 6.8\,\mathrm{m}$ (here, 9.3 m away from the detector center). Right panel: Radial distribution of the signal (blue without oscillation, red with oscillation) and background events (green). Backgrounds are enhanced by a factor 20 to be visible on the plot. The origin of the radius is taken at the center of the detector.

8.4.1 Detector issues and source deployment

An alternative option for the deployment of Ce-ANG is the xenon facility room (Xe-LS room) that is used for the KamLAND-Zen phase of the experiment. There are significant challenges here as the area is completely filled with equipment to process the xenon and load it into the liquid scintillator. In this case, Ce-ANG would have to be lifted through a narrow corridor (600 mm width) to the back of the area, see figure 43. An additional 80 mm of tungsten shielding would be necessary to allow people to occupy the area without making it into a controlled radiation area.

The most optimal spots in the Xenon room and the Control room are respectively located 12 m and 13 m from the detector center. Given the relative easiness of integration in both cases, the shorter baseline of the Xenon room is advantageous. In addition we are considering the option of performing the calorimetric activity measurement in the Xenon room as well; this would allow start of the data taking while the source is still in the calorimeter, therefore increasing the number of detected neutrinos.
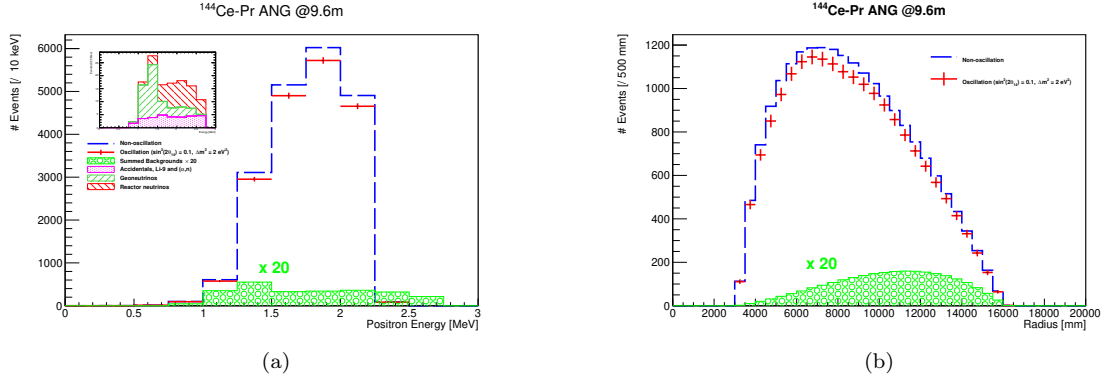
Figure 36: Left panel: Energy distribution of the signal in case of non-oscillation (blue) and oscillation (red) and the background (green, enhanced by a factor 20). Various background components are stacked in the inset. Right panel: Radial distribution of the signal and background with the same color codes. Only the sum of all backgrounds is represented, dominated by the geoneutrinos. The origin of the radius is taken at the center of the source, 9.3 m away from the detector center.
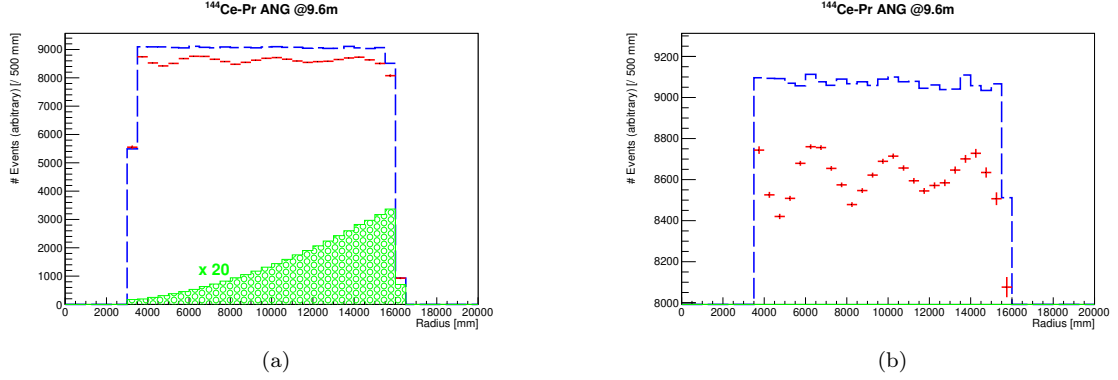

Figure 37: Left panel: normalized radial distribution of the signal and background in case of non-oscillation (blue) and oscillation (red) and the background (green, enhanced by a factor 20). Each bin content at equidistance to the source is divided by the total scintillator volume at the corresponding distance. Right panel: zoom on the radial normalized distributions. Oscillation parameters are $\Delta m_{14}^2 = 2\,\text{eV}^2$, $\sin^2(2\,\theta_{14}) = 0.1$ in the 3 active + 1 sterile neutrino hypothesis.

8.4.2 Signal and backgrounds and sensitivity

Even though the signal quality is lowered by the increase of baseline at these two locations, it would allow CeLAND to basically become a background-free experiment. Indeed, at 12 m, the gamma and neutron activities of the source are no longer an issue. Besides, if needed, it is much easier to put additional shielding in the Xenon room than in the OD. The sensitivity is shown in figure 44.

8.5 Running in parallel with KamLAND-Zen

The KamLAND-Zen experiment, dedicated to the search of the rare neutrinoless double beta decay process ($0\nu2\beta$) with ^{136}Xe, has been installed in the center of the KamLAND LS balloon in 2011[71]. It consists of a 3.08 m nylon-based transparent balloon (IB) filled with 13 tons of Xe-loaded liquid scintillator as shown in figure 28.
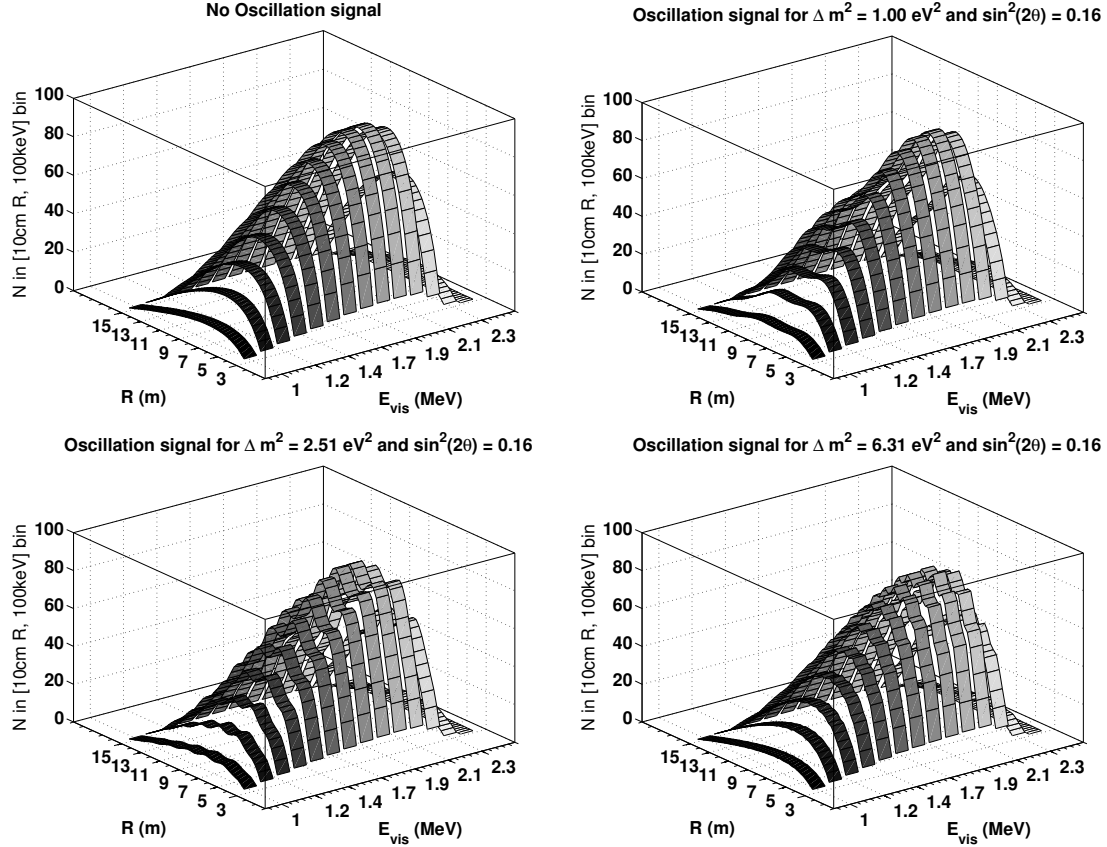
Figure 38: Advantage of $\bar{\nu}_e$ sources providing both R and E$_{vis}$ oscillation patterns. IBD rate for a 75 kCi ^{144}Ce source deployed in the OD of KamLAND, in 10 cm radius bins and 100 keV bins of visible energy, E$_{vis}$=E$_e$+2m$_e$. In 1.5 year, 20,000 $\bar{\nu}_e$ interact within the detector (with a fiducial volume define as R<6m), for the no-oscillation scenario (top-left panel). The other panels show the expected oscillation signal for $\Delta m^2_{\mathrm{new}}$=1, 2.5, 6.3 eV^2 and $\sin^2(2\theta_{\mathrm{new}})$=0.16.

A double beta decay process consists of the simultaneous emission of two electrons with ($2\nu2\beta$) or without ($0\nu2\beta$) neutrino emission. In the case of ^{136}Xe, the $2\nu2\beta$ energy spectrum consists of a continuum up to the nucleus Q-value of 2.458 MeV while the $0\nu2\beta$ spectrum should be a Dirac delta distribution at this Q-value. Taking into account the KamLAND energy resolution of $6.6\%/\sqrt{E(MeV)}$ leads to an overlap of this $0\nu2\beta$ signal with the neutron capture signal at 2.2 MeV and the signals from several radioactive isotopes such as the ^{214}Bi from natural Uranium. These backgrounds have been thoroughly studied by the KamLAND-Zen collaboration and, in order to suppress the antineutrino background from both prompt and delayed events of the IBD process, a 1 ms coincidence cut is applied to the KamLAND-Zen data[72]. Furthermore, by loosing the time and space criteria we will achieve a ˜99.97% rejection efficiency, similar to ^{214}Bi-Po. The remaining number of 2.2 MeV γ capture will be then much lower than any other in-situ backgrounds, at the level of a few events per year.

The CeLAND experiment will not be an additional source of background for the already installed KamLAND-Zen experiment. However, the background of Zen for CeLAND might be worth looking at.

The energy window of interest for $0\nu2\beta$ in ^{136}Xe is located between 2.2 and 3.0 MeV which is the end-point of the ^{144}Pr antineutrino prompt spectrum (figure 45). Besides, with a 90 % CL upper limit of 0.034 evts.ton^{-1}.day^{-1}, the $0\nu2\beta$ background is be considered negligible for both prompt and delayed events.

However with an event rate of 80.2 $\pm$ 1.8(stat) $\pm$ 3.4(syst) evts.ton^{-1}.day^{-1} and its continuous spectrum up to the ^{136}Xe Q-value, the $2\nu2\beta$ could be considered a non-negligible background for the detector central region. In the case of CeLAND, this region is located at the center of the layer
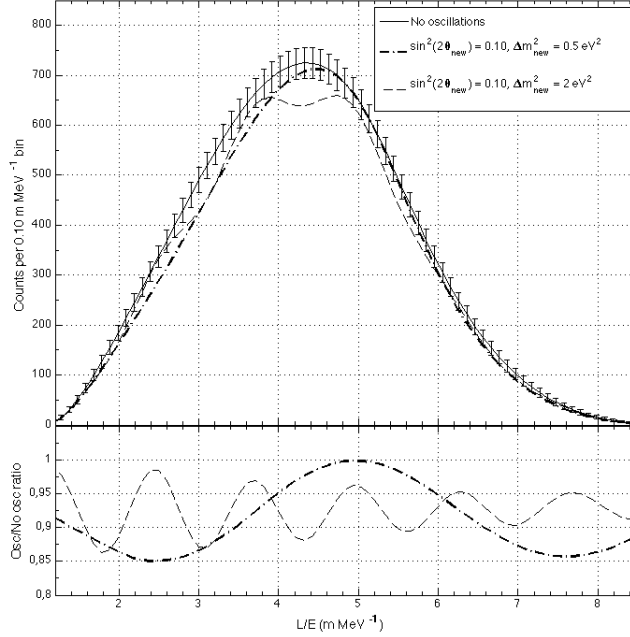
Figure 39: Signal displayed as a function of the variable R/E (L/E on the plot). Statistical error bars are included assuming 18 months of data taking and a fiducial volume defined by R<6.5 m. The shape uncertainty on the current knowledge of the praseodymium neutrino spectra is included, as well as an 1.5% uncertainty on the source activity. Two oscillation scenarios are given, for Δm^2_{new}=0.5 and 2.0 eV^2 and $\sin^2(2\theta_{new})$=0.1, and compared with the no-oscillation case.

Months	3	6	9	12	18	24	30	36	48
R<6 m	3060	5520	7480	9050	11320	12770	13710	14300	14940
R<6.5 m	3930	7080	9610	11630	14530	16410	17620	18380	19190

Table 17: CeLAND in Xenon room: Expected $\bar{\nu}_e$ interactions inside KamLAND with a 75 kCi ^{144}Ce antineutrino generator at 12 m from the detector center as a function of the exposure for 2 definitions of the fiducial volume, R<6 m (current KamLAND analysis) and R<6.5 m (extension of the fiducial volume to the KamLAND balloon surface).

[7.76 ; 10.84] m from the source and contains about 30 % of the events (6700 events for an overall number of 20000 events). A quick computation using the $2\nu2\beta$ event rate and the KamLAND IBD time window of 620 µs gives a total number of coincidences induced by the double beta signal of 2.57×10^{-3} for a data taking period of 1.5 year. Even though the $2\nu2\beta$ event rate can be considered negligible, an additional spatial cut is still needed around the KamLAND-Zen mini-balloon and especially its piping line since it induces a high background rate due to natural radioactivity. This spatial cut only affects the delayed IBD events with the following: $R_d > 2.5$m and $\rho_d > 2.5$m, $Z_d > 0$m (vertical central cylinder cut at the upper hemisphere)[80].
In conclusion KamLAND-Zen is a negligible source of background for CeLAND as well and both experiments can run simultaneously during CeLAND run.

8.6 Additional systematic studies

In this section we evaluate the impact on the experimental sensitivity of: the finite extension of the CeANG, the effect of the finite energy and vertex resolutions, and the knowledge of the source activity. We found out that only only the latter could significantly affect the experiment.

8.6.1 Finite source size effect

Since the cerium material will be contained in a cylinder the $\bar{\nu}_e$ emission cannot be exactly taken as a point like source. We evaluated the impact of the slight extension of the source through
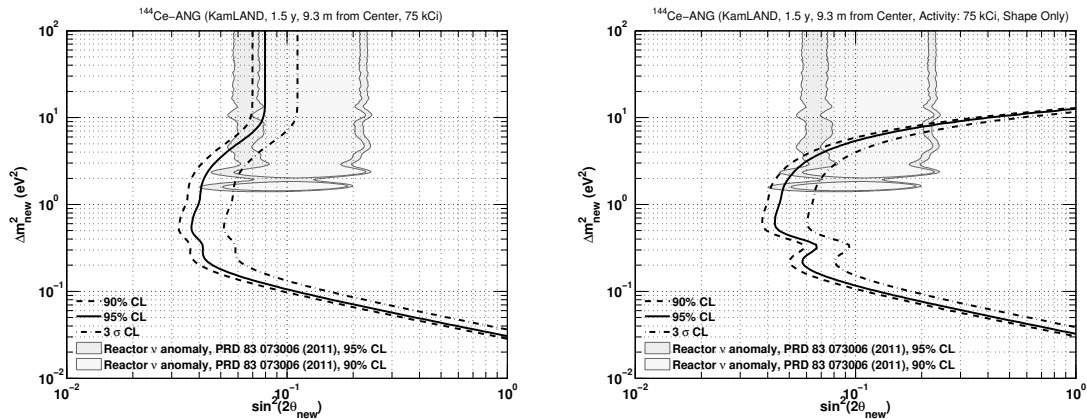
Figure 40: Expected sensitivity to exclude the non-oscillation. We assume an initial activity of 75 kCi with a source 9.3 m from the center. The fiducial volume is starting from the detector center and extends to a radius of 6.5 m. Results are given for 1.5 year of data taking for a rate+shape analysis (left panel), and for a shape only analysis (right panel). The normalization uncertainty is taken at 1.5%.
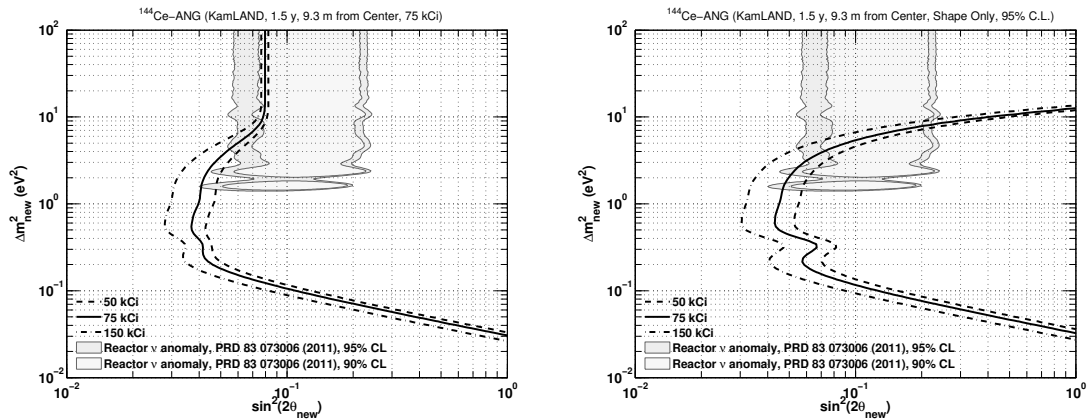

Figure 41: 95% C.L. expected sensitivity to exclude the non-oscillation, as a function of the activity of the source. We assume the antineutrino generator to be places at 9.3 m from the detector center. The fiducial volume is starting from the detector center and extends to a radius of 6.5 m. Results are given for 1.5 year of data taking for a rate+shape analysis (left panel), and for a shape only analysis (right panel). The normalization uncertainty is taken at 1.5%.

Monte-Carlo simulations and found out that a 15 cm-scale CeANG provides a sensitivity as good as the point like source case (that will indeed be used for all other computations). Results are displayed in figure 46.

8.6.2   Energy resolution

CeLAND sensitivity may depend on the energy resolution of the KamLAND detector. As stated previously in this proposal, the energy resolution of KamLAND detector is $6.5\%/(E\_vis\ (MeV))^{0.5}$. The impact on CeLAND sensitivity was evaluated for a 18 months long run and the CeANG located 9.3 m away from the detector center. The energy resolution was varied from 2.5% to 15% as a flat value independent of energy. The results are shown in figure 47. The sensitivity is only marginally degraded for Δm^2 between 1 to 10 eV^2. Since KamLAND published energy resolution ranges from 4.4 % to 6.5 % at 1 MeV visible energy, corresponding conservatively to the black lines on all plots since the positrons induced from the source have an energy between 1 and 2.3 MeV. The energy resolution is therefore not an issue for the CeLAND. Exclusion contours are given at the 95% CL for a fiducial volume taken as 0<R<6.5 m. Improvement of the energy resolution would, slightly

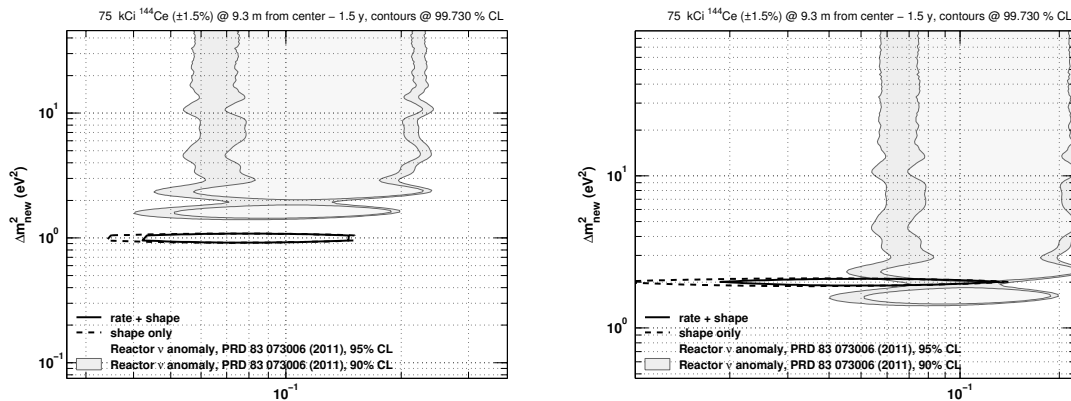Figure 42: 3σ discovery potential illustrated for two examples: $\Delta m_{14}^2 = 1\,\mathrm{eV}^2, \sin^2(2\,\theta_{14}) = 0.1$ (left) and $\Delta m_{14}^2 = 2\,\mathrm{eV}^2, \sin^2(2\,\theta_{14}) = 0.075$ (right) . We assume the antineutrino generator to be places at 9.3 m from the detector center. The fiducial volume is starting from the detector center and extends to a radius of 6.5 m. Results are given for 1.5 year of data taking. The normalization uncertainty is taken at 1.5%.

Months	3	6	9	12	18	24	30	36	48
R<6 m	2580	4660	6320	7640	9560	10780	11560	12080	12630
R<6.5 m	3320	5980	8100	9800	12250	13830	14850	15500	16180

Table 18: CeLAND in Control room: Expected $\overline{\nu}_e$ interactions inside KamLAND with a 75 kCi ^{144}Ce antineutrino generator at 13 m from the detector center as a function of the exposure for 2 definitions of the fiducial volume, R<6 m (current KamLAND analysis) and R<6.5 m (extension of the fiducial volume to the second nylon vessel).

enhance the sensitivity of the shape only analysis for $\Delta m^2 > 2$ eV^2.

8.6.3 Vertex resolution

KamLAND's vertex resolution may impact sensitivity of CeLAND and a simulation study was conducted to evaluate it. In this study, the CeANG was located 9.3 m from the detector center for the duration of 6 and 18 months. The vertex resolution was varied from 10 to 25 cm. The results are shown in figure 48. The sensitivity is marginally degraded for Δm^2 between 1 to 10 eV2. KamLAND's vertex resolution of 12 cm$/(E\_\mathrm{vis}[\mathrm{MeV}])^{0.5}$, or 8 cm to 12 cm in the CeLAND energy range of interest, corresponds approximately to the black lines on all plots, and it is not expected to be an issue, though reconstruction will have to be calibrated in the outermost region of the target volume. In any case one expects no concern induced by vertex resolution effect for the experiment. Exclusion contours are given at the 95% CL for a fiducial volume is taken as 0<R<6.5 m.

8.6.4 Uncertainty on the source activity

Uncertainty in the knowledge of the CeANG activity directly impacts CeLAND's rate measurement and more significantly the sensitivity at delta Δm^2 above a couple of eV^2. The simulation study was conducted to assess the sensitivity of CeLAND to the systematic uncertainty in the rate of the CeANG. The CeANG's activity uncertainty was varied in the range from 0.5% to 3%. The results are shown in figure 49. As can be seen in the plot, the impact of the absolute rate uncertainty is significant especially for smaller values of mixing angle and higher values of Δm^2. The measurement of the absolute activity of the source will be performed prior to deployment in the dedicated calorimeter described earlier. Another measurement will be performed at the end of the deployment run. The plan is to measure the CeANG activity with 1.5% precision or better.
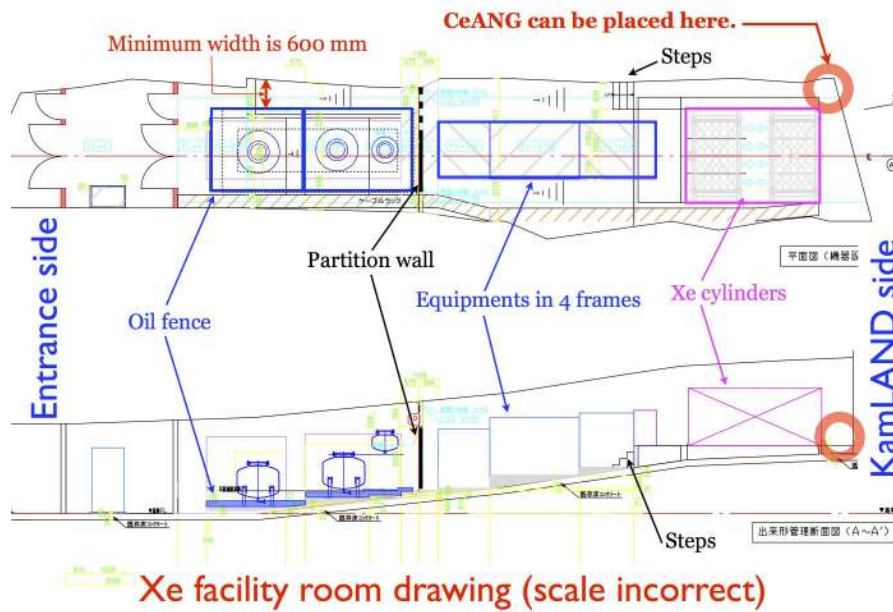
Figure 43: Xe-LS facility room, an alternative deployment area for Ce-ANG.

9 ^{144}Ce $-^{144}$Pr source disposal

At the end of the experiment, the source activity will have decreased by a factor of 6 or so. However, all radio-protection safety rules will still apply for the removal of the source from the detector.
The source disposal will be facilitated by the radioactive decay of cerium. We provide below the evolution of the state of the cerium ANG with time elapsed since its production (see also table 19):

- at the end of the experiment, 2 years after the source delivery (at 85 kCi), the source will only deliver 100 W at 15 kCi;

- after 5 years, heat power will reach the watt scale (for 1 kCi) where heat issues can be neglected, and dose rate at 1 m of the shielded source will be of the order of the natural dose rate (some 0.1 µSv/h, depending on the site);

- after 20 years, the source will reach the 10 MBq scale (corresponding to some 100 kBq in γ activity) where manipulation with bare hand is conceivable and the dose rate at 1 m of the naked source will be of the order of the natural dose rate ;

- after 25 years, the source will reach about 100 Bq/kg, which correspond to natural activity of standard matter;

- after 40 years, the source would reach the Bq scale, but long-lived impurities will probably limit the decrease in the activity.

For disposal the antineutrino generator will return to PA Mayak in Russia. The transport cost could be reduced by keeping the source in Japan (Kamioka mine) until its activity is less than 16 kCi (approx. 2 years after production) such as a regular type B(U) container could be used for air transportation without special arrangement. This should implicitly happen after the data taking period and further measurement of the source activity.
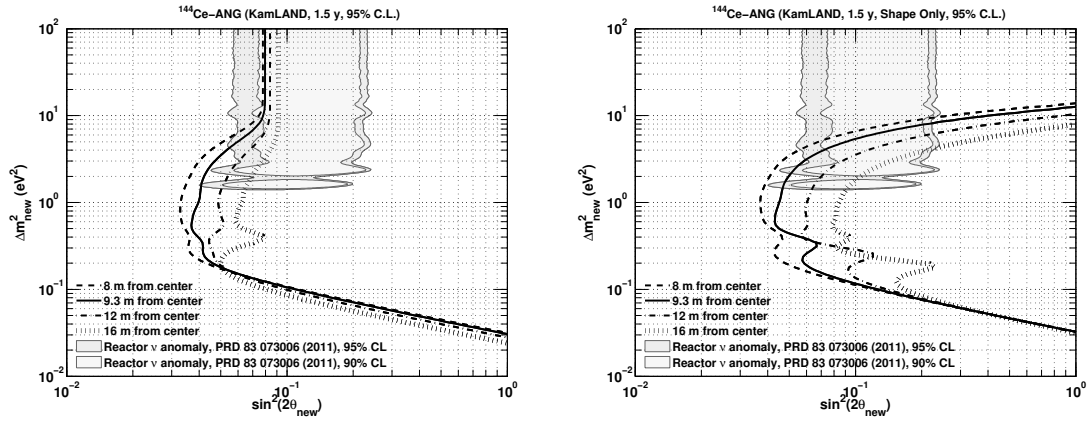
Figure 44: Sensitivity to exclude non-oscillation with a 75 kCi antineutrino generator as a function of the distance between the emitter and the detector center. The xenon/control room sites are located 12 m and 13 m away, respectively. The left panel shows the rate+shape sensitivity assuming a normalization uncertainty of 1.5%, whereas the right panel shows the shape only sensitivity, which is more affected by a longer baseline. Exclusion contours are given at the 95% CL for a fiducial volume is taken as 0<R<6.5 m.
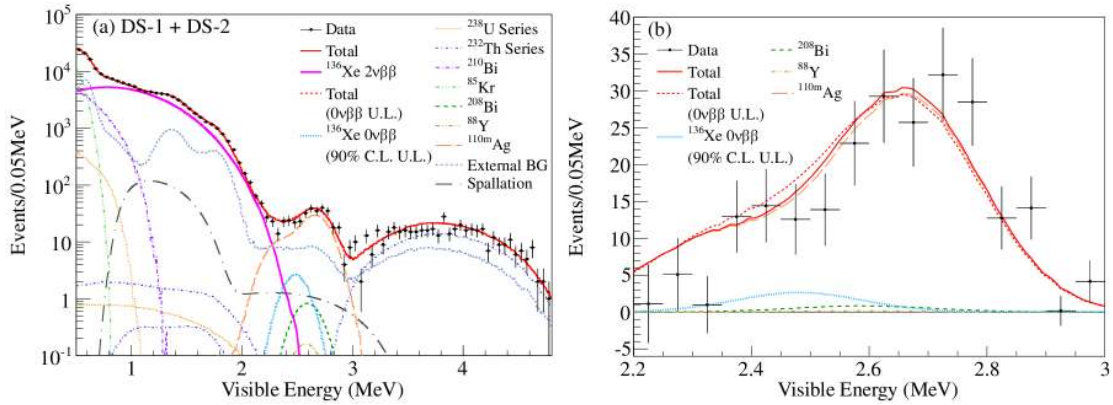

Figure 45: (a) Energy spectrum of the KamLAND-Zen candidate events with the best-fit backgrounds, $2\nu2\beta$ decays and 90 % CL upper limit on $0\nu2\beta$ decays on the $0.5 < E < 4.8$ MeV range. (b) Close-up on the energy window of interest for $0\nu2\beta$ after known-background subtraction.

10   Conclusion

The CeLAND experiment offers to deploy a 75 kCi ^{144}Ce $-^{144}$Pr antineutrino generator next or inside the KamLAND detector in order to test both the reactor and the gallium anomalies. The concept of the experiment is to measure the energy and position dependence of the detected neutrino flux, characteristic of neutrino oscillation into a 4th state. Consequently this will allow to search for eV-scale light sterile neutrino oscillations with mass splittings of ≥0.1 eV^2 and $\sin^2(2\theta_{new}) > 0.05$. With 1.5 year of data, the anomalous allowed region of mixing parameters could be probed non ambiguously. CeLAND plans to make use of the existing KamLAND detector with well-measured backgrounds and systematics. Beside upgrading the KamLAND installation to safely host the source, most of the new effort involves creating, for the first time, an 75 kCi ^{144}Ce $-^{144}$Pr antineutrino and delivering it to the detector, where it could be placed in a first phase outside the detector, 9.3 m from the center (this phase is the main purpose of our current proposal), and possibly later inside the target liquid scintillator, but only after the KamLAND-Zen $0\nu\beta\beta$ run is complete and if a hint of oscillation would be discovered during the first phase. The cost-scale of the whole experiment is estimated to be less than 5 M\$, and data taking could start within the next 1.5 years, depending of funding and logistic issues being currently investigated.
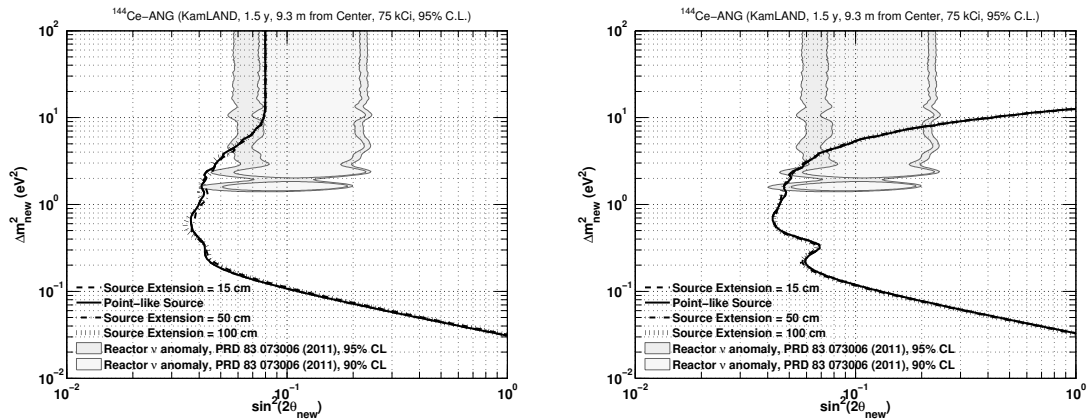
Figure 46: Impact of the extension of the source on the sensitivity. The source extension is taken as a sphere ranging from 0 to of 100 cm diameter. We observe that the sensitivity is not degraded at all by extensions of the source up to 100 cm, for a rate+shape analysis (left) and a shape only analysis (right). Exclusion contours are given at the 95% CL for 1.5 y of data taking with a source located 9.3 m away from the detector center. The vertex resolution of the detector is taken as 15 cm. Fiducial volume is taken as 0<R<6.5 m.

Source age	Heat (W)	β activity	2.2 MeV γ activity	Dose rate with shielding (µSv/h)	Dose rate without shielding (µSv/h)
1 day	678	84.8 kCi	594 Ci	16.4	6.6×10^6
1 week	668	83.6 kCi	585 Ci	16.1	6.5×10^6
1 month	631	79.0 kCi	553 Ci	15.3	6.2×10^6
3 month	546	68.3 kCi	478 Ci	13.2	5.3×10^6
$1/2$ year	438	54.9 kCi	384 Ci	10.6	4.3×10^6
1 year	279	35.0 kCi	245 Ci	6.8	2.7×10^6
2 years	115	14.4 kCi	101 Ci	2.8	1.1×10^6
3 years	47.3	5.92 kCi	41 Ci	1.1	4.6×10^5
5 years	8.0	1.00 kCi	7.0 Ci	0.19	7.8×10^4
10 years	9.5×10^{-2}	12 Ci	3.1 GBq	2.3×10^{-3}	9.2×10^2
20 years	1.3×10^{-5}	61 MBq	430 kBq	3.2×10^{-7}	0.13
40 years	2.5×10^{-13}	1.2 Bq	8.3 mBq	6.2×10^{-15}	2.5×10^{-9}

Table 19: Evolution of the source, starting with an initial β activity of 85 kCi. The dose rate is calculated with formula 23 at 1 m from the center of the source (~ 80 cm of the shielding if any).

A   Interaction length in Tungsten alloy

In reference [63] we found plots of the cross section for photon on all elements taking from the evaluated data base ENDF/B-VI. Examples on W, Fe, Ni,U are given in figure 50. These data are used to precisely compute the interaction length in tungsten alloys.

The total interaction length is 1.238 $\pm$ 0.14 cm (see details in table 20). For comparison, the interaction lengths in pure tungsten and uranium metals are respectively 1.19 cm and 1.13 cm. For a tungsten alloy shielding having a density of 18.5 $\pm$ 0.2 gm/cm^{3}the attenuation factor in a 35 cm thick shielding is $(5.25 \pm 1.4\ ) \times 10^{-13}$.
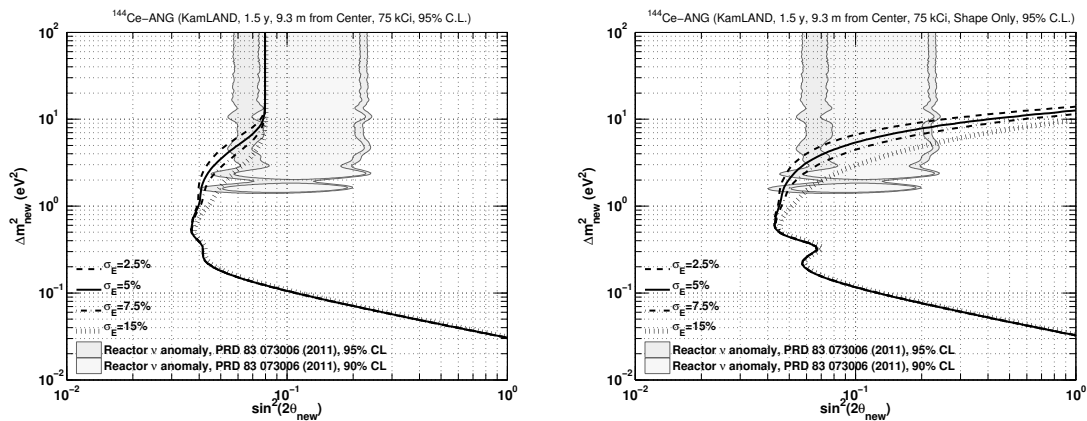
Figure 47: Impact of the KamLAND energy resolution on the sensitivity. We assume a antineutrino generator located 9.3 m away from the detector center. The sensitivity is computed for 18 months of data taking. We vary the resolution from 2.5% to 15%, not depending on energy. The left panel shows the rate+shape sensitivity assuming a normalization uncertainty of 1.5%, whereas the right panel shows the shape only sensitivity. We observe that the sensitivity is not noticeably degraded for Δm^2 between 1 to 10 eV^2 in the case of the rate+shape analysis. KamLAND published energy resolution is 5 % at 1 MeV, corresponding conservatively to the black lines on both plots since the positrons induced from the source have an energy between 1 and 2.3 MeV. The energy resolution is therefore not an issue for the CeLAND. Exclusion contours are given at the 95% CL for a fiducial volume is taken as 0<R<6.5 m.

Element	E (keV)	σ (barn)	A	Z	% in mass	# nuclei/cm^3	λ_i
W	2179	13.3 ± 1	183.84	74	97	$5.878 \ 10^{22}$	1.279 ± 0.096 cm
Fe	2189	$5.09 \pm .15$	55.845	26	1.5	$0.299 \ 10^{22}$	65.65 ± 0.19 cm
Ni	2188	$5.28 \pm .15$	58.6934	28	1.5	$0.284 \ 10^{22}$	66.52 ± 1.9 cm

Table 20: Data used for the computation of the attenuation length in tungsten alloy. λ_i is the partial interaction length. The total interaction length : 1.238 ± 0.14 cm.
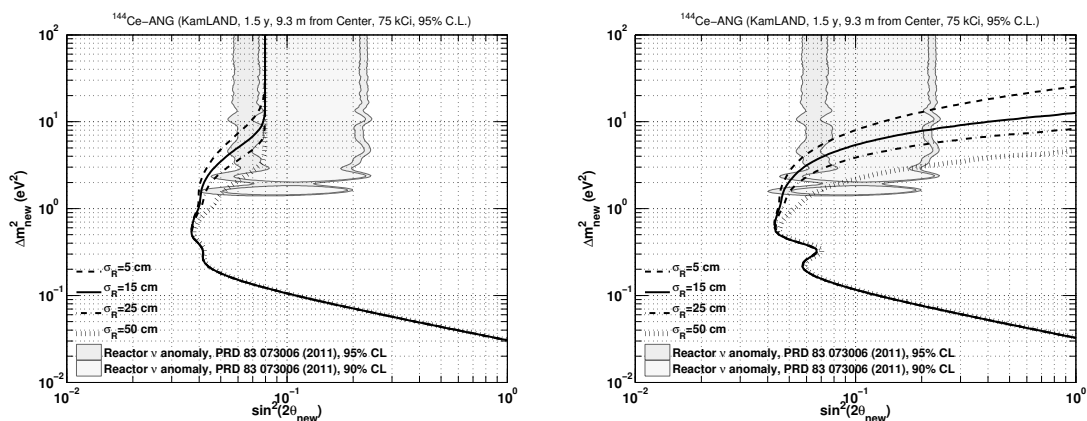

Figure 48: Impact of the KamLAND vertex resolution on the sensitivity. We assume a antineutrino generator located 9.3 m away from the detector center. The sensitivity is computed for 18 months of data taking. We vary the resolution from 5 cm to 25 cm. The left panel shows the rate+shape sensitivity assuming a normalization uncertainty of 1.5%, whereas the right panel shows the shape only sensitivity. The KamLAND published vertex resolution is 15 cm, corresponding to the black lines on all plots. Therefore one expects no concern induced by vertex resolution effect for this phase of the experiment. Exclusion contours are given at the 95% CL for a fiducial volume is taken as 0<R<6.5 m.
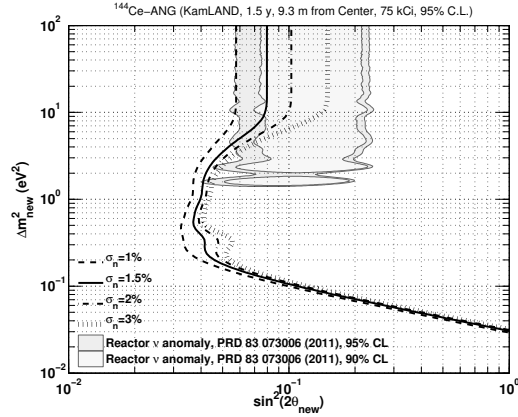
Figure 49: Impact on the knowledge of the source activity. We assume a antineutrino generator located 9.3 m away from the detector center. The sensitivity is computed for 18 months of data taking. The normalization error is expected to be about 1.5%, dominated by the uncertainty on the measurement of the absolute activity of the antineutrino generator. Exclusion contours are given at the 95% CL for a fiducial volume is taken as 0<R<6.5 m.
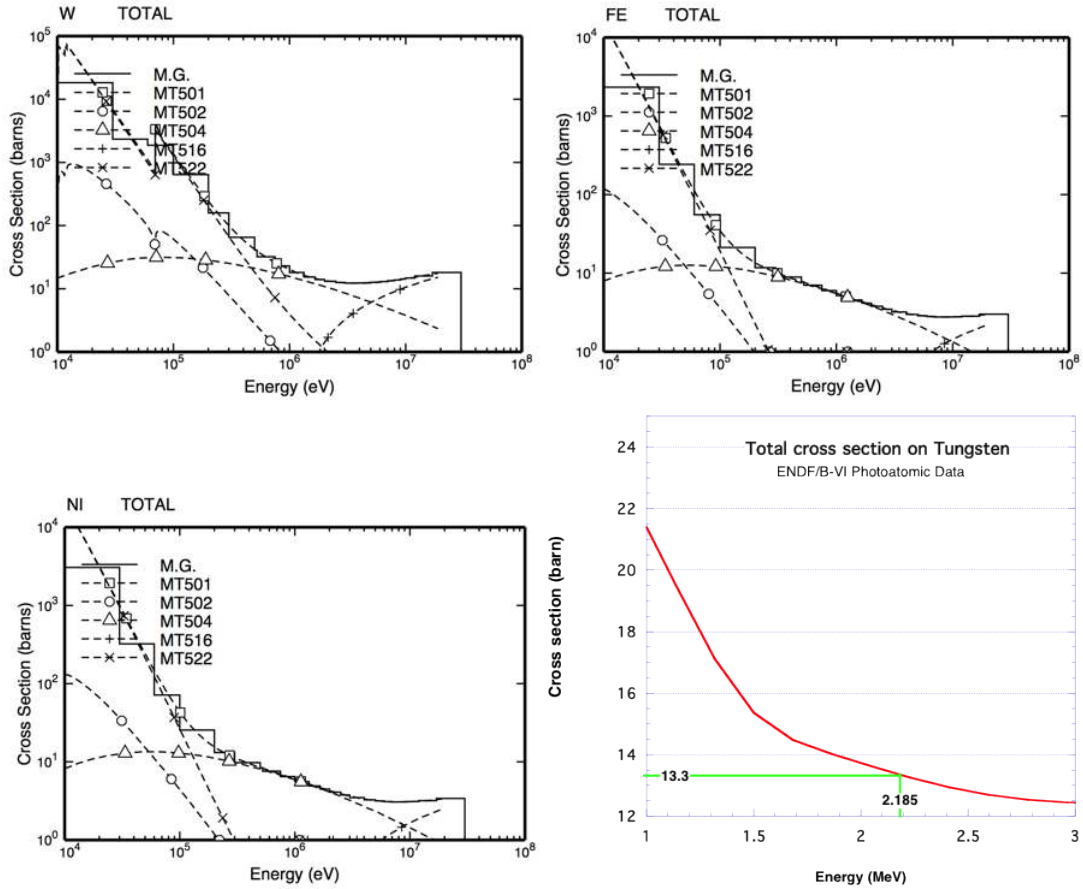

Figure 50: Cross sections of the interaction of $\gamma's$ with tungsten, iron, nickel, and tungsten alloy (18.5 g/cm^3).

References

[1] M. Cribier, M. Fechner, Th. Lasserre et al., Phys. Rev. Lett. 107, 201801 (2011)

[2] C. Giunti and C.W. Kim, "Fundamentals of neutrino physics and astrophysics", Oxford university press (2007)

[3] J. Beringer et al. (Particle Data Group), Phys. Rev. D86, 010001 (2012)

[4] A. Aguilar-Arevalo et al. (LSND), Phys. Rev. D64, 112007 (2001)

[5] A. Aguilar-Arevalo et al. (MiniBooNE), Phys. Rev. Lett. 102, 101802 (2009)

[6] A. Aguilar-Arevalo et al. (MiniBooNE), Phys. Rev. Lett. 105, 181801 (2010)

[7] C. Giunti and M. Laveder, Mod. Phys. Lett. A22, 2499 (2007)

[8] C. Giunti and M. Laveder, Phys. Rev. C83, 065504 (2011)

[9] C. Giunti, M. Laveder, Y.F. Li, Q.Y. Liu and H.W. Long, arXiv:1210.5715 (2012)

[10] G. Mention et al., Phys. Rev. D83, 073006 (2011)

[11] M. Cribier et al., NIM A 378, 233 (1996)

[12] J. N. Abdurashitov et al., Phys. Rev. C59, 2246 (1999)

[13] J. N. Abdurashitov et al., Phys. Rev. C73, 045805 (2006)

[14] P.A.R. Ade et al. (Planck collaboration), arXiv:1303.5076 (2013)

[15] K. Abazajian, G. Barenboim, B. Fleming, J. Formaggio, P. Huber, T. Lasserre, J. Link, W. Rodejohann, T. Schwetz, Y. Wong, *et al.*, arXiv:1204.5379 (2012)

[16] P. Anselmann et al. (GALLEX), Phys. Lett. B342, 440 (1995)

[17] W. Hampel . et al. (GALLEX), Phys. Lett. B420, 114 (1998)

[18] F. Kaether, W. Hampel, G. Heusser, J. Kiko and T. Kirsten, Phys. Lett. B685, 47 (2010)

[19] J.N. Abdurashitov et al. (SAGE), Phys. Rev. Lett. 77, 4708 (1996)

[20] J.N. Abdurashitov et al. (SAGE), Phys. Rev. C59, 2246 (1999)

[21] J.N. Abdurashitov et al. (SAGE), Phys. Rev. C73, 045805 (2006)

[22] Th. Mueller *et al.*, Phys. Rev. C83, 054615 (2011)

[23] P. Huber, Phys. Rev. C**84,** 024617 (2011)

[24] M. Apollonio et al. (CHOOZ), Eur. Phys. J. C27, 331 (2003)

[25] F. Boehm et al. (Palo Verde), Phys. Rev. D64, 112001 (2001)

[26] C. Athanassopoulos et al. (LSND), Nucl. Instrum. Meth. A388, 149 (1997)

[27] A. Aguilar-Arevalo et al. (MiniBooNE), Nucl. Instrum. Meth. A599, 28 (2009)

[28] A. Aguilar-Arevalo et al. (MiniBooNE), Phys. Rev. Lett. 98, 231801 (2007)

[29] A. Aguilar-Arevalo et al. (MiniBooNE), arXiv:1207.4809 (2012)

[30] C. Weinheimer et al., Phys. Lett. B300, 210 (1993)

[31] C. Weinheimer et al., Phys. Lett. B460, 219 (1999)

[32] C. Kraus, A. Singer, K. Valerius and C. Weinheimer, arXiv:1210.4194 (2012)

[33] F.M. Fraenkle (KATRIN), arXiv:1110.0087 (2011), DPF-2011 Conference, Providence, RI, August 8-13, 2011

[34] A. Gando et al. (KamLAND-Zen), Phys. Rev. C85, 045504 (2012)

[35] A. Gando et al. (KamLAND-Zen), arXiv:1205.6372 (2012)

[36] A. Gando et al. (KamLAND-Zen), arXiv:1211.3863 (2012)

[37] M. Auger et al. (EXO Collaboration), Phys. Rev. Lett. 109, 032505 (2012)

[38] J. Hamann, S. Hannestad, G.G. Raffelt, I. Tamborra and Y.Y. Wong, Phys. Rev. Lett. 105, 181301 (2010)

[39] G. Alimonti et al. (Borexino), Nucl. Instrum. Meth. A600, 568 (2009)

[40] K. Eguchi et al. (KamLAND), Phys. Rev. Lett. 90, 021802 (2003)

[41] M.C. Chen (SNO+), arXiv:0810.3694, 34th International Conference on High Energy Physics (ICHEP 2008), Philadelphia, Pennsylvania, 30 Jul - 5 Aug 2008

[42] K. Nakamura et al., J. Phys. G**37**, 075021 (2010).

[43] C. Athanassopoulos et al., Phys. Rev. Lett. **75** 2650 (1995); C. Athanassopoulos et al., Phys. Rev. C**54**, 2685 (1996); A. Aguilar et al., Phys. Rev. D**64**, 112007 (2001).

[44] J. Bahcall, P. Krastev, E. Lisi, **PLB** 349.68 (1995) 121; C. Giunti, M. Laveder, arXiv:1006.3244; P. Anselman et al., Phys. Lett. **342B**, 440 (1995).

[45] G. Alimonti *et al.*, Astropart. Phys. **16** 205-234, (2002).

[46] L.W. Alvarez. Lawrence Radiation Laboratory Physics Note 767 (1973).

[47] R.S. Raghavan, Proc. Conf. on Status and Future of Solar Neutrino Research, BNL Report 50879 (1978), Vol. 2, p. 270.

[48] W.C. Haxton, Phys. Rev. C 38 (1988) 2474.

[49] J. N. Abdurashitov et al. Phys. Rev. C59 (1999) 2246

[50] J. N. Abdurashitov et al. , Phys. Rev. C73.045805 (2006) ; V. N. Gavrin, et al., INR d d d of the Russian Academy of Sciences Report No. P-777 (1992).

[51] C. Arpesella *et al.*, Phys. Rev. Lett. **101**, 091302 (2008).

[52] M.P. Decowski, J. Phys. Conf. Ser. 136:022005 (2008).

[53] M. Chen, Nucl. Phys. **B** (Proc. Suppl.) 154, 65-68 (2005).

[54] A. Ianni *et al.*, Eur. Phys. J. **C8**, 609-617 (1999).

[55] R.S. Raghavan, Phys. Rev. Lett. **37** 259 (1976).

[56] Ch. Grieb *et al.*, Phys. Rev. D**83**, 093006 (2009).

[57] D.A. Dwyer, K.M. Heeger, B.R. Littlejohn, P. Vogel, arXiv:1109.6036 (2011).

[58] V. Kornoukhov, preprint of ITEP, Moscow, 1994. No. 90.

[59] J.S. Geiger, R.L. Graham, G.T. Ewan, Nuclear Phys. 16, 1 (1960).

[60] J. Dalmasso, H. Maria, A. Hachem, G. Ardisson, Nucl.Instrum.Methods 221, 564 (1984).

[61] J. Dalmasso, H. Forest, G. Ardisson, Phys. Rev. C32, 1006 (1985).

[62] http://www.nist.gov/

[63]

[64] S. Agostinelli et al. NIM A 506, 250 (2003).

[65] M. Cribier, CeLAND Internal Note, Thermal issues in CeLAND, 6/12/2012.

[66] M. Cribier et al., NIM A378 (1996) 233-250.

[67] Calorimetric Measurements of the ^{51}Cr Source Activity, Gallex Note GX-58.

[68] ENDF/B-VI Photoatomic Data (http://t2.lanl.gov/data/data.html)

[69] Densimet-Innermet for shielding and aerospace applications data sheet, http://www.plansee.com/en/Materials-Tungsten-403.htm#W-Schwermetall

[70] L. Katz and A.S. Penfold, Rev. Mod. Phys. 24, 28-44 (1952)

[71] KamLAND-Zen Collaboration, Measurement of the double-β decay half-life of ^{136}Xe with the KamLAND-Zen experiment,Phys.Rev.C85:045504 (2012)

[72] KamLAND-Zen Collaboration, Limit on Neutrinoless $\beta\beta$ Decay of Xe-136 from the First Phase of KamLAND-Zen and Comparison with the Positive Claim in Ge-76, arXiv:1211.3863v1 (2012)

[73] National Nuclear Data Center, Brookhaven National Laboratory, information extracted from the Chart of Nuclides database, http://www.nndc.bnl.gov/chart/

[74] E. Le Coz, Radioprotection computation for the CeLAND experiment, CEA/DSM/SAC/UPSE/SPR/SERD/2012-1437 internal Note, 17/10/2012

[75] Patrick Huber. Determination of antineutrino spectra from nuclear reactors. Phys. Rev. C, 84:024617, Aug 2011.

[76] Thomas Mueller. Expï¿œerience Double Chooz : simulation des spectres antineutrinos issus de rï¿œeacteurs. PhD thesis, Paris-Sud XI - Orsay, IRFU/SPhN, Sep 2010.

[77] Patrick Huber. Erratum: Determination of antineutrino spectra from nuclear reactors. Phys. Rev. C, 85:029901, Feb 2012.

[78] D.H. Wilkinson. Evaluation of beta-decay: I. The traditional phase space factors. Nuclear Instruments and Methods in Physics Research Section A: Accelerators, Spectrometers, Detectors and Associated Equipment, 275(2):378 386, 1989.

[79] D.H. Wilkinson. Evaluation of beta-decay: II. Finite mass and size effects. Nuclear Instruments and Methods in Physics Research Section A: Accelerators, Spectrometers, Detectors and Associated Equipment, 290(2/3):509 515, 1990.

[80] A. Sirlin. Radiative correction to the ν_e -$\overline{\nu_e}$ spectrum in β decay. Phys. Rev. D, 84:014021, Jul 2011.

[81] H. Behrens and W. Bï¿œehring. 5 Electron Radial Wave Functions and Nuclear Beta-Decay. The International Series of Monographs on Physics Series. Clarendon Press, 1982.

[80] A. Gando et al. (KamLAND Collaboration), arXiv:1303.466 (2013)

[81] S. A. Fayans, Sov. J. Nucl. Phys. 42 (4), 590 (1985).